

# **Atmosphere-surface vapor exchange and ices in the Martian polar regions**

Dissertation  
zur Erlangung des Doktorgrades  
der Mathematisch-Naturwissenschaftlichen Fakultäten  
der Georg-August-Universität zu Göttingen

vorgelegt von  
**Ganna Valeriyivna Portyankina**  
aus Karachevka/Ukraine

Göttingen 2005

## **Bibliografische Information Der Deutschen Bibliothek**

Die Deutsche Bibliothek verzeichnet diese Publikation in der Deutschen Nationalbibliografie; detaillierte bibliografische Daten sind im Internet über <http://dnb.ddb.de> abrufbar.

D7

Referent: Dr. U. Christensen

Korreferent: Dr. H.U. Keller

Tag der mündlichen Prüfung: 12 September 2005

Copyright © Copernicus GmbH 2006

ISBN 3-936586-47-0

Copernicus GmbH, Katlenburg-Lindau

Druck: Schaltungsdienst Lange, Berlin

Printed in Germany

# Contents

<b>Summary</b>	<b>5</b>
<b>1 General Introduction</b>	<b>7</b>
1.1 History of Martian polar observations . . . . .	7
1.1.1 The first detection of polar caps and early observations . . . . .	7
1.1.2 More recent telescopic observations . . . . .	8
1.1.3 Spacecraft observations of polar regions and ices on Mars . . . . .	9
1.2 Martian polar caps and their role in the martian climate and evolution . .	11
1.3 Differences between South and North polar caps . . . . .	12
1.4 Outline . . . . .	17
<b>2 Spider patterns in the Martian cryptic region - observational data</b>	<b>19</b>
2.1 Cryptic region and CO <sub>2</sub> slab ice . . . . .	19
2.1.1 Cryptic region detection . . . . .	19
2.1.2 Optical properties of CO <sub>2</sub> ice and solid-state green-house effect .	21
2.2 Spiders in MGS MOC images . . . . .	24
2.2.1 MOC polar observations . . . . .	24
2.2.2 Spider patterns in MOC narrow angle images . . . . .	26
2.2.3 Spatial distribution of spiders. Are all spiders inside the cryptic region? . . . . .	29
2.2.4 Fan structures, winds and seasonal distribution . . . . .	30
2.3 MOLA data of spider areas . . . . .	32
2.4 Conclusions . . . . .	36
<b>3 Modeling of spiders</b>	<b>37</b>
3.1 Formation of spiders . . . . .	37
3.2 Simulations of CO <sub>2</sub> ice cleaning process . . . . .	39
3.2.1 Insolation of the South polar region . . . . .	39
3.2.2 Single particle modeling . . . . .	40
3.2.3 Dust inside an ice slab . . . . .	47
3.2.4 Net effect . . . . .	52
3.2.5 Energy flux . . . . .	53
3.3 Simulations of geyser-type eruptions and CO <sub>2</sub> slab ice rigidity . . . . .	57
3.3.1 Calculations of stresses inside CO <sub>2</sub> ice plate . . . . .	57
3.3.2 Pressure below ice plate . . . . .	60
3.3.3 Discussion of material strength . . . . .	61

3.4	Conclusions . . . . .	63
<b>4</b>	<b>Seasonal evolution of the Martian cryptic region: influence of the atmospheric opacity</b>	<b>65</b>
4.1	Introduction . . . . .	65
4.2	Observations . . . . .	67
4.3	Model description and results . . . . .	74
	4.3.1 Model description . . . . .	74
	4.3.2 Model results . . . . .	74
4.4	Conclusions . . . . .	79
<b>5</b>	<b>Lee wave clouds in the Martian atmosphere: observations by HRSC</b>	<b>81</b>
5.1	Observations of Martian lee-waves before HRSC . . . . .	81
5.2	Wind velocity measurement on Mars . . . . .	82
	5.2.1 Direct measurements of wind velocities on Mars . . . . .	82
	5.2.2 Winds derived from the cloud motion. . . . .	83
	5.2.3 Winds derived from modeling or analysis of temperature fields. . . . .	83
5.3	Mars Express (MEX) and the High Resoluting Stereo Camera (HRSC), an overview . . . . .	84
5.4	The formation of lee wave clouds - mathematical formulation . . . . .	85
5.5	Measuring wind velocities from HRSC images . . . . .	91
5.6	Conclusions . . . . .	92
<b>A</b>	<b>Mars Global Surveyor MOC images which contain spiders patterns.</b>	<b>97</b>
	<b>Bibliography</b>	<b>107</b>
	<b>Acknowledgements</b>	<b>113</b>
	<b>Lebenslauf</b>	<b>115</b>

# Summary

This thesis is a report of my quest for understanding a few of the many processes that shape the Martian polar regions into the wide variety of landforms that have been observed with various spacecraft during recent years.

The main part of this work is dedicated to the study of relatively small (10m-1km) features in the South polar regions called spider patterns. We collected observational data available from Mars Global Surveyor instruments (MOC, TES, and MOLA) of areas where spiders were found. We modeled spider formation on basis of the scenario proposed by Kieffer (2003). We checked two stages of Kieffer's scenario: first, the cleaning of CO<sub>2</sub> slab ice from dust, and then, the breaking of the slab ice plate under the pressure built below it by subliming ice. Our modelling indicates that spherical grains can reach the bottom of a 1 m thick layer of CO<sub>2</sub> ice in a relatively short time of less than 20 days. During the beginning of spring, the dust sinking rate is higher than the ice sublimation rate at the top of the slab. Spherical dust grains can sink so fast that the CO<sub>2</sub> ice becomes completely clean of dust. If the dust particles are randomly oriented thin disks, then only the upper part of ice will be cleaned. At a latitude of 75°S it will take between 1 and 20 days to build enough pressure below a slab to break it. The plate should break before  $L_s = 175^\circ$ . Our results support scenario proposed by Kieffer.

Spider patterns are found in the so called cryptic region. Part of the cryptic region significantly changed its appearance between 2001 and 2003. This change may be related to the global dust storm of 2001. We modeled the seasonal ice sublimation/condensation cycle to show that the evolution of this area of the cryptic region was affected by the dust storm during the year 2001. The model includes self-consistent treatment of sublimation and condensation of CO<sub>2</sub> and H<sub>2</sub>O ices, and was used to calculate surface temperatures and the thicknesses of CO<sub>2</sub> and H<sub>2</sub>O ice layers during these two years. Our modelling shows that the dust storm lowered surface temperatures in spring, and thus caused later than usual seasonal sublimation of both CO<sub>2</sub> and water ices. The dust storm also considerably decreased the surface albedo. These two important effects almost cancel: the solar flux is reduced during the dust storm, but at the same time the dust that precipitates onto the surface reduces the albedo. Thus, the surface absorbed a bigger fraction of the solar radiation. The surface temperature stayed at about 146K for almost half of the Martian year, both during 2001 and 2003. We also studied the influence of surface roughness.

We used images of lee wave clouds acquired by HRSC to infer the velocity of the driving wind. Wind speeds have only rarely been measured on Mars, although knowledge about them is essential for understanding the local climate and evolution. HRSC images taken during orbits 68, 719, 751, 1096 show lee wave clouds distinct enough to measure their wavelength. We infer wind speeds of 24.5 - 25.2 m s<sup>-1</sup> from these images.



# 1 General Introduction

## 1.1 History of Martian polar observations

### 1.1.1 The first detection of polar caps and early observations

The polar ice caps are the most conspicuous albedo features on the surface of Mars, therefore it is not surprising that they were among the first features to be identified on the Martian surface. During 1659 Christiaan Huygens was the first to detect albedo features on the planet. Three martian oppositions later, during 1666, Giovanni Cassini made about twenty sketches of Mars at the observatory in Bologna. He was apparently the first to notice bright markings at Mars' poles. Probably this was the discovery of the polar caps. Since then they have been observed often during more than two centuries by terrestrial observers and with instruments onboard many spacecrafts.

One of the sketches by Huygens in 1672 shows the South cap. Maraldi made observations during every opposition from 1672 to 1719, and he was lucky in that Mars came closer to the Earth in 1719 than it would for another 284 years.

Maraldi described both polar caps but refrained from calling them ice-caps, and merely wrote about "white spots". He also discovered that the center of the South cap is not at the rotational pole, reported about temporal changes of the cap in connection with equatorial dark areas, and described a dark band around the edge of one cap, which he interpreted as melted water.

Frederick William Herschel, between 1777 and 1784, was the first to suggest the polar caps consisted of ice and snow that grow and shrink with the season. He observed Mars during the oppositions from 1777 to 1783 and reported on this in a paper called "On the remarkable appearances at the polar regions of the planet Mars, the inclination of its axis, the position of its poles, and its spheroidal figure; with a few hints relating to its real diameter and atmosphere". Herschel estimated the inclination of Mars' equator to its orbit plane at around  $30^\circ$ , and thought the seasons on Mars to be similar to the terrestrial ones. He speculated that the polar caps are thin layers of ice and snow.

Nicolas Camille Flammarion summarized the knowledge about Mars in a two-volume tome. The first volume was published in 1892 and had the following notes about observations of the polar regions before 1830 (from Kieffer et al. (1992)):

*"There are also on Mars white spots, marking its poles. These spots vary with season, increasing in winter, diminishing in summer. They submit to the influence of the Sun like our polar ice. We can consider them to be ice or snow."*

*"These polar snows are not situated exactly at the extremities of the same diameter and do not mark absolutely the geographic poles. These poles are generally covered. But,*

*at the epoch of minimum, they are reduced to a white point approximately circular that is removed a certain distance from the pole”*

### 1.1.2 More recent telescopic observations

During the first half of the 20th century, all possible technics of observational astronomy (visual, photographic, spectrometry, radiometry and polarimetry) were used to study Mars. There are various reasons why it is difficult to observe the Martian polar caps from Earth:

- they are quite small
- the polar regions are inclined toward the Sun (and hence better visible from Earth) during spring and summer and the other way around during winter and fall. Therefore it is much easier to observe the polar caps when they are shrinking than when they are growing. Thus, deposition phases for both polar caps are hardly documented.
- the perihelion of the Martian orbit is situated near Southern summer solstice. Therefore, the recession of the South polar cap can be observed at higher spatial resolution than the Northern polar cap.
- during the most interesting seasons of fast changes - spring and fall, both caps tend to hide below clouds. The most famous phenomenon of this type is the polar hood - haze that covers the whole polar area during the beginning of both condensation and sublimation phases. This haze is easy to confuse with freezing/subliming surface albedo changes, especially from Earth based observations that have low spatial resolution.
- observations in the visible are complicated by the near coincidence of the terminator with the edge of the cap. This also applies to spacecraft observations.

The oppositions, when Mars comes closer to Earth, offer the most favorable periods for Earth based observations.

Since the time of Cassini the Martian polar caps were thought to consist of water ice or snow, analogously to the polar caps of Earth. This was the opinion of most Mars observers, even though the Dutch astronomer Gerard Kuiper's found evidence in 1947 of carbon dioxide on Mars from telescopic observations: he discovered two relatively strong bands of CO<sub>2</sub> near 1.6 $\mu$ m on one of his spectrograms. Later he found three more near 2.0 $\mu$ m. At that time CO<sub>2</sub> was the only known constituent of the Martian atmosphere. However, CO<sub>2</sub> was considered as a minor atmospheric component for a long time - until the flight of Mariner 4. As the first space probes visited the planet they proved that carbon dioxide is the main constituent of the atmosphere, and hence, that it possibly contributes to the polar ices.

Many telescopic observations were made to monitor seasonal changes of the polar caps. As noted above, the recession phase of the caps is better documented than the deposition phase. From the beginning of the 20th century, the Martian polar caps were observed during all oppositions. These observations indicate that the North polar cap remains roughly circular during the whole period of its recession, while the South polar cap shows asymmetric recession, which results in a relatively small residual cap shifted by 6.5° from the geographic pole. The list of observations can be found in Kieffer et al. (1992).

Light from the surface cap is almost unpolarized while clouds reflect strongly polarized light. Therefore to separate between the appearance of the atmospheric polar hood

and the growing of the seasonal polar cap, the Northern cap was observed with a polarimeter (Focas 1961). The polarization signature of the polar hood is very similar to that of other clouds. As spring progresses, the cloud-polarized light from the polar region is diluted by unpolarized light from the polar cap.

Continuous observations of the Martian polar regions proved that clouds and hazes are locally important phenomena. Both the condensation and deposition processes on the polar caps depend on atmospheric condensate and dust clouds, and on advection and surface deposition of dust.

In addition to Earth-based telescopic observations Mars was monitored in a number of observational programs of the Hubble Space Telescope (HST) (Cantor et al. (1998), Wolff et al. (1999), Bell et al. (2003)). These observational programs included monitoring of polar cap regression rates as well as large scale atmospheric features like polar hood or semitransparent transient clouds (Shkuratov et al. 2005).

### 1.1.3 Spacecraft observations of polar regions and ices on Mars

An American spacecraft, the Mariner 4, performed the first successful fly-by of Mars during 1965. Its photographs revealed a heavily cratered Moon-like surface, some of the craters touched with frost in the chilly Martian evening.

The analysis of two sets of radio occultation data indicated that the surface pressure might be only 4 or 5 mbar. Such low pressures were below the triple point of water and forced the conclusion that water is only stable as ice or gas on the present Mars.

Mariner 4 also measured temperatures of the Polar cap surface to be  $-80^{\circ}\text{C}$  - too low for water ice. As  $\text{CO}_2$  was already known to be the main component of the Martian atmosphere (95.32%), the low temperatures hinted at the existence of frozen  $\text{CO}_2$ .

Mariner 6 and 7 were the second pair of Mars missions in NASA's Mariner series of solar system exploration in the 1960s and early 1970s. In 1969, Mariner 6 and Mariner 7 completed the first dual mission to Mars, flying by over the equator and South polar regions and analyzing the Martian atmosphere and surface with remote sensors, as well as recording and relaying hundreds of pictures. The infrared radiometer onboard of Mariner 7 measured the temperature of the South polar cap, it appeared to be 150K - i.e. the condensation temperature of  $\text{CO}_2$ . At the same time, measurements of the infrared spectrometer showed polar cap temperatures of 203K, indicating water ice.

Russian spacecrafts also contributed to Martian polar exploration. For example, the optical instruments in infrared and visual wavelengths on Mars 3 yielded good data. Surface temperatures at the North polar cap were close to carbon dioxide condensation temperatures and condensation clouds of sub- $\mu\text{m}$  were observed.

Mariner 9 was the first spacecraft to orbit Mars. It transformed the image of Mars once again; after Mariner 9, Mars was no longer considered to be a dead desert planet. The spacecraft arrived at Mars in the middle of a global dust storm and observations had to wait until the dust settled down in the atmosphere. After this, it discovered a different planet than expected: Olympus Mons proved to be a giant volcano, Valles Marineris was discovered, a grand canyon stretching 4,800 kilometers across the planet's surface. Even more surprisingly, ancient river beds were carved in the landscape of this seemingly dry and dusty planet.

Mariner 9 images revealed that the remnant summer cap of the Southern pole was

surrounded by a thick sequence of layered deposits. And additionally that carbon dioxide survived all year long at the Southern residual cap (Paige et al. 1990).

The S-Band Occultation Experiment measured the temperature of the lower atmosphere near both the poles. In winter it appeared to be close to the sublimation temperature of carbon dioxide, whereas during spring the temperature over the North pole was much warmer than over the South pole.

The Infrared Spectrometry Experiment took more than 20,000 spectra. It showed evidence of gaseous carbon dioxide, water, entrained dust, and ice crystal clouds.

Two identical Viking spacecrafts, each consisting of an orbiter and a lander, were launched in 1975. These missions were the first to land a spacecraft safely on the surface of another planet. During 1976 the Viking orbiters made extensive observations. In particular, they showed that the Northern polar cap had a surface temperature of about 200 K indicating that it was too warm for ice of carbon dioxide - it had to be water-ice.

The Mars Atmospheric Water Detectors (MAWD) produced global maps of the quantity of water vapor at all seasons, thus revealing the seasonal cycle of vapor transport and demonstrating that the residual Northern polar cap in the summer was water ice.

The Infrared Thermal Mappers mapped the temperature, albedo and thermal inertia of the entire surface; they detected a lot of local dust storms and demonstrated along with MAWD, that the Northern polar cap in the summer was water ice; the residual South polar cap was covered with CO<sub>2</sub> frost.

Viking images revealed that layered terrains exist at both North and South pole. There have also been many studies, both in the visual and IR, focussing on the shape of the North polar cap during its recession (James (1979), James (1982)). They revealed that the North polar cap stays circular and has its center on the geographical pole during its recession. A similar study for the South pole (James et al. 1979) showed the cap's asymmetry during recession.

The next successful mission to Mars that contributed enormous amount of data to the polar investigations is the Mars Global Surveyor (MGS) (Arden et al 2001). It was launched November 7, 1996 and to date still continues its extended mission. Since it is in polar orbit, MGS is a perfect mission for polar science. The polar science objectives of MGS cover a wide range of open questions. In brief these are: the shape and volume of the residual polar caps and the polar layered deposits; nature, stratigraphy and evolution of meter-scale landforms in polar regions; seasonal polar cap evolution as well as short time scale changes, study of atmospheric conditions to gain better understanding of the past and present climate. These objectives are addressed by three instruments:

- The Mars Orbiter Camera (MOC) (a description can be found in chapter 2.2) provided images of both polar regions with high spatial resolution of up to 1m per pixel. The polar regions are well covered by MOC, and some places were observed several times to monitor seasonal changes.

- The Mars Orbiter Laser Altimeter (MOLA) (briefly described in section 2.3) provided global elevation maps, including the models of the polar cap. It also derived seasonal thickness of carbon dioxide layers on the poles (Aharonson et al. 2004);

- The Thermal Emission Spectrometer (TES) (Christensen et al. 1992) contributed with highly accurate monitoring of surface temperatures.

Data of all three instruments were used for this work.

Another orbiter that is still active is Mars Odyssey. It was launched on April 7, 2001.

The primary science mission lasted until August 2004, currently Odyssey is in its extended mission.

Less than a month after the science mapping campaign began, Odyssey's Gamma Ray Spectrometer detected copious hydrogen just under Mars' surface in the planet's South polar region. Researchers interpret this hydrogen as an evidence for frozen water. At the moment, global maps of hydrogen in the first meter below the surface are available. These show the presence of water on both poles during local summer, while during winter the signatures of water decrease and can even disappear completely as CO<sub>2</sub> ice condenses onto the surface (Litvak 2004).

Mars Express (MEX) is the latest spacecraft sent to Mars. Mars Express was launched on June 2, 2003 from the Baikonur Cosmodrome in Kazakhstan with a Russian Soyuz/Fregat launcher. After its six-month journey the orbiter successfully entered Martian orbit on December, 25, 2003.

MEX is in an almost polar orbit and offers great opportunities for studying polar regions. Section 5.3 offers a description of HRSC, one of its instruments. We use data from HRSC to estimate the wind velocities in polar regions in section 5.5. Another instrument that made various discoveries concerning the polar caps is OMEGA - a visible-infrared imaging spectrometer.

Mars Express cooperates with NASA's twin robot geologists, the Mars Exploration Rovers, which are presently working on the surface of Mars. These were launched on June 10 and July 7 of 2003, to search for answers about the history of water on Mars, and landed on Mars January 3 and January 24, 2004. The collaboration includes, among others, atmospheric studies.

During the first year of its mission, MEX already collected numerous observations of the polar regions. Among them: HRSC images of both polar caps; detection of a broad range of clouds, including those over poles also made with HRSC (chapter 5.1), detection of perennial water ice in the South polar cap (Bibring et al. 2004) and monitoring of North polar cap evolution during summer (Langvin et al. 2005).

## **1.2 Martian polar caps and their role in the martian climate and evolution**

The polar caps are composed of polar residual ice and polar layered terrain. The bulk of the residual cap is mainly water ice, in winter each cap is covered with a seasonal coating of CO<sub>2</sub> ice. This seasonal cover extends to 50°-60° latitudes and approximately has a thickness of 1m (Aharonson et al. (2004) and Smith et al. (2001b)).

The layered terrains consist of layered ice and dust mixtures. The layered deposits are approximately centered on the poles. Until now it is unknown how much of them is dust and how much of it is ice, presumably their structure hold a record of the climate history of the planet. The layered terrain has a smooth surface that is almost free of craters, indicating that it is geologically young. On both poles show numerous valleys which form giant spiral patters. At the North pole these spirals are oriented counter clockwise, in the south the spirals wind the other way around. Equator facing slopes of the valleys expose layers of brighter and darker material and are mostly defrosted during summer. The average thickness of each layer ranges from 10 m to 50 m. These layers vary in

albedo, reflecting their varying proportion of dust and ice. They are probably the result of volatile and dust accumulation during geologically long time intervals, and are therefore commonly expected to contain a record of the martian climate, that extends back at least  $\sim 10^5 - 10^8$  years. The question how to read this record is one of most exciting questions in martian polar science.

The polar caps are reservoirs for atmospheric  $H_2O$  and  $CO_2$  (Malin et al. 2001). Each year the mass of complete varies by several tens of percent due to the freezing and subliming of the seasonal  $CO_2$  polar ices. Surface pressure measurements of two Viking probes recorded these seasonal variations. The residual caps are important for the martian water cycle because of their ability to act as sources or sinks of atmospheric water. Seasonal  $CO_2$  serves as a cold trap for water.

The polar regions are subject to an active wind regime. Since the early condensation and sublimation of a significant part of the atmosphere generates strong winds. Thermal contrasts caused by the latent heat of ice, and strong albedo changes can also generate regional winds. In addition, the topography of the polar regions is sufficient to generate slope winds. Wind patterns near the poles are easy to detect from a variety of frost and dust streaks, as well as by dune fields. In chapter 5 we give an example of how winds were measured above the North polar cap. The formation of  $CO_2$  clouds and snowfall during the Martian polar night is still far from understood but it is a widely addressed topic (Colaprete and Toon (2002), Titus et al. (2001)). Presumably most of the  $CO_2$  ice condenses directly onto the surface, but a fraction should also condense into snowflakes in the atmosphere, thus strongly influencing the radiative properties of the atmosphere and the Martian surface (Forget et al. 1995).

Another interesting atmospheric phenomenon connected to the polar caps is the polar hood. The polar hood is a haze which form over the cap in fall during cap condensation and covers the full cap. This haze appears when atmospheric temperatures drop below the condensation point. The polar hood also shades the cap underneath thus cooling the surface.

Here we conclude, that polar processes can be sensitive indicators of the global climate. Therefore, surface features associated with the poles are indicators of climate evolution. how we have to interpret this record of earlier climates is a complicated question, not in the least because of the huge differences between the North and South poles (Fishbaugh and Head III (2001), Thomas et al. (2000)).

### 1.3 Differences between South and North polar caps

Mars possesses a general asymmetry between the Southern and the Northern hemispheres: Southern hemisphere is approximately 5km higher than Northern, and much more cratered.

Due to the eccentricity of its orbit, Mars is closer to aphelion during the Southern winter, and close to perihelion during the Southern summer. Therefore, the winter is longer and colder in the Southern hemisphere than in the Northern. This creates clear differences between the two polar caps: the seasonal South polar cap is larger than the North cap. In the South seasonal frosts extend to between  $-50^\circ$  and  $-55^\circ$  latitudes, in the North to roughly  $55^\circ$ .

It is useful to introduce a calendar based on  $L_s$ , the areocentric longitude of the Sun.

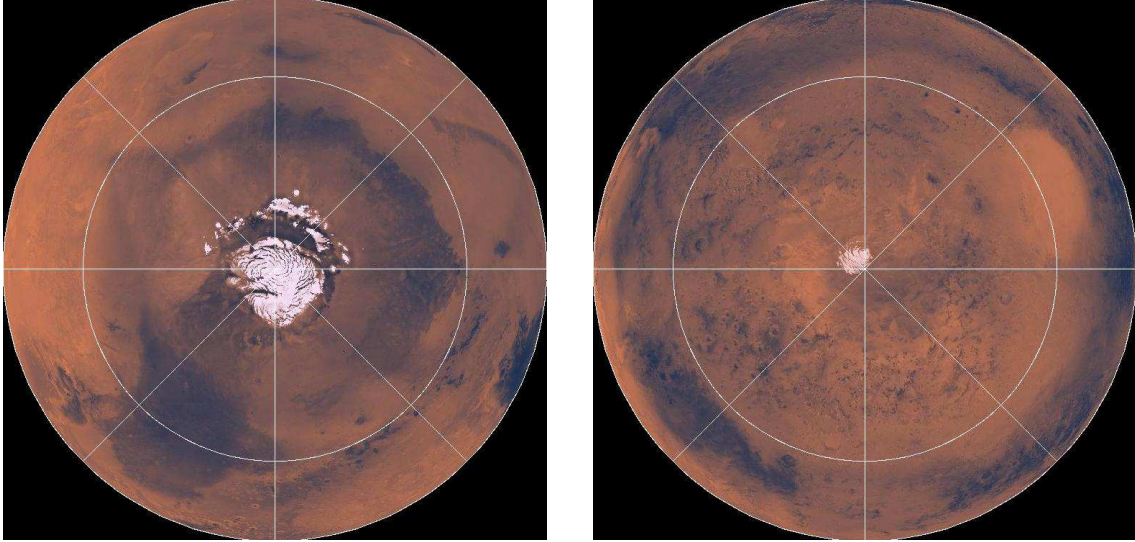


Figure 1.1: North (left panel) and South (right panel) residual polar caps.

$L_s$  gives Mars's position in its orbit relative to the Sun-Mars line at the Northern spring equinox, which marks the beginning of Northern spring. This point is defined as  $L_s = 0^\circ$ . The Northern spring lasts from  $L_s = 0^\circ$  to  $90^\circ$ , summer from  $90^\circ$  to  $180^\circ$ , fall from  $180^\circ$  to  $270^\circ$ , and winter from  $270^\circ$  to  $360^\circ$  (or  $0^\circ$ ). Algorithm of moderately accurate closed-form representation of  $L_s$  is described in Allison (1997).  $L_s$  is calculated in terms of mean anomaly  $M$  (or mean longitude with respect to the perihelion) and the right ascension of the "fictitious mean sun"  $\alpha_{FMS}$ .

$$\Delta t_{J2000} = (JD - 2451545.0)$$

$$M = 19^\circ.41 + (0.5240212^\circ/d)\Delta t_{J2000}$$

$$\alpha_{FMS} = 270^\circ.39 + (0.5240384^\circ/d)\Delta t_{J2000}$$

$$L_s = \alpha_{FMS} + (10^\circ.691 + 3^\circ.7 \cdot 10^{-7}d^{-1}\Delta t_{J2000}) \sin(M) + 0^\circ.623 \sin(2M) + 0^\circ.050 \sin(3M) + 0^\circ.005 \sin(4M) \quad (1.1)$$

While an average Mars solar day (or "sol") is only 39 minutes, 35.2 seconds longer than the terrestrial 24 hours, a Mars solar year is 1.881 Earth years, or 668.59 sols. The  $25.2^\circ$  tilt of the planet's equator with respect to the plane of its orbit imposes an Earth-like progression of the seasons. For more details of Martian orbit parameters see Table 1.1.

During the winter, both polar caps are centered on the geographical poles. However, during the spring recession, they show different behavior: the Northern cap retreats almost symmetrically, while the position of Southern one becomes asymmetrical with respect to pole - its center is offset from the rotational pole by about  $5^\circ$ . Fig. 1.1 show how both caps look during the local summer. The Southern residual cap has a much smaller size than the Northern one.

The mean albedo of the Southern polar cap is higher than that of the Northern one. Dust contained inside the ice modifies the albedo, which can explain this difference. Most probably, the reason is that most of dust storms occur during the Southern summer. The

Element	Symbol	Numerical Value
Perihelion Date (mean element)	$t_p$	1999 Nov 25.46 =JD 2451507.96
Areocentric longitude of Perihelion	$L_{sp}$	250°.98
Anomalistic Year (perihelion-to-perihelion)	$\tau_{anomal}$	686.9951 <sup>d</sup> = 668.6141 <sup>sol</sup>
Tropical Year (fictitious mean sun)	$\tau_{trop}$	686.9725 <sup>d</sup> = 668.5921 <sup>sol</sup>
Mars solar day	sol	24 <sup>h</sup> 39 <sup>m</sup> 35.244 <sup>s</sup> = 1.02749125 <sup>d</sup>
Orbital Eccentricity	e	0.0934+0.00012/d <sup>post-J2000</sup>
Orbital Longitude of Perihelion	$\varpi$	336°.04+0.00012/d <sup>post-J2000</sup>
Mean Solar Distance	a	1.52366 AU = 2.27936 · 10 <sup>8</sup> km
Obliquity	$\varepsilon$	25°.19

Table 1.1: Mars mean orbit and rotational elements (J2000) (from Allison (1997)).

dust suspended in the atmosphere shadows the Southern areas from the Sun's radiation. Meanwhile, CO<sub>2</sub> condenses in the North. It nucleates around dust grains, thus retrieving the dust from the atmosphere. In winter, when the Southern cap forms, the atmosphere is clear, and thus very clean CO<sub>2</sub> condenses in the south.

Another difference between the two polar regions is that in the North the seasonal CO<sub>2</sub> completely sublimates away during the local summer, revealing the permanent water ice cap. Unlike the Northern region, the South polar region stays cold enough during summer to retain frozen carbon dioxide. Viking Orbiter observations during the late 1970s showed that very little water vapor comes off the South polar cap during summer, indicating that any frozen water that might be there remains solid throughout the year. At the South pole the carbon dioxide ice never completely disappears. The OMEGA team reported the identification of water ice in the residual South cap during summer, when the polar cap is smallest (Bibring et al. 2004). This water ice was detected in CO<sub>2</sub>-free areas between CO<sub>2</sub>-covered places.

Besides the listed global-scale differences, the images from MOC NA show clear differences of topography of Southern and Northern polar regions.

The most typical surface features in the South polar areas are:

- **Spiders patterns** (Fig.1.2, a) Branching radial troughs emanating from central depressions were called spiders because of their unusual morphology. Spiders and their formation are addressed in chapters 2 and 3.

- **Swiss cheese** (Fig.1.2, b) The surface of the residual South polar cap partly shows pattern that resembles sliced swiss cheese. It was for the first time noted by Thomas et al. (2000). Shown here is a frost-covered surface at the very beginning of Southern spring in which two layers are evident: a brighter upper layer with swiss cheese-like holes, and a darker lower layer below the "swiss cheese" pattern. Many other images show these flat-floored, circular pits that are usually about 8 meters deep and 200 to 1,000 meters in diameter. They grow outward by about one to three meters per year (Byrne and Ingersoll 2002). These features uniquely exist within the South polar cap of Mars.

- **Fingerprints** (Fig.1.2, c) Some portions of the martian South polar residual cap have long, somewhat curved troughs instead of circular pits. These appear to form in a layer of

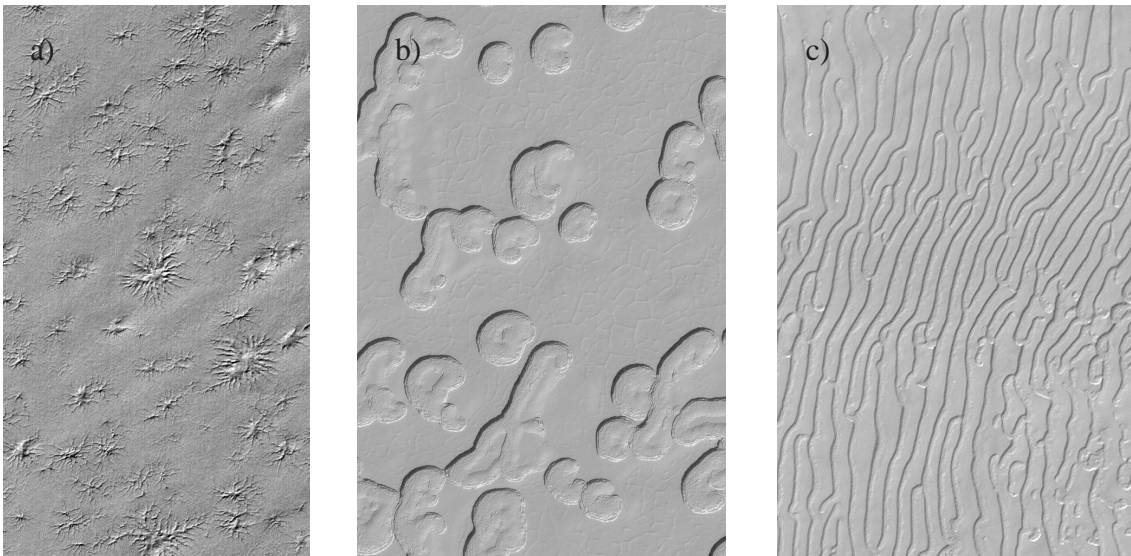


Figure 1.2: Examples of different types of terrain near the South pole. a) First panel: summer time of the spiders. This image, MOC m11-02368, was taken at  $L_s=283.88^\circ$  at the location  $232.57^\circ\text{W } 87.11^\circ\text{S}$ . The image width is 7.15 km at a resolution of 2.75 meters per pixel. The Sun illuminates the scene from the lower right corner. b) The middle panel represents a subsection of MOC NA image e10-00804 acquired during Southern summer at  $L_s=267.05^\circ$ . The image shows circular depressions called swiss cheese. The imaged location is  $87.00^\circ\text{S}, 5.67^\circ\text{W}$ , and covers an area of 1.49 km across with a resolution of 1.45 meters per pixel. c) The right panel is an example of the fingerprint terrain. This MOC image m03-06756, was obtained during early Southern spring on August 4, 1999. It shows an area of 3 x 5 kilometers at a resolution of about 7.3 meters per pixel. The image is located near  $86.0^\circ\text{S}, 53.9^\circ\text{W}$ .

material that may be different than that in which "swiss cheese" circles and pits form, and none of these features have any analogs in the North polar cap or elsewhere on Mars. This picture shows the "fingerprint" terrain as a series of long, narrow depressions considered to have formed by collapse and widening by sublimation of ice.

In contrast, the Northern cap regions have:

- **Dark dune fields** (Fig. 1.3, a, b) Dunes with a very much smaller albedo than the bright ice covering the surface around them. The shape of them appeared to be modified by the wind, prevailing in the area.

- **Cottage cheese** (Fig. 1.3, c) The North polar cap has a relatively flat surface, covered with pits, that resembles cottage cheese.

The differences between the North and the South pole is not yet fully understood. For example, the processes that lead to the formation of specific surface features should include the interaction of surface and atmospheric volatiles, wind activity, dust sedimentation, changing insolation conditions on both seasonal and on longer time scales. Over the next years, ongoing investigations will address many unsolved questions in polar science and, in doing so, vastly enhance our understanding of the nature and evolution of the poles. Martian polar regions are likely to remain a high priority objective of current and future exploration.

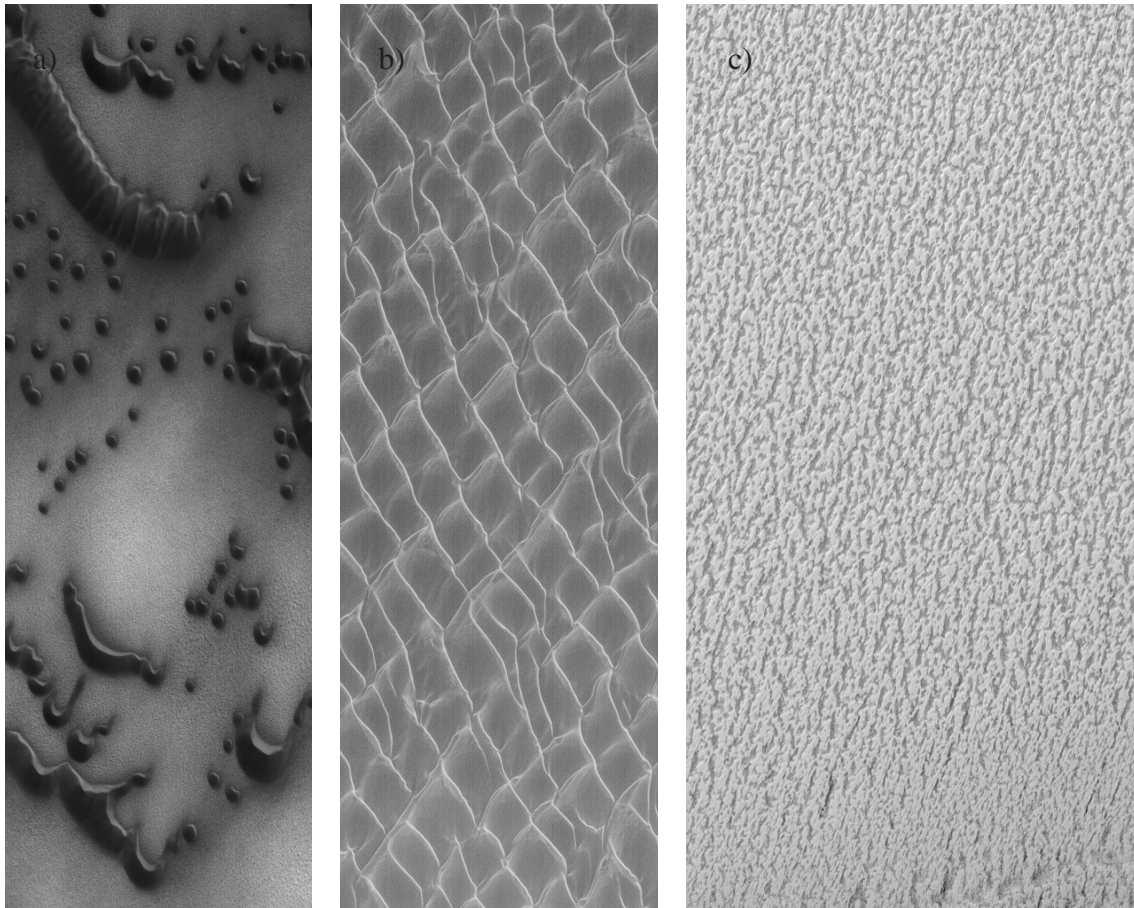


Figure 1.3: Three examples of typical North polar landforms. a) A sub-field of MOC NA image showing dark sand dunes. The dominant winds, which are responsible for these dunes, blew from the lower left. The dunes are located near  $76.6^{\circ}\text{N}$ ,  $257.2^{\circ}\text{W}$ . The picture covers an area that is 3 km wide; sunlight illuminates the scene from the upper right. b) Middle panel: North polar dunes in late winter, imaged in January 2004. At the time, the dunes were covered with frost. The location is  $77.8^{\circ}\text{N}$ ,  $52.8^{\circ}\text{W}$ . The image covers an area about 3 km wide. The sunlight illuminates the scene from the lower left. c) The right panel shows, at about 3 meters per pixel resolution, a surface of the North polar ice cap of Mars that is informally called 'cottage cheese'. This picture was taken during Northern summer, the scene is located near  $82.1^{\circ}\text{N}$ ,  $329.6^{\circ}\text{W}$ , and covers an area 1.5 km wide by 3 km long.

## 1.4 Outline

Although the Martian polar regions have intensively been observed, a lot of questions remain unanswered. A few examples:

- How were the present polar caps formed? What is the origin of the polar layered deposits? Can these layers be interpreted as a climate record?
- What is the present climate above the caps?
- Why are the South and North polar regions so different? Why is the South polar cap not centered on the geographical pole?
- What causes the small-scale differences between the Northern and Southern polar caps? How do spiders, swiss cheese, cottage cheese form?

The main part of this work is dedicated to the study of relatively small (10m-1km) features in the South polar regions - spider patterns. As spiders were found inside (and only inside) the South polar regions, they must somehow offer clues about processes acting in the South, but not (or differently) in the North.

In chapter 2 we present and discuss observations of spider patterns areas, in particular, from the Mars Orbiter Camera and the Mars Orbiter Laser Altimeter. We gathered the collection of spider images from MOC, listed in appendix. The spatial distribution of spiders was compiled on the base of this collection. We also discuss various properties of spiders.

Chapter 3 is dedicated to the modeling of spider formation. We check the model proposed by Kieffer (2003) and show its feasibility.

Chapter 4 is an attempt to understand the interannual variability of areas of spider formation: we model the local CO<sub>2</sub> and water ice thicknesses and surface temperatures of the location, that was imaged by MOC during two different years and showed large differences in albedo.

In chapter 5 we use HRSC images of the North polar cap to estimate wind velocities over the area. Wind speeds have only rarely been measured on Mars, although knowledge about them is quite important if one wants to understand the local climate and its evolution.



## 2 Spider patterns in the Martian cryptic region - observational data

### 2.1 Cryptic region and CO<sub>2</sub> slab ice

#### 2.1.1 Cryptic region detection

Cryptic region was first identified by Kieffer et al. (2000) from analysis of the Thermal Emission Spectrometer (TES) data collected during the early part of the Mars Global Surveyor (MGS) mission. MGS began mapping operations from Mars orbit on 1 March 1999 ( $L_s=104$ ). It monitors martian atmosphere and surface almost continuously. Since the spacecraft is in an almost polar orbit, TES acquires very good coverage of the South polar regions, thus allowing mapping polar cap recession, temperatures at the surface and in the atmosphere and albedo features inside the seasonal polar cap. This unique data set enabled the detection of Cryptic region.

Figure 2.1 shows the type of data Kieffer used in his work. The upper panel shows the surface albedo of the selected areas of interest. The lower panel shows the temperature of these regions (as measured with the TES equivalent of the Viking  $T_{20}$ ). Among other regions (such as perennial polar cap and Mts. Mitchel) there is a region called cryptic. It is located between latitudes  $85^\circ\text{S}$  and  $75^\circ\text{S}$  and longitudes  $150^\circ\text{W}$  and  $310^\circ\text{W}$ . The plots for this region are marked with red. From the albedo plot one can see that this region has low ( $< 0.3$ ) albedo for almost all values of  $L_s$ . This albedo is compatible with the typical albedo of martian regolith. During  $L_s$  from  $180^\circ$  to  $230^\circ$ , the temperature is at the same time below 160K. On Mars such temperatures indicate frozen CO<sub>2</sub> ice. CO<sub>2</sub> ice, however, should have higher albedo than 0.3. This contradiction, a combination of low temperature with low albedo led Kieffer to name this region 'cryptic'. One of the first observations of cryptic region by Kieffer et al. (2000) is shown in Fig. 2.2.

The boundaries of the cryptic region were defined by Piqueux et al. (2003) by contouring the albedo data at the value of 0.38. Only regions with albedos below this value and located within the seasonal cap (which was determined from the data on surface temperature) were considered to be cryptic.

The reasons for geographic distribution of cryptic material is still unknown. The boundary of cryptic region does not correlate with any other properties of the surface such as elevation, geological structure, chemical composition or thermal properties.

Piqueux et al. (2003) also showed how cryptic region evolves with time Fig. 2.3 from their paper illustrates seasonal changes of cryptic region. Initially at  $L_s=175^\circ$  the cryptic region covers almost the full range of longitudes surrounding the residual polar cap. As

## 2 Spider patterns in the Martian cryptic region - observational data

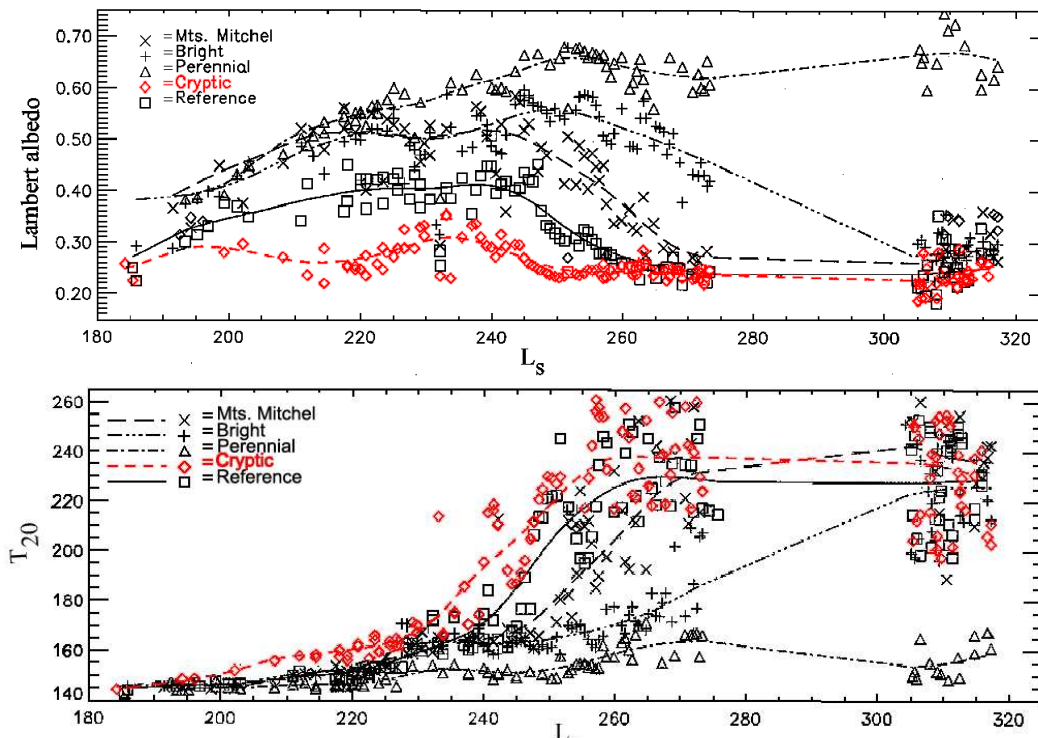


Figure 2.1: This is the first observations of the cryptic region. The curves for cryptic region are marked with red. From Kieffer et al. (2000).

the season progresses, the area designated as cryptic rapidly shrinks to a minimum at  $L_s=200$ . Then cryptic region begins to expand in the direction of  $150^\circ\text{W}$ - $300^\circ\text{W}$ . Between  $L_s=205^\circ$  and  $230^\circ$  the cryptic region takes the form previously discussed by Kieffer et al.

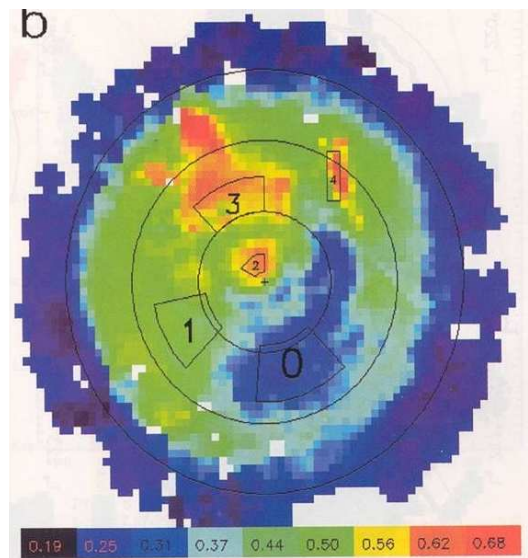


Figure 2.2: Detection of the cryptic region. It was defined as area having simultaneously low albedo ( $<0.3$ ) and low temperature ( $<160\text{K}$ ). This image shows surface albedo map of Mars South Pole as measured by TES. From Kieffer et al. (2000)

(2000). After this period cryptic region merges to the retreating edge of the seasonal cap and fades from the view (Piqueux et al. 2003).

### 2.1.2 Optical properties of CO<sub>2</sub> ice and solid-state green-house effect

On Mars seasonal CO<sub>2</sub> surface ice in polar regions recondenses every year. Condensation happens by radiative cooling from nearly pure CO<sub>2</sub> atmosphere. During such a process two types of resulting solids can form: columnar crystals oriented along the diffusion gradient or thick slab ice. The growth of both ice types were observed in laboratory conditions (Kieffer 1968, 1970).

If the abundance of non-condensing gases is negligible, then a thick slab ice forms. This is particularly true when the amount of gas between the condensation site and the low-radiation background (space) is large enough that significant path lengths in the solid are needed to generate appreciable emissivities outside the bands in which the gas absorbs. In this case, which holds for Mars, the dominant radiative loss of the condensate is from inside the bulk material. Growth perturbations outward from a planar solid interface, such as a crystal spike growing upward, have a poor conductive path to the bulk solid which, in turn, can radiate away the latent heat of condensation. Lacking a diffusion gradient at the tip of such a spike, the condensation rate is limited by conductive heat loss, not by abundance of molecules in the gas phase, and this tip is at a disadvantage for condensation relative to the bulk solid. Thus these perturbations do not grow, and the expected steady state form is a thick slab with a smooth surface.

In the presence of some amount of non-condensing gas there will be some diffusion gradient of the condensing gas towards the condensation sites. If one assumes that both the temperature gradient and the concentration gradient of the condensate are linear across this layer, then, because of the nonlinear dependence of saturation pressure on temperature, the partial pressure will be above the saturation pressure throughout this layer. Under this condition, if there is adequate heat conduction down the spike into the substrate (from which radiation is efficient), then spikes sticking up into this diffusion gradient become the favored site of condensation and they will grow more rapidly than locations deeper into the diffusion gradient.

TES spectra in the 25  $\mu m$  region indicate that the cryptic regions of cold-dark material consist of a CO<sub>2</sub> non-scattering ice slab composed of indeterminately large grains.

In this case the best solution to the paradox of low albedo together with low temperatures observed in the cryptic region is to assume that the surface with the albedo of approximately 0.3 is covered by ice with the temperature of 160K. This cover is transparent and forms a slab consisting of large grained crystals. Then specific optical properties of CO<sub>2</sub> ice, when it is exactly slab ice, play an important role and will be discussed next.

Optical properties are determined by the complex index of refraction, the imaginary part of which is proportional to the absorption. Figure 2.4 shows the indexes of refraction of three important components of martian polar regions - water ice, CO<sub>2</sub> ice, and dust (the figure is adopted from Hansen (1999)). The top panel gives the real part of index of refraction or refractive index, and the bottom panel the imaginary part of index of refraction. The visible and near-infrared absorption of CO<sub>2</sub> ice is rather uncertain, but it is very small, and an upper limit can be set confidently. The main differences are in the imaginary index, which is low in both ranges for CO<sub>2</sub> ice, low in the visible and

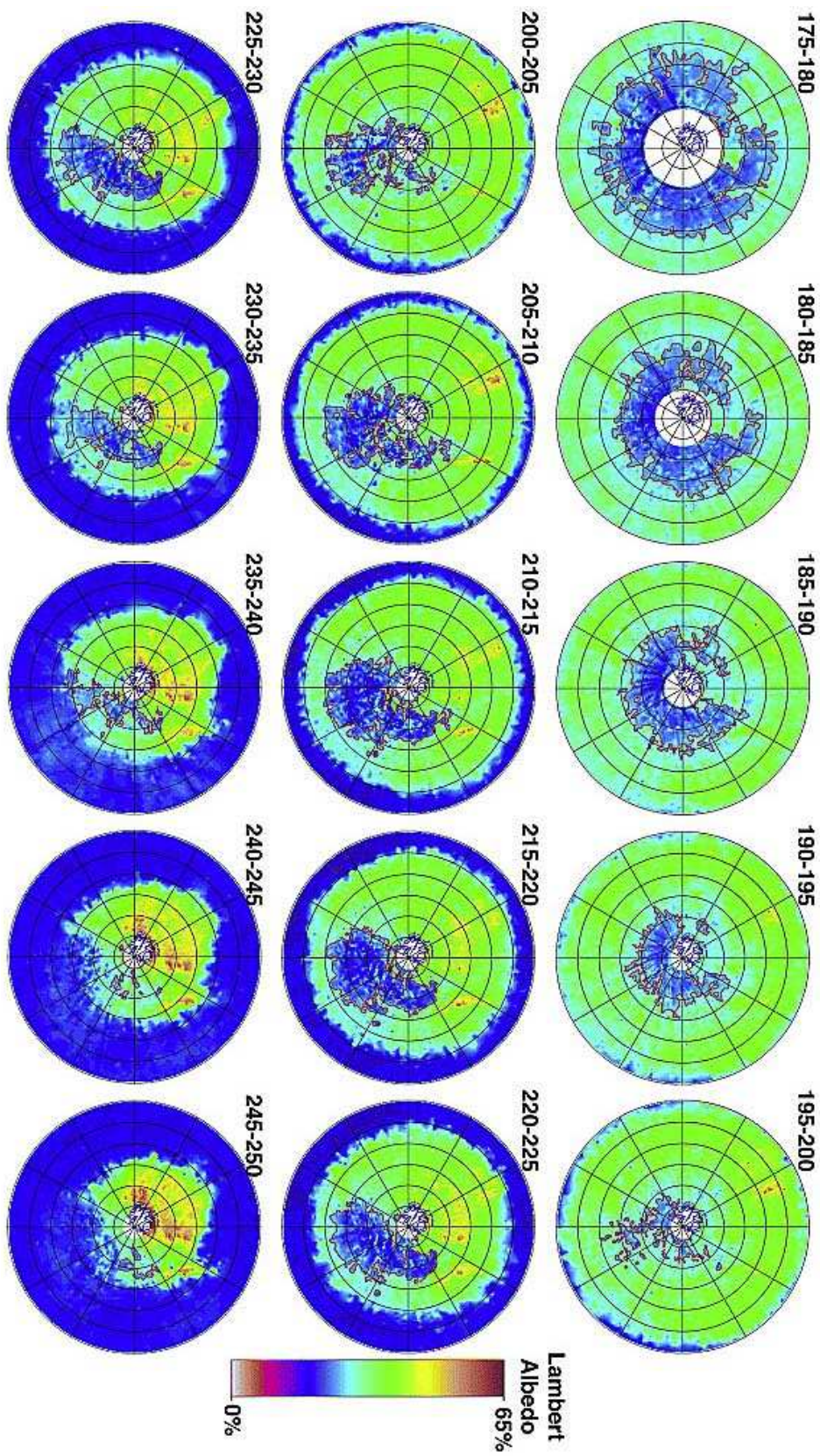


Figure 2.3: Evolution of the cryptic region as a function of season from the South pole to  $60^\circ$ . Shown here is TES Lambert albedo. Cryptic region is outlined with red. From Piqueux et al. (2003).

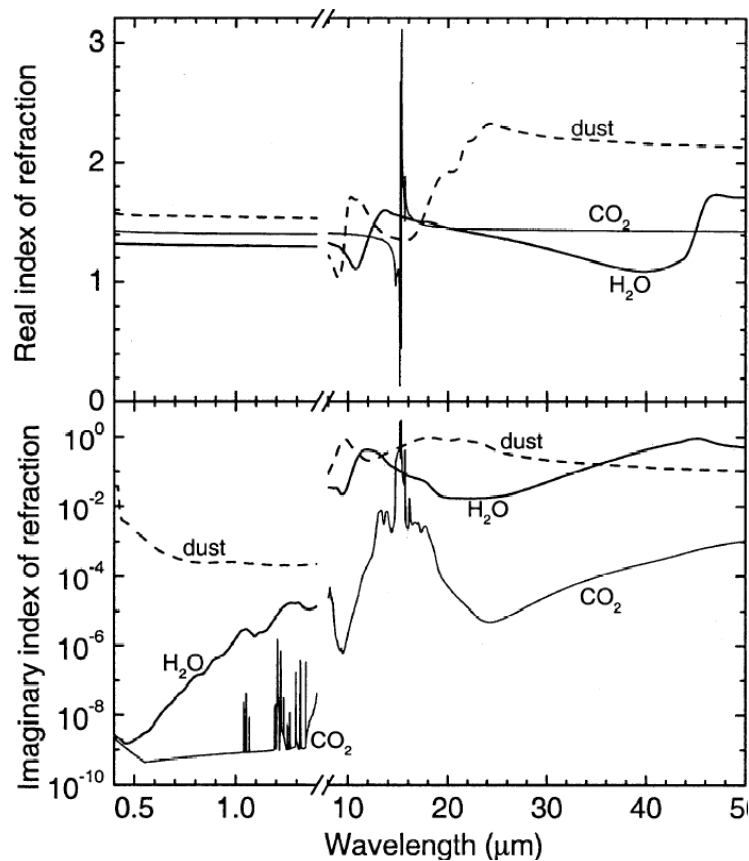


Figure 2.4: The optical properties of CO<sub>2</sub> slab ice (thin line), hexagonal water ice at 150°K (heavy line), and palagonite dust (dashed line) in the visible/near infrared (0.4-1.4 $\mu$ m) and thermal infrared (9-50 $\mu$ m). From Hansen (1999)

high in the infrared for water ice, and relatively high in both ranges for dust. Dust has higher absorption than CO<sub>2</sub> or water ice in the visible, and CO<sub>2</sub> ice has significantly lower absorption in the thermal infrared than water ice or dust.

Solid CO<sub>2</sub> is very transparent, which is quite unusual for geological materials. This leads to peculiar radiative behavior, the so called "solid-state greenhouse effect". The solid-state greenhouse is analogous to the classical atmospherical greenhouse. If a surface consists of the particles which are neither dark nor optically thick most solar radiation passes the surface without being absorbed. The solar radiation (which has a maximum intensity in the visible, see Fig. 2.5) is then absorbed either gradually over a large distance while penetrating downward below the surface, or at some opaque layer below or embedded within the transparent layer. The absorbed energy is then reradiated as infrared radiation. It can not easily escape from most media since most transparent solids have strong absorption bands in the IR. Therefore, in the case of a medium which is optically thin in the visible and opaque in the thermal infrared (as CO<sub>2</sub> ice), energy is deposited below the surface, and thus the average temperature of interior layers should be higher than the average surface temperature.

The importance of such subsurface heating for the behavior of planetary ices was first noted by Brown and Matson (1987) who introduced the name "solid-state greenhouse

effect”.

This effect plays a big role in the cleaning of CO<sub>2</sub> ice and in the formation of spiders. It is discussed in the following chapters.

## 2.2 Spiders in MGS MOC images

### 2.2.1 MOC polar observations

The Mars Orbiter Camera (MOC) is one of the instruments onboard Mars Global Surveyor (MGS) which began mapping operations on Mars orbit on March, 1 1999 ( $L_s=104^\circ$ ) after its launch on November, 7 1996.

MOC has three cameras (one narrow-angle and two wide-angle cameras) that are designed to obtain high spatial resolution images of the surface of Mars and lower spatial resolution, synoptic coverage of the planet’s surface and atmosphere. More detailed description, operations, and primary science objectives for this instrument can be found in Malin et al. (1992) and in general overview of the Mars Global Surveyor mission (Arden et al 2001).

MOC is primarily a telescope that enables extremely high resolution images of selected locations on Mars. Using the narrow-angle (NA) camera, areas ranging from 2.8 km×2.8km to 2.8km×25.2km (depending on available internal digital buffer memory) can be imaged at about 1.4m/pixel spatial resolution. Additionally, lower-resolution images (to a lowest resolution of about 11m/pixel) can be acquired by pixel averaging. These

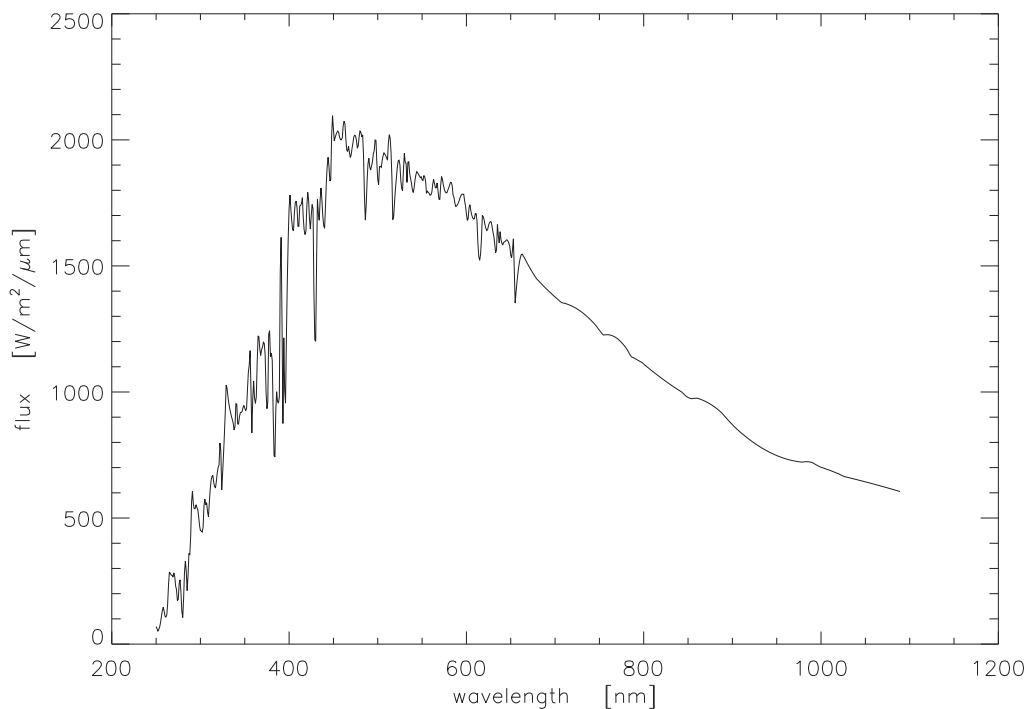


Figure 2.5: Solar flux at 1AU after Kurucz et al. (1984)

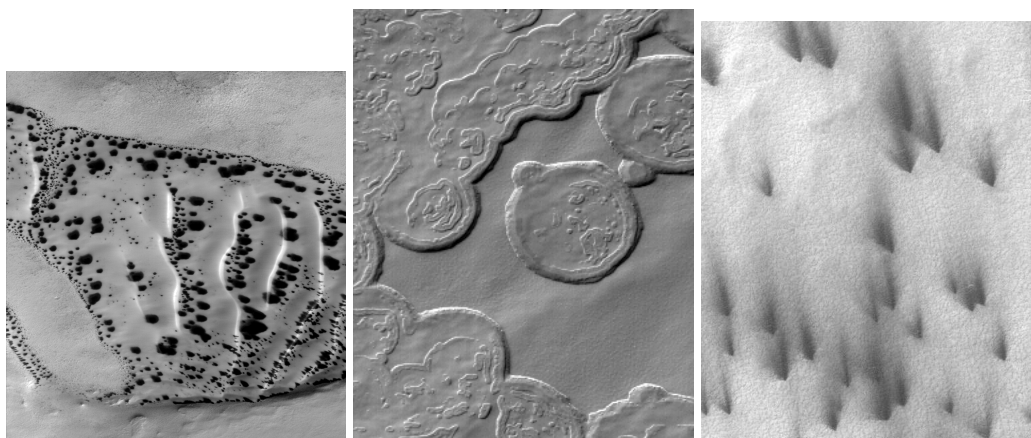


Figure 2.6: a. The subsection of MOC NA camera image M04-01718: image longitude  $9.59^{\circ}\text{W}$ , latitude  $64.87^{\circ}\text{S}$ , scaled image width: 2.80 km, solar longitude  $L_s=190.31^{\circ}$ ; b. The subsection of MOC NA camera image M04-00674: image longitude  $342.24^{\circ}\text{W}$ , latitude  $87.02^{\circ}\text{S}$ , scaled image width 2.82 km, solar longitude  $L_s=186.86^{\circ}$  c. The subsection of MOC NA camera image E07-00829: image longitude  $254.63^{\circ}\text{W}$ , latitude  $85.72^{\circ}\text{S}$ , scaled image width 1.42 km, solar longitude  $L_s=213.76^{\circ}$ .

images can be much longer, ranging up to  $2.8 \times 500$  km at 11m/pixel. High resolution data is used to study sediments and sedimentary processes, polar processes and deposits, volcanism, and other geological/geomorphic processes.

The MOC experiment also consists of two wide-angle (WA) cameras with red (575-626 nm) and blue (400-450 nm) band pass filters (WAR and WAB). The MOC wide-angle cameras are capable of viewing Mars from horizon to horizon and are designed for low-resolution global and intermediate resolution regional studies. Low-resolution observations can be made on every orbit, so that in a single 24-hour period a complete global image of the planet can be assembled at a resolution of about 7.5 km/pixel. Regional areas (covering hundreds of kilometers on a side) may be imaged at a resolution of better than 250 m/pixel at the nadir. Such images are particularly useful in studying time-variable features such as clouds, the edge of the polar cap, wind streaks, as well as acquiring stereoscopic coverage of areas of geological interest. MOC's wide angle color images can be used to distinguish between surface and atmosphere dust and ice clouds. E.g. the more features show up in blue, the more ice they probably contain, since almost everything else on Mars is reddish.

Because of the  $87^{\circ}$  inclination of its orbit, Mars Global Surveyor passes almost over the poles every orbit. Since MGS makes 12.5 orbits per day, it offers great opportunity for mapping the polar areas with all its cameras. Observations at  $3^{\circ}$  of the poles are particularly dense since MGS passes here every orbit. The WA cameras enable global scale monitoring of the polar caps evolution, while the NA camera can provide high resolution images for detailed analysis.

Observations with the MOC NA camera revealed several classes of unusual small scale features inside the South polar regions (Kieffer 2003) which are unlike anything known on Earth. Among these features are:

- dalmatian spots (Fig. 2.6 a.),

- swiss cheese (Fig. 2.6 b.),
- oriented fans (Fig. 2.6 c.),
- spiders (Fig. 2.7).

In the present chapter we discuss observations, distribution, and a model of formation of spider patterns.

The name "martian spiders" was introduced by the MOC team to describe structures that show several branches diverging from one common center. Soon after the first detection they were discovered to be negative topographical features (depressions) - i.e. radial troughs or channels. This unusual shape and appearance of spiders caused a lot of speculation about their origin ranging from carving by running fluid to explanations involving biological species. Here we will try to argue in a favor of a model proposed by H.H. Kieffer (Kieffer et al. 2000). It builds on the specific optical properties of CO<sub>2</sub> slab ice. The description of the model can be found in section 2.4.

The Planetary Data System (PDS) archives and distributes scientific data from NASA planetary missions, astronomical observations, and laboratory measurements. In the present study we used the PDS archives of the MOC images acquired during the full period of MGS operations. Both wide and narrow angle camera images are in the archive and are used for the work.

### 2.2.2 Spider patterns in MOC narrow angle images

Our area of interest surrounds the South pole of Mars and is limited to a minimum latitude of 75°S. All MOC NA images in the PDS archive that cover regions inside this area were checked visually for the presence of spider patterns. Images that contain single spiders, spider arrays, or spider ravines were selected for further analysis. Each of such images was counted as one entry. The archive covers the period from September 1997 to March 2004.

We found 326 images that contain spider patterns (Appendix A).

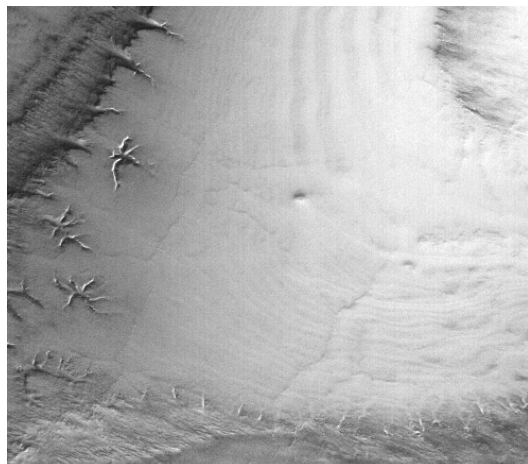


Figure 2.7: The subsection of MOC NA camera image M09-03484: image longitude 177.45°W, latitude 76.83°S, scaled image width 2.84 km, solar longitude  $L_s=243.79^\circ$ . Sunlight is from lower right corner.

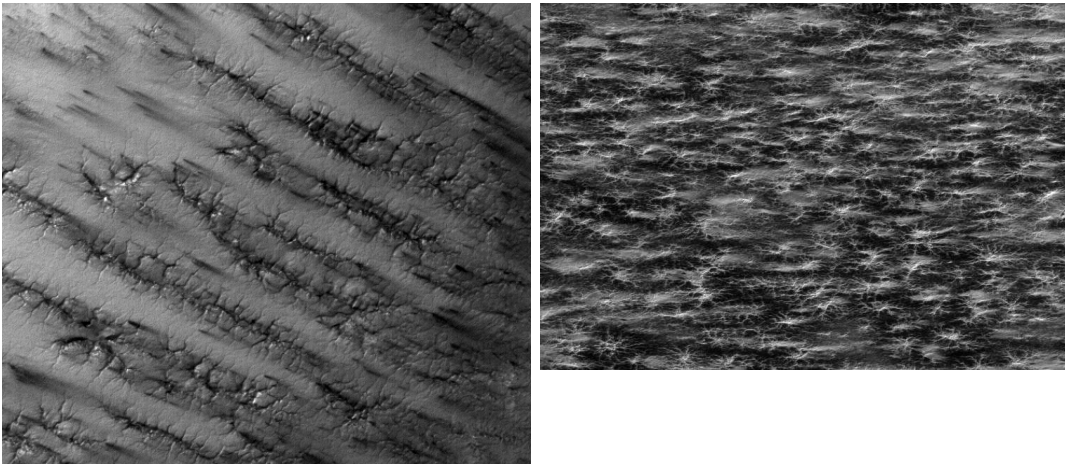


Figure 2.8: Left panel show the subsection of MOC NA camera image m08-03864: image center longitude 209.14°W, latitude 75.28°S, scaled image width is 1.42km, image was taken at  $L_s=226.08^\circ$  with the resolution of 2.76m per pixel. Left panel is the part of MOC image e09-00407: coordinates of image center are 269.72°W, 87.02°S, image width is 2.99km, its resolution is 2.90 meters,  $L_s=247.31^\circ$ .

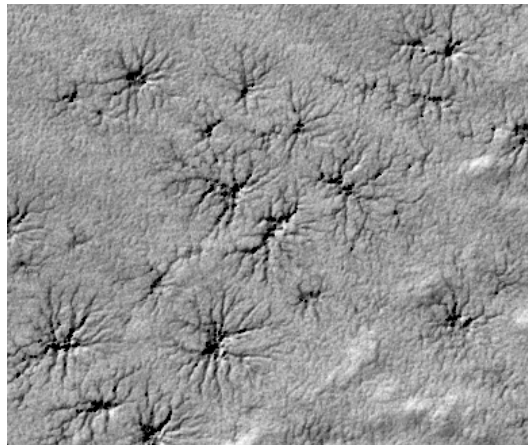


Figure 2.9: The subsection of MOC NA camera image m11-00280. The image was taken at  $L_s=275.04^\circ$  at the location 274.77°W, 86.97° with the resolution of 2.77 meters per pixel, image width is 1.42km. The sunlight illuminates the scene from the upper left corner.

Analysis of these images prove that spider patterns show a lot of morphological variations. They are of different sizes in a range from 40 m to 2 km, have different appearance, form rows or distribute randomly.

First of all, spiders can have both dark or bright albedo features on a correspondingly bright or dark background (Fig. 2.8), or they can look like topographical features, i.e. depressions (Fig. 2.9). Spiders are very often associated with fan structures. Such fans look wind-shaped (Fig. 2.10).

Sometimes spiders form rows that are aligned along a line. An interesting detail here is that they normally are all equidistantly separated from each other (Fig. 2.11). More

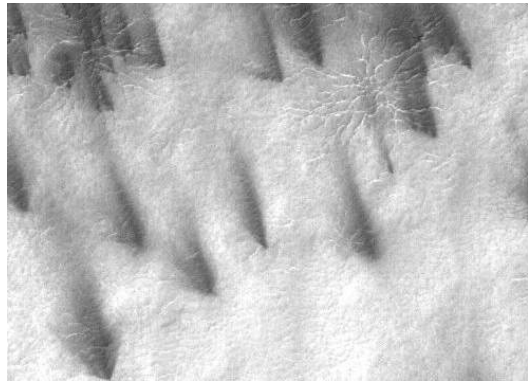


Figure 2.10: The subsection of MOC NA camera image e07-00829. Image location is  $254.63^{\circ}\text{W } 85.72^{\circ}\text{S}$ ,  $L_s=213.76^{\circ}$ , image width is 1.42 km, resolution 2.77 meters per pixel.

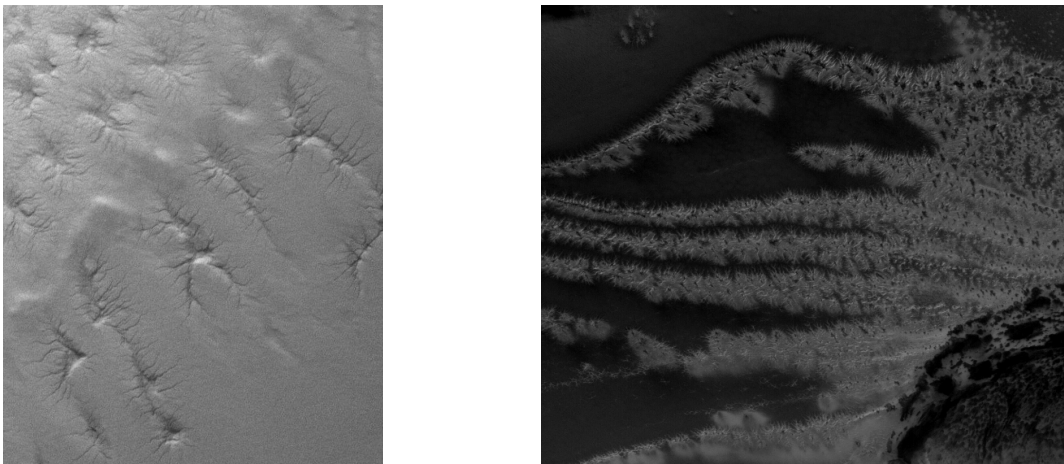


Figure 2.11: The subsections of MOC NA camera image m16-00550 (on the left): image is located at  $187.56^{\circ}\text{W } 73.94^{\circ}\text{S}$ , its resolution is 1.38 meters, width is 1.06km and it was taken at  $L_s=5.24^{\circ}$ ; The subsections of MOC NA image e09-00409 (on the right):  $330.56^{\circ}\text{W } 79.85^{\circ}\text{S}$ , image width is 2.94 km, resolution is 4.35 meters per pixel,  $L_s=247.32^{\circ}$ .

often spiders are distributed randomly over large areas (Fig. 2.9).

Appendix A offers a table which lists MOC images of spiders we found in MOC archive. This table includes the image ID that is used in the Planetary Data System, together with the observation time and image location. The table includes all images that are used for our work. All the conclusions about spiders' properties hereafter were made on the basis of their observations in the South Polar cap. Spiders have not been yet identified in the north.

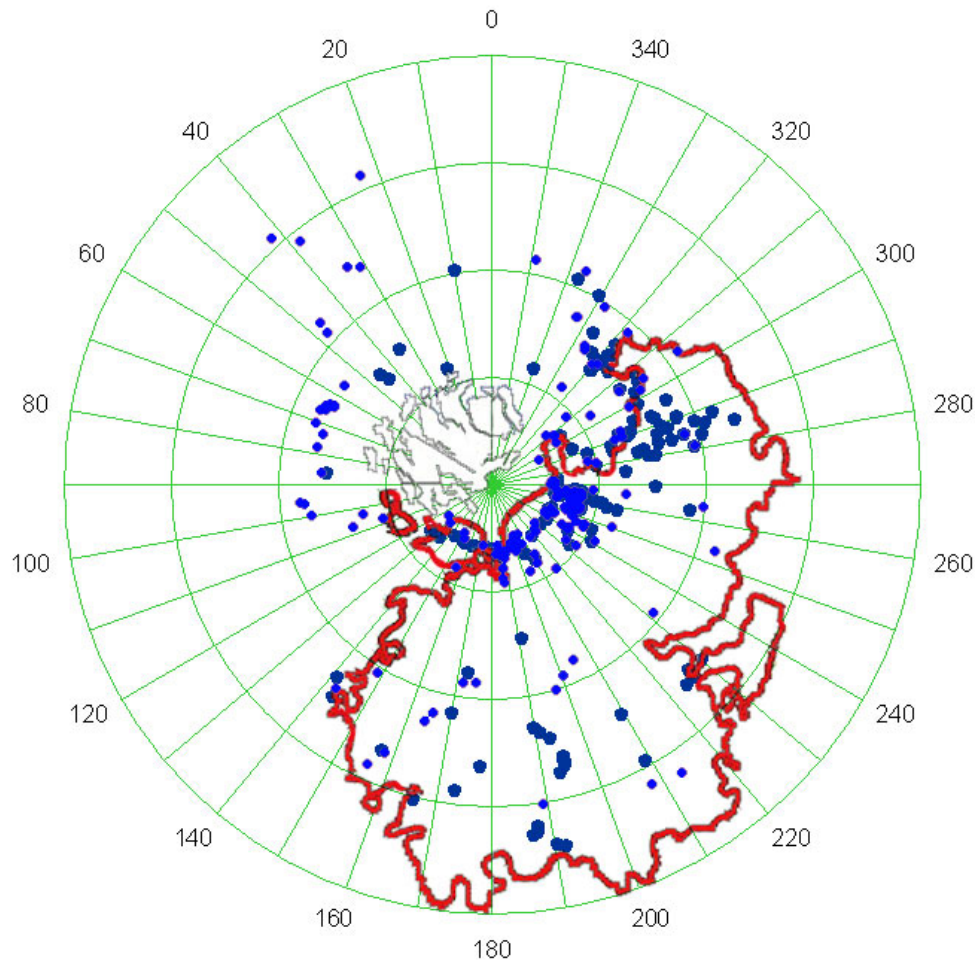


Figure 2.12: Spatial distribution of 327 detected images containing spiders from the South pole down to  $70^{\circ}\text{S}$ . Red line indicates the border of late cryptic region as it is defined by Kieffer et al. (2000).

### 2.2.3 Spatial distribution of spiders. Are all spiders inside the cryptic region?

Piqueux et al. (2003) found that almost all regions where spiders were identified lie inside cryptic region. We checked this hypothesis with our sampling of spiders images. Our selection has more spider images because it includes more recently taken MOC NA data (taken from October 2003 till March 2004).

Fig. 2.12 shows the position of images that contain separate spiders or spider ravines (blue dots) together with the border of the cryptic region as described by Kieffer et al. (2000) (red line). Clearly, quite a number of images lie outside cryptic region defined in this way. However, more accurately this cryptic region has to be called "late cryptic region". As we noted in the discussion of the cryptic region evolution (see chapter 2.1), in the early spring (at approximately  $L_s=175^{\circ}$ ) the cryptic region almost symmetrically occupies all the area around South pole. There is still a lack of data for the area from the

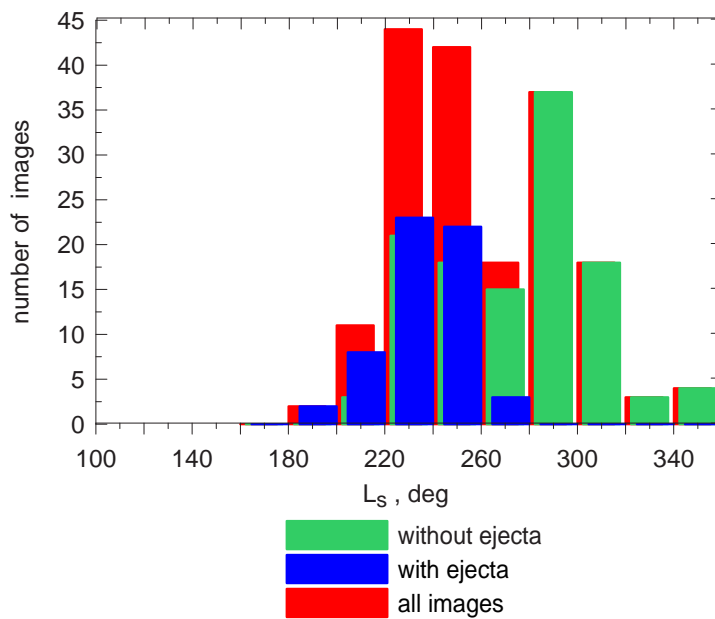


Figure 2.13: Seasonal distribution of detected spiders. Histogram shows number of MOC NA images of spiders with and without fans depending on  $L_s$ .

South pole to  $80^\circ\text{S}$  for that season. In the strict sense we do not know if these areas show cryptic behavior or not.

### 2.2.4 Fan structures, winds and seasonal distribution

As was noted above, spiders are very often associated with fan structures. Examples are shown on figures 2.10 and 2.14 (low panel). Among 178 spiders' images from MOC data archive (except for the last release) about one third (58 images) show fan structures.

Spiders with fan structures show also non homogeneous distribution depending on the season. Fig. 2.13 shows the histogram of spiders' images with and without fans depending on  $L_s$ , i.e. season. Starting from the beginning of the spring (when insolation allows the observations over the South pole) spiders with fans start to appear with roughly the same frequency as those without fans. On the other hand images with fans have not been found after  $L_s=280^\circ$ ) which corresponds to the beginning of summer in Southern hemisphere. All the images that were taken during summer time show spiders without fans. By this time all of the seasonal  $\text{CO}_2$  ice has sublimed away. This means that spiders are active features that evolve while martian season progresses from winter to spring, and then to summer. Hence, main active processes in the areas of spider formation and evolution can be expected to happen during the spring time.

Fans over spiders basically look as if loose material emerged from a local source and was redistributed around the surface by wind. Majority of fans have being shaped in one direction over the considerable area that leads to the conclusion of one preferential direction of winds in this area. If this is a true assumption, generally the direction of the fans should correlate with average wind direction on the spot. As the wind directions from observations for such a fine scale are not available so far, we could only use results

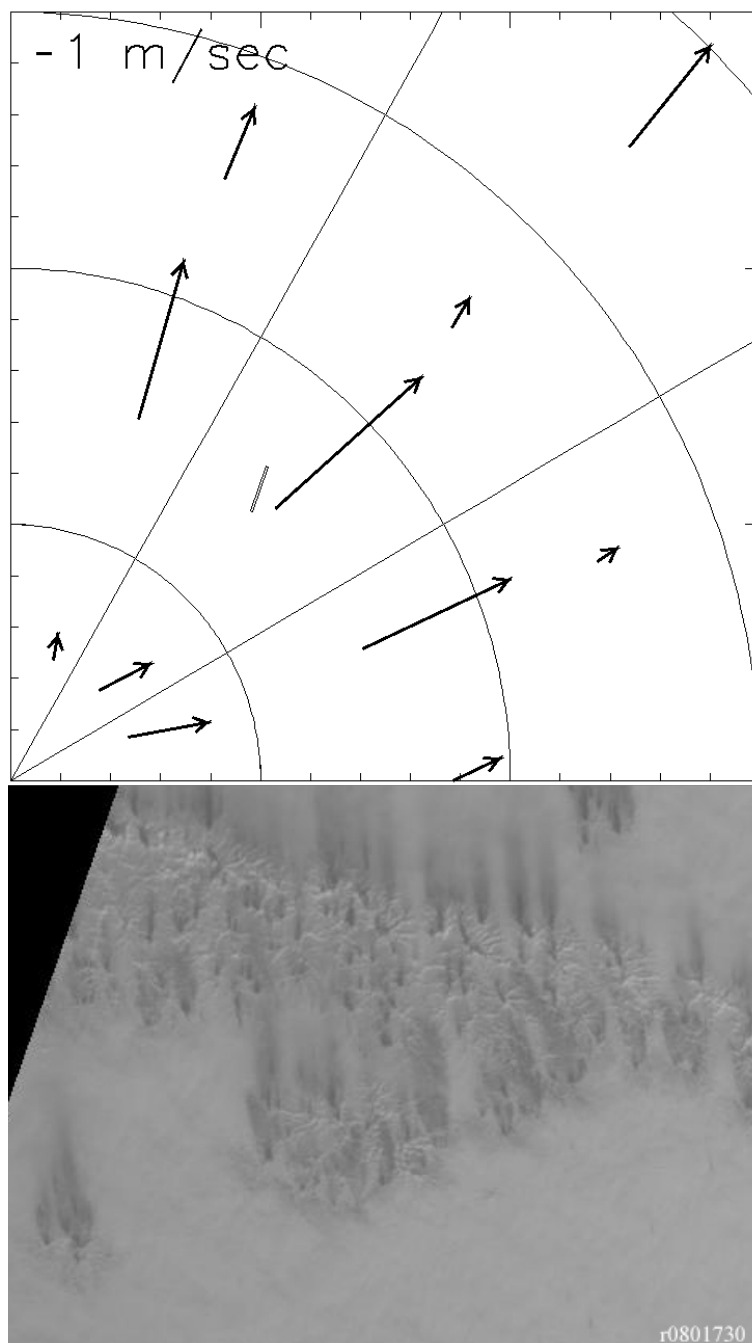


Figure 2.14: Upper panel: the wind direction field from the Martian Climate Database. The small black rectangle in the middle of the plot is the trace of MOC image r08-01730. Lower panel shows the section of this image in the same (polar) projection.

from the models of Martian atmosphere circulation. Fig. 2.14, upper panel, shows the wind direction field taken from the Martian Climate Database (Forget et al. 1999). It is shown for the part of South cap where MOC NA image R0901730 was taken for 0h local solar time at  $L_s=210^\circ$  - time when majority of spiders' images with fans were taken. The small black rectangle in the middle of the plot is the trace of MOC image. The subsection of image itself is shown in the lower panel. The projections of both are polar and we can directly compare the direction of winds and can say that it does not correlate completely but at least winds blow away from the pole and the fans are also oriented northwards. Of course local topography plays a very big role in changing wind directions. Also, the resolution of the Mars climate Database is not sufficient for strong evidence on the question. What we can conclude is that the fan directions are not in contradiction with the mean wind direction over the area.

Some areas containing spiders imaged by MOC several times to allow the study of seasonal or annual changes of spiders. In (Piqueux et al. 2003) one example of seasonal changes of such area with spiders is shown and discussed. The appearance of spiders changes considerably in chosen example while spring progresses to summer in South regions.

In Fig. 2.15 we show the repeated observations of the same place at the location  $265.87^\circ\text{W}$ ,  $86.14^\circ\text{S}$ . Images m09-00157 and e08-01159 were taken with 1 martian year difference. Spiders appear on both images and show no significant annual changes. It may indicate that either seasonal evolution does not change considerably appearance of spiders (at least not so much that it can be noted with MOC imaginary abilities), or that some areas do not exhibit activity as other areas do.

### 2.3 MOLA data of spider areas

The Mars Global Surveyor includes in its payload an optical remote sensing instrument, the Mars Orbiter Laser Altimeter (MOLA). The primary MOLA objective is to determine globally the topography of Mars by generating high-resolution topographic profiles at a precision suitable for addressing problems in geology and geophysics (Smith et al. 2001, Zuber et al. 1992).

MOLA has a diode-pumped laser transmitter that emits 8.5-ns pulses at 100-ms intervals with an initial output power of 40 mJ per pulse. The instrument measures the round-trip time of flight of a  $1.064\text{-}\mu\text{m}$  laser pulse transmitted from the spacecraft to the surface. Combining these data with accurate location and velocity of the spacecraft allows derivation of surface topography. On some pulses, reflections are also received from ice clouds. The receiving optics, a Cassegrain telescope with a 0.5-m-diameter primary mirror, focuses the return signal on a silicon avalanche photodiode detector. At the mapping altitude each laser spot illuminates about 160-m-diameter circle on the surface with a spacing of  $\sim 300$  m (0.1 sec) per spot along the MGS nadir ground track. The range measurements are quantized with 1.5-m vertical resolution before correction for orbit and pointing errors. Relative error in altitude along profiles is 110 m, and the profiles are being assembled into a global grid referenced to Mars center of mass with high absolute accuracy.

There is only limited data available from MOLA for the images from our selection that

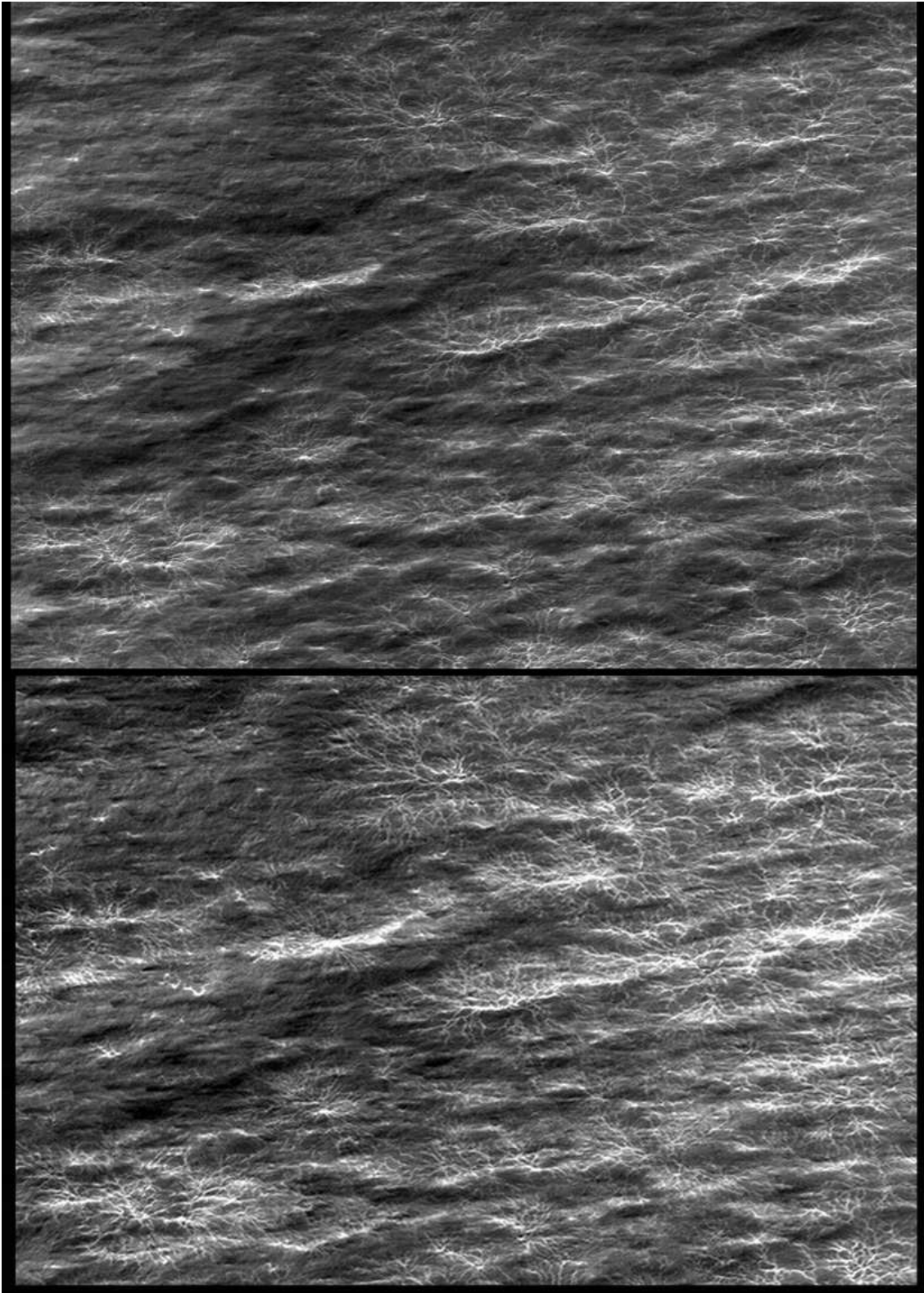


Figure 2.15: The subsections of MOC NA camera images m09-00157 ( $L_s=235.94^\circ$ ) and e08-01159 ( $L_s=238.15^\circ$ ) taken with the time difference of 1 martian year at the same location  $265.87^\circ\text{W}$ ,  $86.14^\circ\text{S}$ .

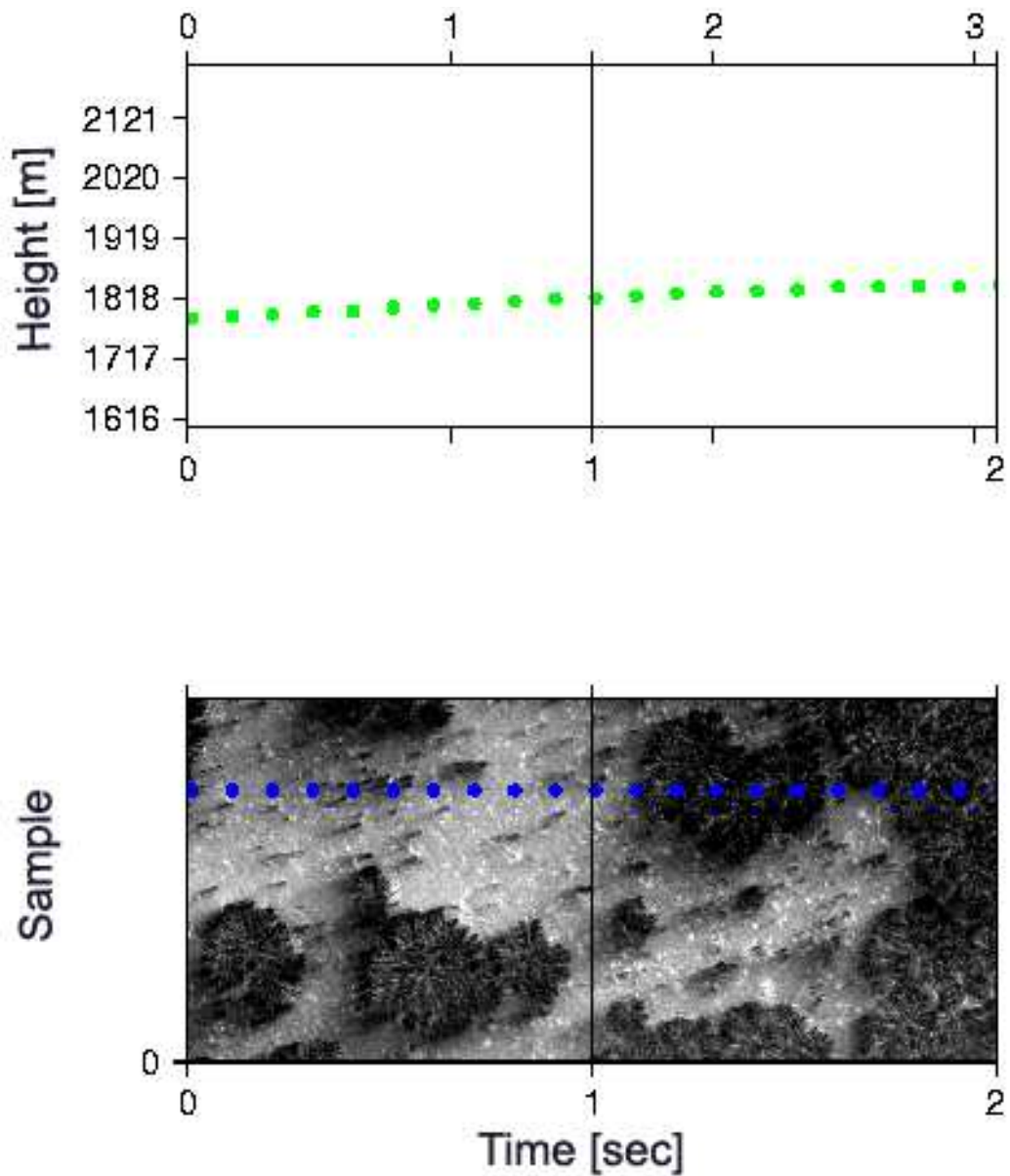


Figure 2.16: MOLA data for the part of MOC NA image M0804688. Although MOLA track crosses a big dark spider the elevation changes through the whole image are less than 1 m.

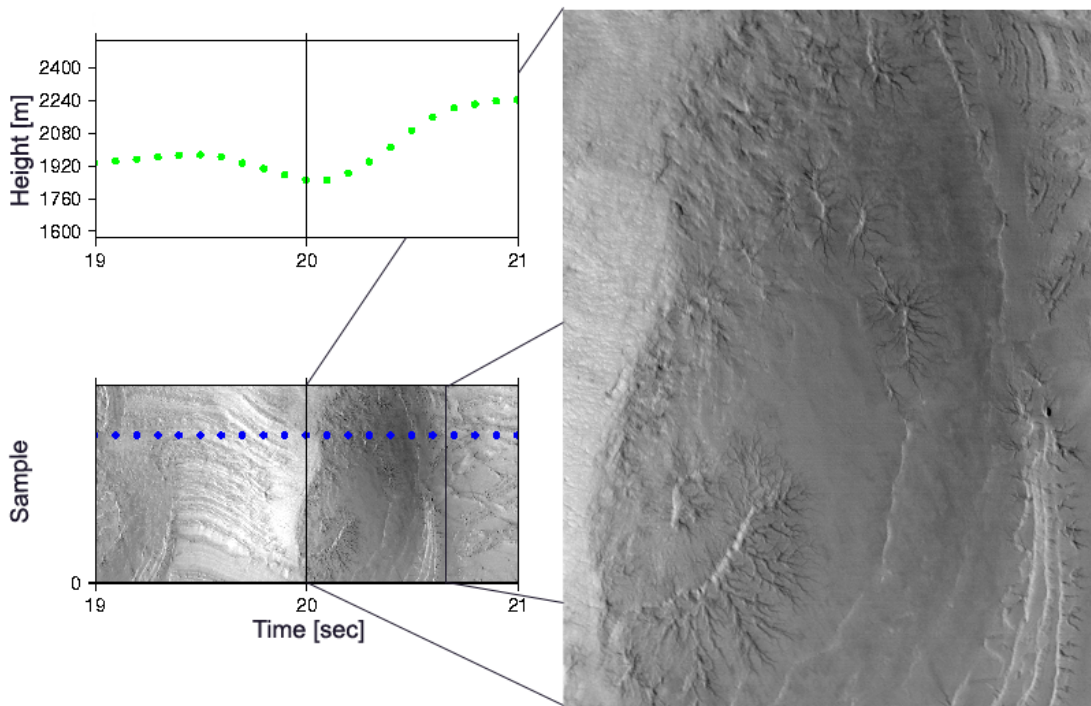


Figure 2.17: MOLA data for the part of MOC NA image M1103360. Several big spiders are situated on the walls of valley.

show spiders. MOLA usually took the track along the MOC image, but not necessarily the side where spiders are. Some general conclusions from analyzing MOLA tracks of spiders areas are:

- Majority of spiders with average diameter  $\sim 300\text{m}$  are too small to be resolved by MOLA.
- The only thing we can see in this case is the context topography of the area where spiders are situated.
- Usually, the area surrounding spiders is flat.

Some big spiders can be resolved by MOLA and usually in this case they do not stand out of context topography significantly. From shadows on MOC images spiders are known to be depressions. Example in the Fig. 2.16 shows large dark spiders on the much lighter background. The MOLA track shows that area is very flat and elevation changes through the whole image are less than 1 m.

Another point that can be clarified from MOLA data is that spiders can appear on inclined surfaces. Their branches can go both uphill and downhill. This supports the hypothesis that they are not formed by flow or other gravitationally-bound processes. For example, figure 2.17 shows several big spiders situated on the steep slope of 13 deg. The spider has branches in both - downhill and uphill direction. Fig. 2.18 also shows spiders (with fans) on two opposite walls of depression.

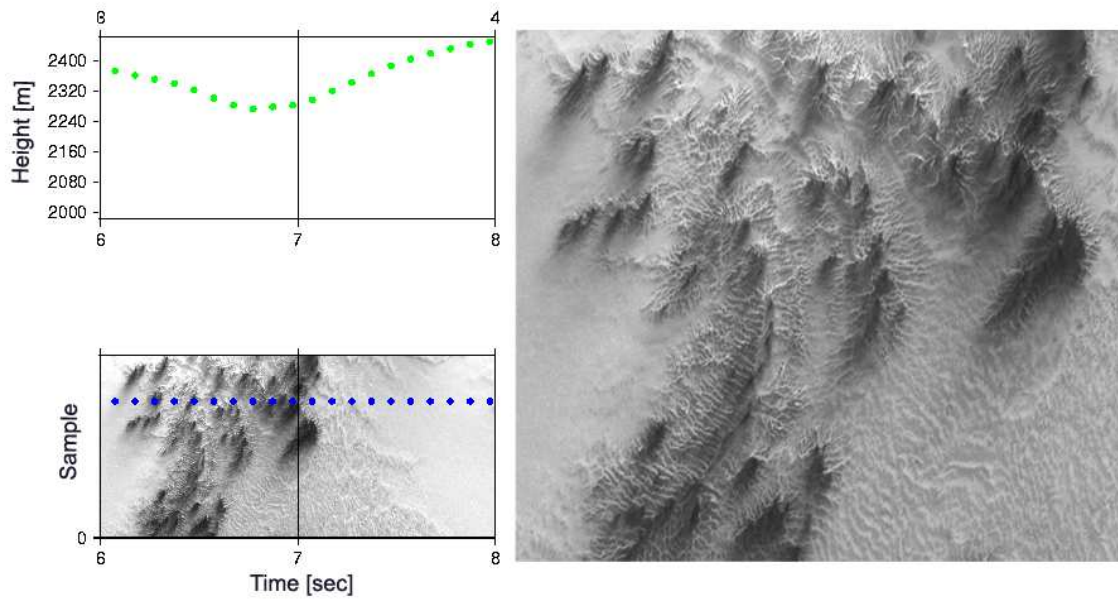


Figure 2.18: MOLA data for part of MOC NA image M0307160. Spiders with fans are visible on the walls of the depression.

## 2.4 Conclusions

The most important observation facts on spiders are:

- sizes range from 40 m to 2 km;
- spiders are found only in South polar regions. They were neither found in other places on Mars nor on other planets;
- spiders are found southwards of  $70^{\circ}\text{S}$  and are concentrated in the cryptic region;
- spiders often show fan structures;
- spiders with fans have not been found after the beginning of local summer;
- the direction of fans coincides with the direction of local winds;
- usually, the area surrounding spiders is flat;
- spiders can form on inclined surfaces.

We intend to explain all the discussed properties of spiders with the formation model that we discuss in section 3.

## 3 Modeling of spiders

### 3.1 Formation of spiders

In 2003 H.H. Kieffer proposed a model for the formation of spiders Kieffer (2003). He based his model on a combination of specific optical properties of CO<sub>2</sub> slab ice and insolation conditions of the cryptic region during spring time. The formation process is divided into 3 stages:

1. Formation of CO<sub>2</sub> slab ice with dust.
2. Ice cleaning due to solar insolation.
3. Breaking the ice by sub-glacial pressure and formation of channels.

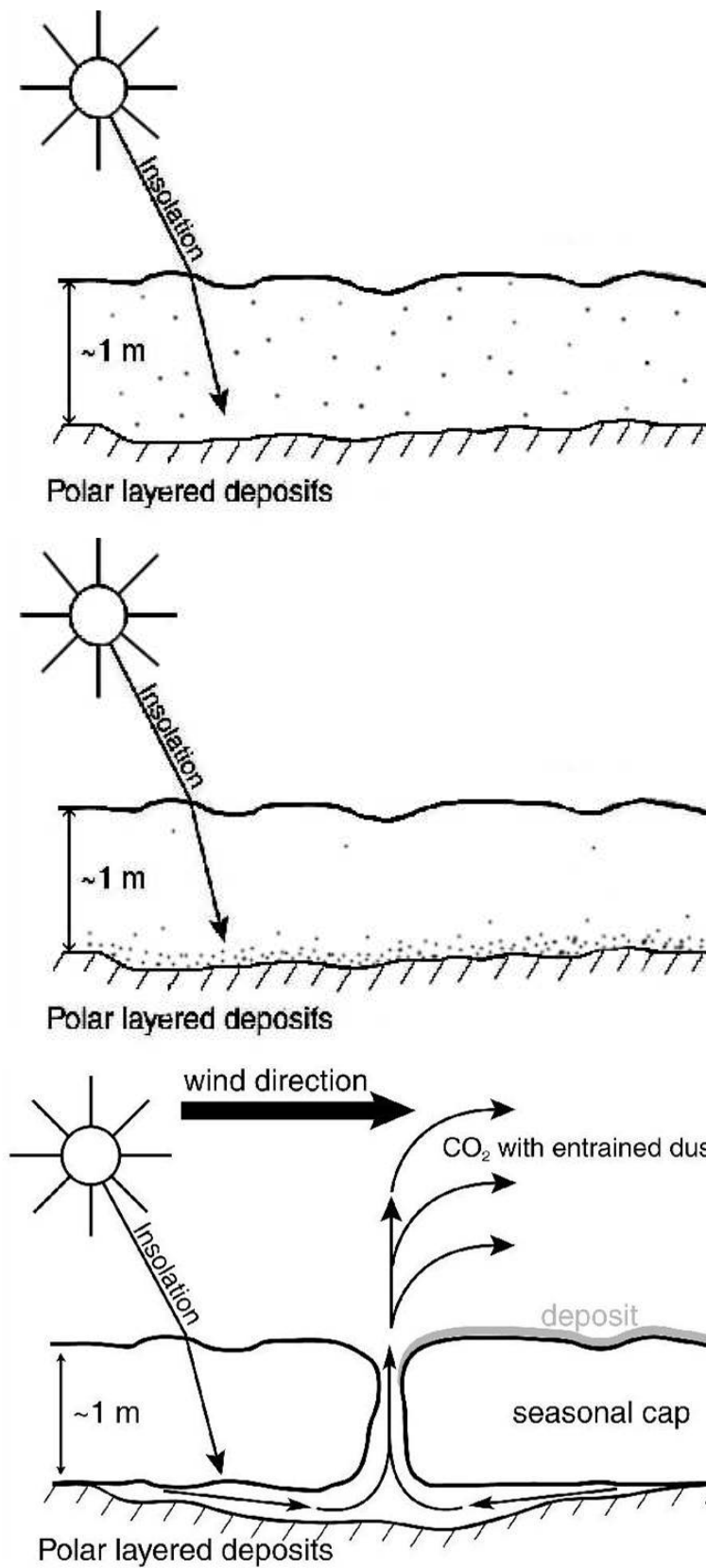
A more detailed description of these stages is given directly below. After this we will offer a quantitative formulation.

#### Dust embedded in CO<sub>2</sub> slab ice

The Martian atmosphere always contains some dust suspended in it. During winter time, a seasonal CO<sub>2</sub> ice cover forms over the polar region. The condensation of CO<sub>2</sub> may take place on the surface or in the atmosphere. In the latter case it will later precipitate to the surface as snowfall (Forget et al. 1998). Dust grains serve as condensation nuclei for growing CO<sub>2</sub> crystals, and independent of which process forms the ice, dust precipitates from the atmosphere to the surface. As a result, a certain amount of dust is embedded in the forming ice (Fig. 3.1, upper panel).

#### CO<sub>2</sub> ice cleaning

Dust grains rest in the ice until the Sun rises over the horizon during spring time. Since CO<sub>2</sub> is very transparent for solar radiation (see chapter 2.1.2) most of it is absorbed by the embedded dust. As a first approximation, one could presume that all solar radiation is absorbed by dust grains but not in the ice. We also assume that all of the absorbed energy will go into sublimation of ice around the dust grain (Fig. 3.3). If the grain absorbs enough solar radiation, then a high-pressure gas pocket will form around it. The warm grain can not be in direct contact with solid CO<sub>2</sub>, it has to rest on the layer of gas. If the gas bubble, with its dust grain inside, is close to the top of the slab - the bubble can rupture. If not, it will move downward through the solid ice. Gas in the upper part of the bubble receives little heat from the dust grain and freezes again. Therefore, vertical vents that the grain leaves after its passage downward will close. The solar flux at the bottom of the slab is smaller than in upper part of it, therefore dust grains high in the slab get more radiation and thus move faster than grains lower down. This concentrates the dust in the



during early spring, the dust is suspended in the slab of CO<sub>2</sub> ice

as the Sun gains strength, the dust gradually sinks downward through the ice

after some time the CO<sub>2</sub> ice starts sublimating starting at the bottom thus creating geyser-like phenomena

Figure 3.1: Model of spiders' formation by Kieffer (2003).

lower part. In this way the ice is eventually cleaned from dust and the dust accumulates at the bottom of the slab (Fig. 3.1, middle panel).

### Ice breaking, formation of vents, channels and fans

While the dust moves downward, it continues to absorb more solar radiation than the ice around and above it. Thus, the sublimation zone moves down with the dust grains.

Dust settled at the bottom continues to heat the ice. This in turn creates rise in pressure under the ice. This pressure can possibly grow high enough to break the ice plate after which the pressure releases through the formed vents. During the escape, the gas will move loose material from under the ice and eject it on top of the ice. The process resembles geyser. Velocities under the slab will depend on the geometry of the flow. In the circular symmetric case the average velocity must initially decrease away from the vent. However in reality symmetric case is unlikely to be stable especially because topography below the ice is never perfectly flat. Most probably channels will develop. The moving gas removes the material below the ice and redistributes it on top of the slab. The fans visible in the MOC NA images may have formed in this way (Fig. 3.1, lower panel).

## 3.2 Simulations of CO<sub>2</sub> ice cleaning process

### 3.2.1 Insolation of the South polar region

Seasonal insolation governs various processes on the polar caps. The amount of solar radiation that falls on a unit area of the surface per unit of time depends on the geographical location and season. A first approximation is:

$$E = S_c(1 - A) \cos(\mu_0) \exp\left(\frac{-\tau}{\cos(\mu_0)}\right) \quad (3.1)$$

where  $S_c$  - is the solar constant at the distance of Mars,  $A$  - is the surface albedo,  $\mu_0$  - the zenith angle of the Sun, and  $\tau$  - the atmospheric opacity.

The solar zenith angle at a given time of day can be calculated from the maximum height of the sun on that particular day. The maximum height of the sun as a function of latitude  $\varphi$  and  $L_s$  is:

$$h = \frac{\pi}{2} - \varphi - i \cdot \sin(L_s) \quad (3.2)$$

where  $i = 25.19^\circ$  - is the Mars' obliquity of the polar axis relative to the orbital plane. Using 3.1 - 3.2 we calculate incoming energy at a given latitude for a given time of the year.

Fig. 3.2 illustrates the insolation conditions in the polar regions of Mars. High latitudes - i.e. higher  $75^\circ$  - in winter have periods, when Sun does not rise over the horizon - i.e. they are in the polar night. From the beginning of spring the Sun starts to rise above the horizon on increasingly higher latitudes. When the summer approaches, the polar day will begin. This is the time when the Sun is above the horizon continuously. For example, at latitude  $85^\circ$  it begins around  $L_s = 205^\circ$ .

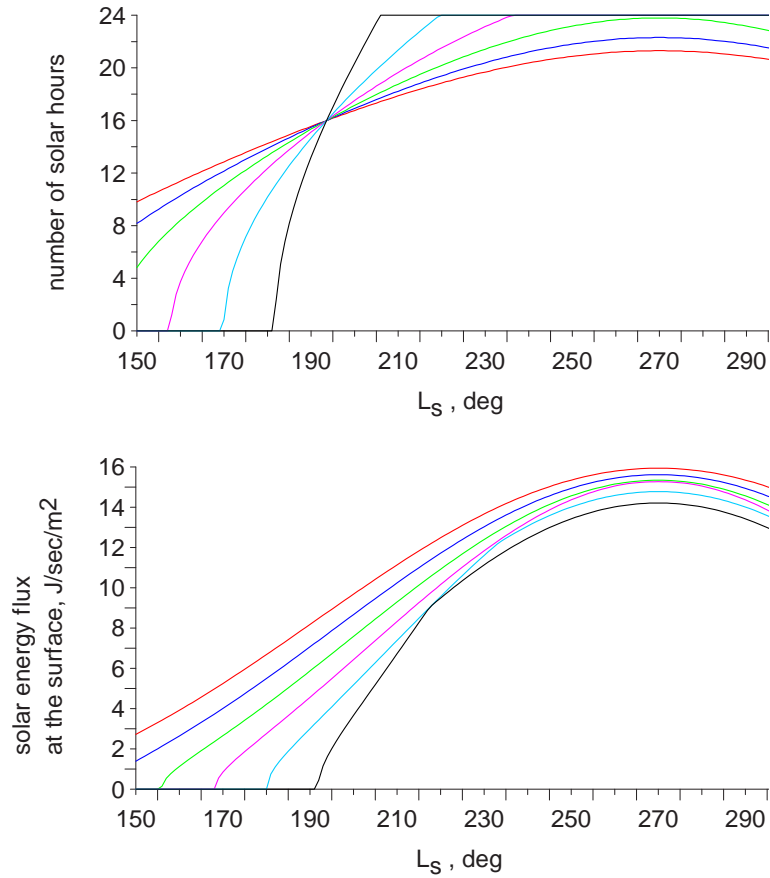


Figure 3.2: Number of solar hours and solar flux at the surface of the polar regions. Curves correspond to different latitudes: red -  $\varphi = 60^\circ$ , blue -  $\varphi = 65^\circ$ , green -  $\varphi = 70^\circ$ , magenta -  $\varphi = 75^\circ$ , sky-blue -  $\varphi = 80^\circ$ , black -  $\varphi = 85^\circ$

Using equation 3.1 we calculate the energy that is received by a CO<sub>2</sub> slab ice and dust grains inside it.

### 3.2.2 Single particle modeling

Let us assume that a single dust particle is embedded in a slab of ice. We assume that the CO<sub>2</sub> slab ice initially is 1 m thick. This is represented by the two dimensional simulation box with size: 1m per 1cm.

We consider two types of dust grains: spheres, and cylinders with a height/radius ratio = 0.1. The particles have: radius  $r_p$ , material density  $\varrho$ , and the position  $(x_p, z_p)$  in the slab. We chose the x-axis to be horizontally along the simulation box, and z - vertical, with zero on the bottom of the box.

First of all, we need to know the amount of energy that our particle can get from solar radiation that passed through the atmosphere and ice above it. Equation 3.1 gives the solar radiation per unit area on the top of slab ice. Taking into account attenuation of energy inside the ice, each dust particle will get an energy  $E_p$ :

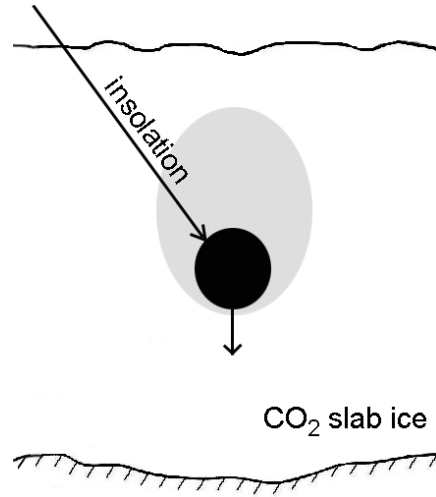


Figure 3.3: Dust particle inside a slab of ice.

$$E_p = s_p \cdot E \cdot \exp\left(\frac{-4 \cdot \pi \cdot R_{CO_2, \lambda} \cdot ds}{\lambda}\right) \quad (3.3)$$

where  $s_p$  is the cross section of the dust particle exposed to the sun, the energy  $E$  is calculated from equation 3.1,  $ds$  is the path length light travels inside the ice before it reaches the dust grain,

$$ds = \frac{1 - z}{\sin(h)},$$

and the last exponential term represents the absorption of light inside the ice.

For the spherical dust grains,  $s_p$  is always  $s_p = \pi r_p^2$ . While for an irregular particle  $s_p$  depends on the position of the sun. As an example of irregular particles we here consider cylinders with a height/radius ratio = 0.1. These can be tilted to the vertical axis and the amount of solar radiation that such particles get depends on the angle between its axis and the direction to the sun. Denoting this angle as  $\mu$ , the  $s_p$  will have an additional term and can be calculated as

$$s_p = \pi r_p^2 \cos(\mu)$$

The radiation which a particle receives first immediately after sunrise is used to heat particle from the temperature of the surrounding ice up to the temperature of CO<sub>2</sub> sublimation, and only then for the sublimation of ice around the particle.

The amount of energy needed for heating the dust grain, and hence the time needed for that, is rather small. The duration can be calculated as

$$t = V_p s_{reg} dT / E,$$

where  $V_p$  is the particle volume, and  $s_{reg}$  is the specific heat of material from which the particle consists. For our calculations here, we use the specific heat of regolith. The heating of dust grains does not take a lot of time: to heat a 1mm sized particle will take

parameter	value	units
solar constant on Mars	$S_c = 588.98$	J/sec/m <sup>2</sup>
gravity constant on Mars	$g = 3.758$	m/sec <sup>2</sup>
ice albedo	$A_{ice} = 0.8$	
regolith albedo	$A_{reg} = 0.25$	
regolith density	$\rho = 3.0$	kg/m <sup>3</sup>
specific heat of regolith	$s_{reg} = 0.40 \cdot 4.184$	J/g/K
specific heat of dry ice	$s_{ice} = 0.205 \cdot 4.184$	J/g/K
latent heat of vaporization CO <sub>2</sub>	$L = 635.0$	J/g
CO <sub>2</sub> ice density	$\rho_{ice} = 1.56$	kg/m <sup>3</sup>
particle mode radius	$r_m = 0.4$	$\mu\text{m}$
effective radius of particles	$r_{eff} = 1.8$	$\mu\text{m}$

 Table 3.1: Parameters for the CO<sub>2</sub> ice cleaning model.

less than 1 second. At later times the radiation that the dust grain absorbs will go into sublimation of ice. We assume that all radiation goes into sublimation of the ice directly underneath the grain only. Thus, ice does not sublime above or on the side of the particle. With such an assumption, we can calculate the amount of ice that is sublimed and hence the distance the particle can sink down:

$$dz = \frac{m_{ice}}{\rho_{ice} \cdot \pi r_p^2} \quad (3.4)$$

and  $m_{ice}$  is calculated as:

$$m_{ice} = \frac{E}{s_{ice} \cdot dT + L}, \quad (3.5)$$

where E is calculated from equation 3.3,  $s_{ice}$  is the specific heat of dry ice, L is the latent heat of vaporization of CO<sub>2</sub>,  $dT$  is the difference of mean ice temperature and the temperature of ice sublimation. As this difference for Martian polar conditions is very small (about 1-2K), the first term in the denominator of the last equation can be neglected.

Using equations 3.1 - 3.4 we calculated the path of sinking dust grains through the CO<sub>2</sub> slab ice. Dust grains in our simulations are either spherical, or are cylindrically shaped with height to radius ratio of 0.1. Cylinder-shaped particles are tilted from the zenith by 10°, 30°, 60°, or 90°. Radius of all particles is 2.5  $\mu\text{m}$ . Cylinder-shaped particles were chosen to introduce some degree of skewness, especially, for contrast with spherical grains. We can not expect real dust grains to have spherical shape. Therefore, non spherical particles may help to estimate how skewness affects the sinking rate and general duration of ice cleaning.

The amount of Solar radiation depends on the location (mainly latitude), here we present results for the latitude 75°S, unless the opposite is mentioned. This latitude is still inside the cryptic region but on its northern edge. All other parameters that were used for the calculations are summarized in the table 3.1.

Figure 3.4 shows the simulated motion of dust grains inside slab ice. Curves show the distance from the top of the slab to the dust grain center versus time. The simulation

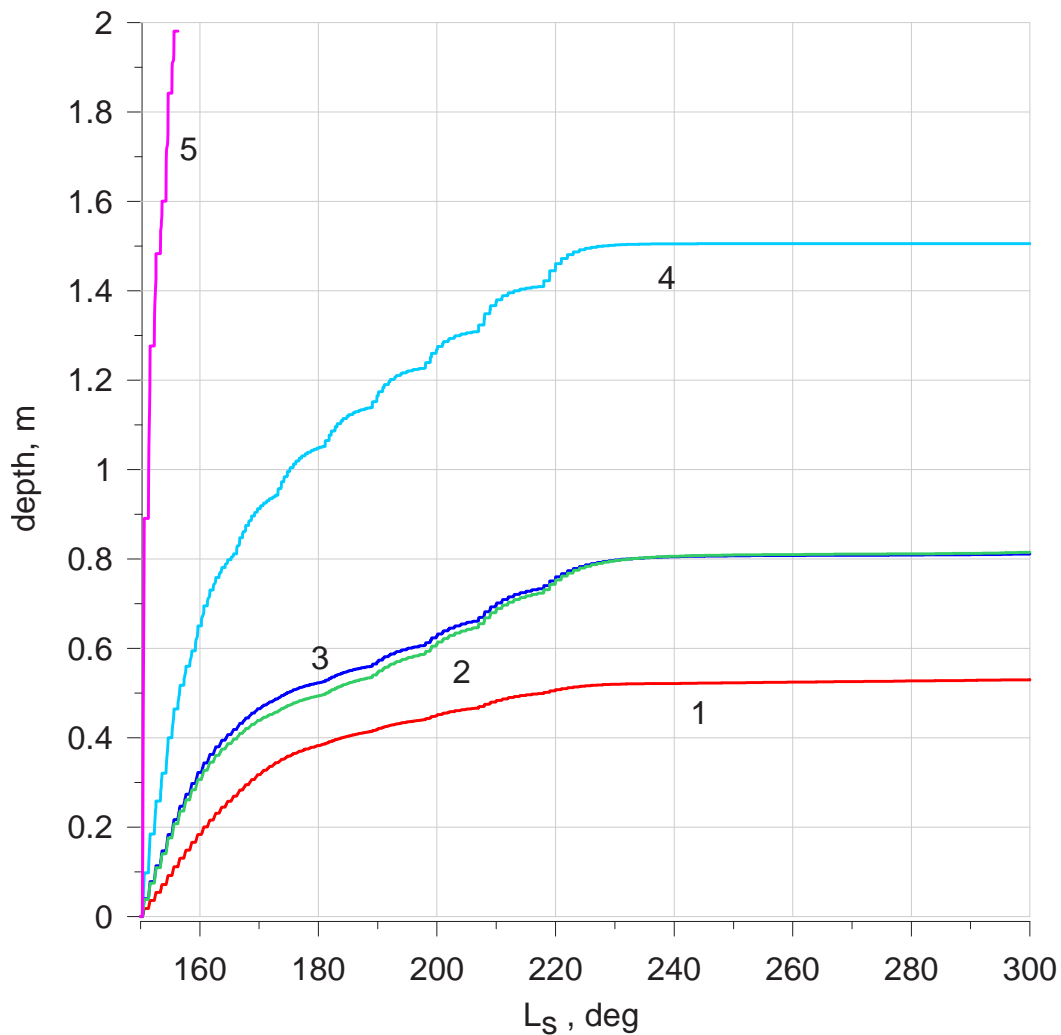


Figure 3.4: Distance from the top of the slab to the dust grain center versus time for the discussed grains. 1: cylinder tilted by 90° from zenith, 2: cylinder tilted by 60°, 3: cylinder tilted by 30°, 4: sphere, and 5: cylinder tilted by 10°.

starts at the beginning of Southern spring ( $L_s = 150^\circ$ ), near the time when Sun first appears above the horizon at the considered latitude of 75°S. Calculations were made until Southern summer ( $L_s = 300^\circ$ ).

Plotted curves are for:

- 1) cylinder tilted by 90° from zenith,
- 2) cylinder tilted by 60°,
- 3) cylinder tilted by 30°,
- 4) sphere, and
- 5) cylinder tilted by 10°.

Curve 5 shows very fast sinking. It corresponds to the cylinder shaped dust grain which is tilted 10° to the zenith, which moves down very rapidly. Obviously since it has the smallest amount of ice below it and thus needs the smallest amount of energy to sublime it. Moreover, its orientation yields the largest absorption of solar radiation;

i.e., the Sun is near the horizon, and the dust grain, since it stands almost vertically, is almost perpendicular to the rays of the Sun. As a result of this, particles can travel through 1 meter of ice in less than 5 days, even at the beginning of spring when the amount of solar hours per day is still very small. The sun is generally very low over the horizon in polar areas, this is especially true for the beginning of spring. Other cylindrical particles (curves 1-3) receive less energy and also have bigger amount of ice below them to sublime. Therefore, they move much slower, and horizontally-oriented particles (curve 1) move slowest of all. They reach only 40 cm depth in 50 days. Spherical particle represents intermediate speed of sinking (curve 4). It can travel through 1 m of ice in less than 30 days.

The conclusions for this calculations are:

- sinking rates highly depend on the shape and orientation of dust grains;
- spherical particles show intermediate sinking rates among other shapes;
- spherical particles can reach the bottom of the expected 1 m thick layer of ice in relatively short time (about 20 days) after the beginning of spring.

The latitude of the place is important since the amount of solar radiation that reaches the surface strongly depends on it. Fig. 3.5 shows the sinking rate of a cylinder particle (cylinder shape,  $30^\circ$  tilt to zenith) if it is situated at different latitudes  $75^\circ\text{S}$ ,  $80^\circ\text{S}$ , and  $85^\circ\text{S}$ . Clearly, the motion of the particle is driven by insolation: the curve for the highest latitude is steepest because during spring the solar energy flux increases fastest for the highest latitudes (Fig. 2.5). This implies that despite the Sun rising later at regions closer to the pole, the dust grains there still have enough time to sink to the bottom of ice slab as we will see below.

While the dust grain sinks downward, the upper part of ice heats up and sublimates away. Due to its transparency, the process is quite slow, but nevertheless still noticeable. We calculated the  $\text{CO}_2$  ice sublimation rate with the same assumptions that we used for ice sublimation under the dust particle using the equation 3.5. The only difference is that energy income  $E$  is from direct Sun insolation, and it was calculated from equation 3.1 using for  $A$  albedo of  $\text{CO}_2$  ice.

For our model it is essential to compare two rates: how fast particles sink down and how fast the slab shrinks from the top. Figure 3.6 shows such a comparison. Curve 1 depicts the depth of the cylindrically-shaped grains that are horizontally oriented, curve 2 is for the spherical particle (the same as curves 1 and 4 in the Figure 3.4). Dashed lines represent the sublimation rates of ices with different albedos.  $\text{CO}_2$  ice albedo strongly depends on the amount of dust that is suspended inside. Therefore, we calculated sublimation rates for 3 albedo values: 0.3 - very dirty ice (albedo similar to that of the martian regolith), 0.6 - ice with considerable amount of dust, 0.9 - extremely clean  $\text{CO}_2$  ice.

If the thickness of an ice slab is 1 m, as it was assumed above, then spherical grains sink to the bottom faster than the overlying ice sublimates away. This result is independent of the albedo of the ice. For asymmetrical particle the situation is opposite: it will never reach the bottom of the ice simply because the ice will disappear faster than the particles able to travel downward through the full ice depth. We expect that, in reality, the sinking rate of most dust grains will be somewhere between that of 1 and 2 in Fig. 3.6. This means that downward velocity of ice sublimation and dust sinking are comparable. However, the initial estimates show that during the beginning of spring the dust sinking rate is faster than the ice sublimation rate. This allows to create at least a layer of dust-free ice, or for

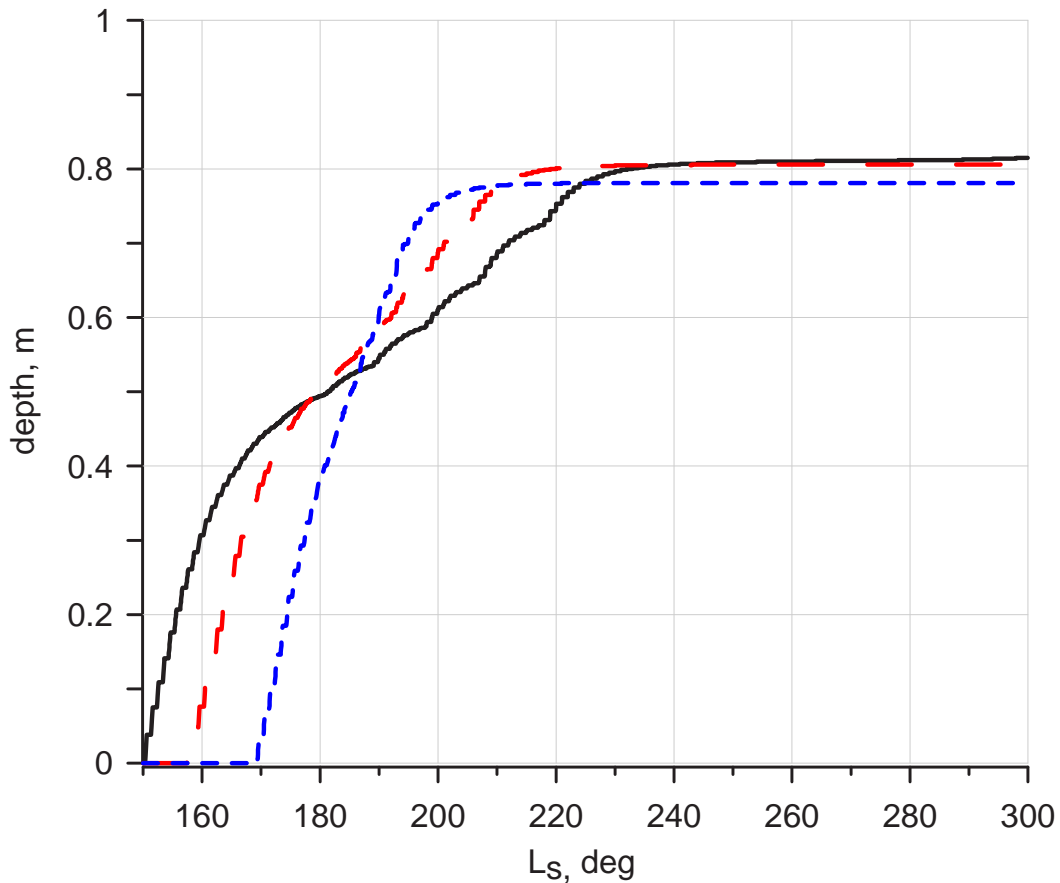


Figure 3.5: Sinking rate for cylindrical dust particle with a tilt of  $30^\circ$  with the zenith for different latitudes: black -  $75^\circ\text{S}$ , red -  $80^\circ\text{S}$ , blue -  $85^\circ\text{S}$ .

the case of spherical dust grains, even a slab of ice that is fully clean.

All the estimates we gave until now, consider a single dust grain in a large slab of CO<sub>2</sub> ice. Of course, in reality, there will always be many. This may have an impact on the time that it takes the dust grains to sink down, most of all since the grains can shade each other. In another words until now we considered optically thin regime, in the next chapter we will consider optically thicker cases.

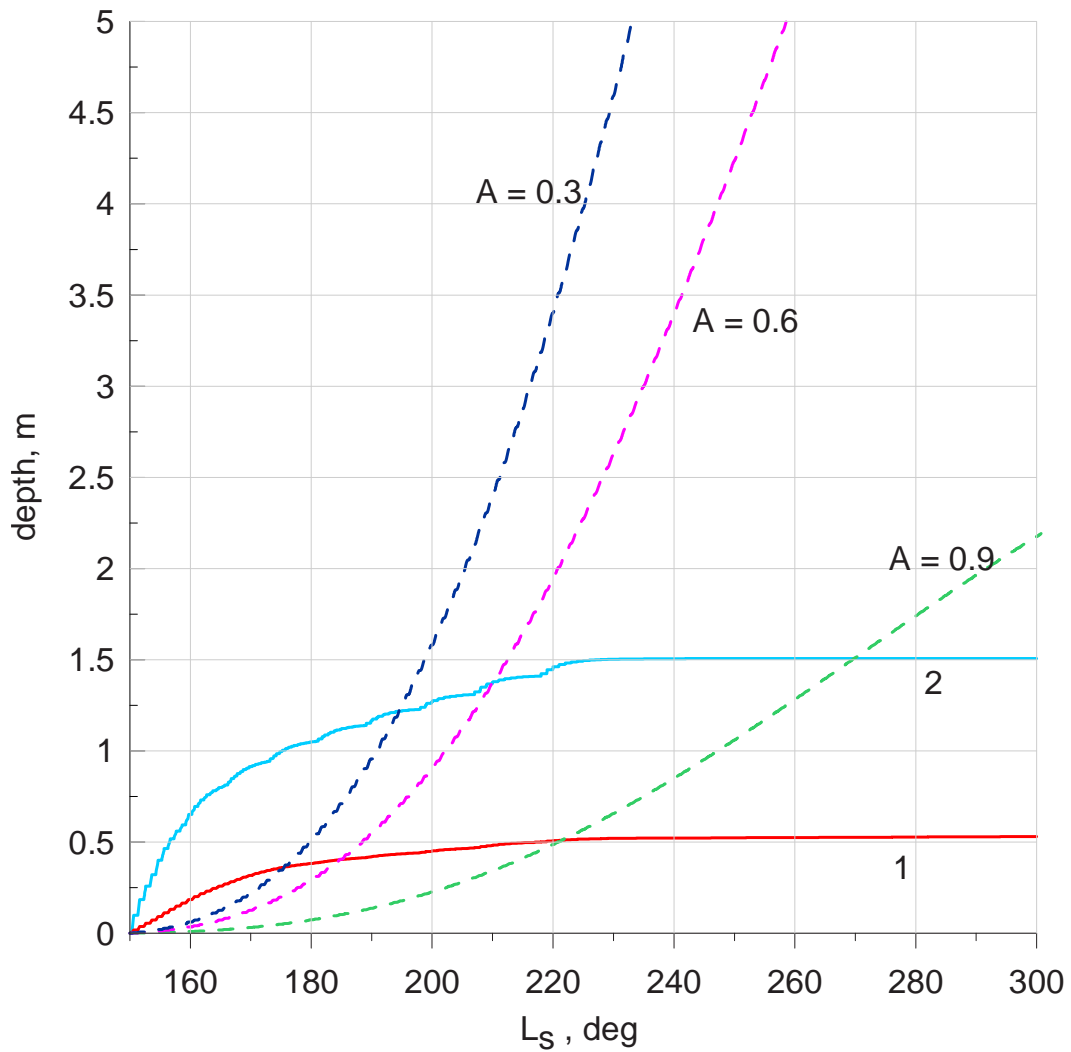


Figure 3.6: The sublimation of CO<sub>2</sub> ice versus time is shown by dashed lines for three different values of ice albedo. Two curves from Figure 3.4 are over plotted here: 1) cylinder tilted by 90° from zenith, and 2) spherical dust particle.

### 3.2.3 Dust inside an ice slab

Atmospheric dust is very important for the Martian climate. The suspended dust interacts with both visible and infrared radiation, modifies atmospheric heating rates and changes the albedo of Martian surface through sedimentation.

Formation of slab ice at South polar regions occurs simultaneously with dust sedimentation during the winter season. The dust sedimentation rate is a critical parameter for our model of CO<sub>2</sub> ice cleaning. That is why we decided to pay more attention to this point. Unfortunately there are only limited observational data for dust sedimentation especially - for the Southern pole. Mainly due to specific insolation conditions but also because there have not been any lander in the Southern hemisphere high latitudes. Table 3.2 summarizes estimations on dust deposition rates from literature.

Deposition rates estimated starting with the same assumptions and using same method can differ by orders of magnitude. These differences originate in the observational data. For example, Pollack et al. (1979) calculate dust deposition rate from precipitation during a dust storm. Thus using the averages for the whole planet may yield very different deposition rates than using regional values. Especially near the poles the local values may be quite different from the planet average. Also one always needs to make assumptions on size distribution of the dust, the radii of the particles and on their density. This also increases the scatter in the final results.

We couldn't find any estimates on deposition rates in the South polar regions during the periods when there were no dust storms. Therefore we used the approach of Pollack et al. (1979) to approximate the amount of dust inside South polar slab ice.

As an initial step, let us approximate the mass of particles in the atmosphere. one can find the mass loading of particles in the atmosphere. Let  $m$  be the mass of the particles in a vertical column of unit horizontal cross section that extends from the surface to the top of the atmosphere. It depends on the optical depth  $\tau$ , mean particle radius  $\bar{r}$ , and dust particle density  $\rho$  via

$$m = \frac{2}{3} \bar{r} \rho \tau \quad (3.6)$$

Let us assume that any observed decrease of the optical depth is the result of precipitation of dust from the atmosphere to the surface and that the horizontal transport of dust by the atmosphere is negligible. Then using the observed change in  $\tau$  ( $\Delta\tau$ ) equation 3.6 straight forwardly gives the dust sedimentation rate. This approach is good in a sense that one only needs to measure the change in atmospheric opacity without caring for the time it took the dust to settle onto the surface.

We will consider below only the dust particles sedimentation. Mean particle radius and density are:  $\bar{r} = 2.5\mu m$ ,  $\rho = 3g/m^3$  - the same that was used in Pollack et al. (1979).

As we are interested in the sedimentation of dust during the time when condensation of CO<sub>2</sub> occurs and slab ice forms we should consider the optical depth change over the Southern winter time. The atmosphere over the South pole during the calm year (without global dust storm) stays quite clear and this is especially true for the Southern winter time. Atmospheric opacity stays below 0.1 over winter period and its changes are below 0.05 (Smith 2004).

Year	Method	Dust deposition rate	Equivalent layer depth, in $\mu\text{m}$ per yr	Reference
1979	Optical depth changes at 2 Viking landing sites	$2 \cdot 10^{-3} \text{ g/cm}^2/\text{yr}$ up to $20 \cdot 10^{-3} \text{ g/cm}^2/\text{yr}$	7 70	(Pollack et al. 1979)
1990	Atmospheric dust loading and the amount of $\text{CO}_2$ actually deposited	$1.8 \cdot 10^{-3} \text{ g/cm}^2/\text{yr}$	6	(Kieffer 1990)
2000	Dust accumulation on the solar panels of the Mars Pathfinder	$10 \text{ g/m}^2/\text{yr}$	3.3	(Landis 2000)
2001	Two-layer radiative transfer scattering model for estimating changes in the dust coating thickness on the radiometric calibration targets at the Pathfinder site	$20\text{-}200 \mu\text{m}/\text{yr}$	20-200	(Johnson et al. 2001)
2001	Dust storm time	$6\text{-}10 \cdot 10^{-4} \text{ g/cm}^2/\text{yr}$	2-3	(Cantor et al. 2001)
2003	Using fading rate of slope-steaks	$0.4 \text{ g/m}^2/\text{yr}$	0.1	(Schorghofer et al. 2003)
2003	Two-layer radiative transfer scattering model for estimating changes in the dust coating thickness on the radiometric calibration targets of Pathfinder	$40\text{-}90 \mu\text{m}/\text{yr}$	40-90	(Johnson et al. 2003)

Table 3.2: Estimates of dust deposition rates.

According to equation 3.6 amount of deposited dust is proportional to change in the atmospheric opacity. Fig. 3.7 a shows the thickness of the deposited layer as a function of the change in optical depth. Let us define a two dimensional simulation box with a height of 1 m and a width of 1 cm. For our simulation it is necessary to know how many dust grains reside in this box. Fig. 3.7 b. displays the number of dust particles in this box. When the opacity change is less than 0.1, less then 1000 dust grains gather in the box. We will use this number as maximum value for our simulations.

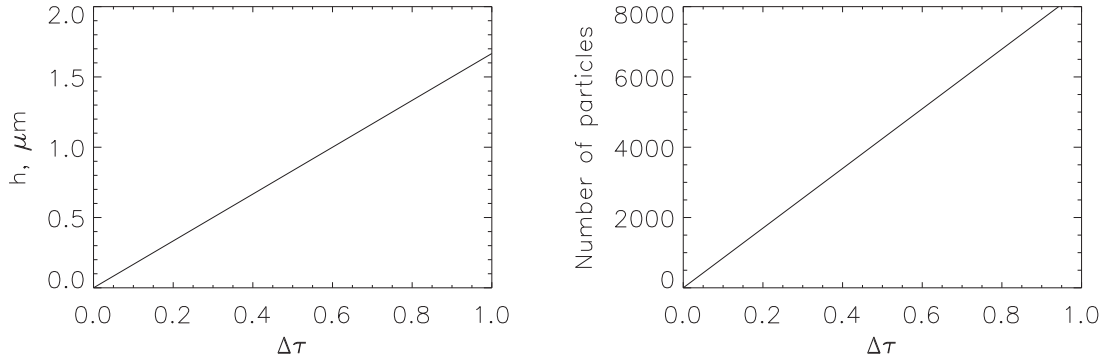


Figure 3.7: Depth of the layer of deposited dust (left hand panel) and corresponding number of dust particles in a simulation box  $1\text{m} \times 1\text{cm}$  as a function of the change in atmospheric opacity

For the more precise description of the size distribution of the dust that is deposited in the ice and on dust sedimentation rates in South polar regions the one dimensional model of Martian atmosphere developed by Inada (2002) was used. Her one dimensional model includes precipitation of dust from an atmosphere with given opacity. The main equations of this model are given below.

The initial atmospheric dust size distribution follows the modified gamma size distribution (Toon et al. 1977). The number of dust grains with a radius of  $r$  to  $r+dr$  in a unit volume is:

$$\frac{dn}{dr} = Ar^\alpha \exp\left(-\frac{\alpha}{\gamma} \left(\frac{r}{r_m}\right)\right), \quad (3.7)$$

where  $A$ ,  $\alpha$ ,  $\gamma$  are constants, and  $r_m$  is the mode radius of the distribution. The relationship between the atmospheric opacity  $\tau$  and the number density of the dust is:

$$\frac{d\tau}{dz} = \int dn \cdot \sigma(r) Q_E dr, \quad (3.8)$$

where  $z$  is the altitude,  $\sigma(r)$  is cross-section of the particle with the radius  $r$ , and  $Q_E$  is the extinction coefficient of the aerosol. The constant  $A$  is calculated by

$$A = \frac{\tau_0}{Z_{dtop} \int_0^\infty r \exp\left(-\frac{r}{r_{eff} v_{eff} \sigma(r) Q_E dr}\right)},$$

where  $\tau_0$  is the optical depth,  $Z_{dtop}$  is the top altitude of the opaque layer (in the model 20km),  $r_{eff}$  and  $v_{eff}$  are the effective radius and effective variance of the dust grains.

The effective radius, or the mean cross section weighted radius is defined as (Hansen and Travis 1974):

$$r_{eff} = \frac{\int_0^\infty r \cdot \pi r^2 n(r) dr}{\int_0^\infty \pi r^2 n(r) dr}.$$

The effective variance, or the mean cross section weighted variance is:

	value	units
$k$	$1.381 \cdot 10^{-23}$	$[J/K]$
$m_H$	$1.67 \cdot 10^{-27}$	$[kg]$
$g$	3.69	$[m/s^2]$
$\rho_a$	$1.272 \cdot 10^{-2}$	$[kg/m^3]$
$\eta$	$1.16 \cdot 10^{-5}$	$[Ps \times s]=[kg \times ms]$
$V_m$	295.94	$[m/s]$
$\rho_p$	$2.5 \cdot 10^3$	$[kg/m^3]$
$T_{surf}$	230.0	$[K]$

Table 3.3: Parameters used in the model to calculate dust sedimentation rate.

$$\nu_{eff} = \frac{\int_0^\infty (r - r_{eff})^2 \cdot \pi r^2 n(r) dr}{r_{eff}^2 \int_0^\infty \pi r^2 n(r) dr}.$$

If  $\gamma=1$  then

$$r_{eff} = \frac{3+\alpha}{\alpha} r_m, \quad \nu_{eff} = \frac{1}{3+\alpha}.$$

The effective radius and effective variance were estimated by several authors from various observations. Tomasko (1999) offers a summary on this topic. We input  $r_{eff}=1.85 \mu m$  and  $\nu_{eff}=0.25$  at  $\lambda=896.1$  nm in the model (Markiewicz et al. 1999).

Dust can move vertically by sedimentation and by turbulence. The transport is described by the flux diffusion equation:

$$\frac{\partial C}{\partial t} + \frac{\partial WC}{\partial z} - \frac{\partial \rho_a K}{\partial z} \frac{\partial C}{\partial z} / \rho_a = 0 \quad (3.9)$$

The terminal velocity of the dust is determined by the gravity of Mars and the viscosity of CO<sub>2</sub> atmosphere. Applying the Stokes law,

$$\frac{4}{3} \pi r^3 \rho_p g = 6 \pi r \eta V_{fall}, \quad (3.10)$$

where  $r$  is the particle radius,  $\rho_p$  is the particle density,  $g$  is the gravity,  $\eta$  is the dynamic viscosity of CO<sub>2</sub> and  $V_{fall}$  is the terminal velocity of the particle. With the Cunningham slip-flow correction, the terminal velocity is,

$$V_{fall} = \frac{2 \rho_p r^2}{9 \eta} (1 + \alpha K_n), \quad (3.11)$$

where

$$K_n = \frac{l}{r}, \quad l = \frac{2 \eta}{\rho_a V_a}$$

and

$$\alpha = 1.246 + 0.42 \exp\left(\frac{-0.87}{K_n}\right).$$

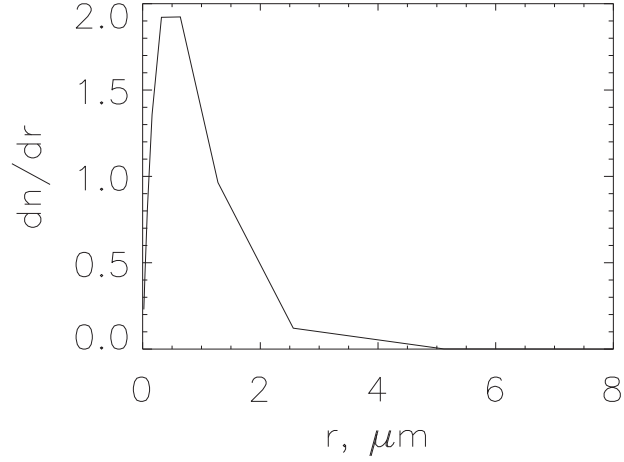


Figure 3.8: Size distribution of the dust sedimented from the atmosphere above polar regions when assuming that the dust opacity of the atmosphere is 0.1.

$K_n$  is Knudsen number,  $l$  mean free path of CO<sub>2</sub>,  $\rho_a$  is the air density,  $V_a$  is the air molecular velocity, and  $\alpha$  is the coefficient. The air molecular velocity is derived by

$$V_a = \sqrt{\frac{2kT}{M_d m_H}},$$

where  $k$  is Boltzman's constant, and  $m_H$  is the molecular weight of hydrogen. Since we need to calculate the maximum dust precipitation we set the upward air advection velocity to zero. In addition the turbulence of the atmosphere is also neglected.

All parameters of the model are summarized in the table 3.3. During the calculation the atmosphere is divided in 23 layers. The lowest layer (number 23) has the surface as the lower boundary. The model was run for 1 Martian day. All the dust that resided within the lowest layer after this time is presumed to be sedimented on the surface.

The optical depth is set to 0.1. The area is the South polar region. As an output of the calculation we get the amount of precipitated dust over 1 Martian day and the size distribution of the dust. Both of which we use later for ice cleaning modeling, which we will introduce in next section. Fig. 3.8 shows the size distribution of the sedimented dust. It is very close to atmospheric one, as it should be expected. The dust sedimentation rate is calculated to be  $1.8112044 \times 10^{-11} \mu\text{m}/\text{m}^2/\text{sec}$ . This corresponds to  $1.2518092 \times 10^{-3} \mu\text{m}/\text{m}^2/\text{yr}$  and means 1000 dust particles inside the simulation box  $1\text{m} \times 1\text{cm}$ .

### 3.2.4 Net effect

We start with a two dimensional box 1 m high and 1 cm wide filled with CO<sub>2</sub> ice in which dust particles are embedded. According to our calculations as described in chapter 3.2.3, such an amount of ice may contain about 1000 dust particles. The dust particles are characterized by coordinates  $(x_i, z_i)$  and radius  $r_i$  and follow the size distribution as discussed in chapter 3.2.3. The dust particles are either spheres (category 1) or cylinders with a height to radius ratio of 0.1. The flat surfaces of the cylinders are given angles with the horizontal plane of 10°, 30°, 60°, or 90° (categories 2-5 respectively). The dust particles are randomly distributed over these five categories.

Most of the solar radiation that is absorbed by dust in the ice is absorbed by dust in the top layer.

Dust grains in lower layers are shadowed by particles above them. They also have more ice above them than those in the upper layers, and this ice obviously also absorbs some radiation. Therefore, dust higher in the slab will sink faster than dust near the bottom. This effect will influence the time in which the CO<sub>2</sub> slab is cleaned from dust, and hence generally model time scales.

To check if a given dust particle with number  $i$  receives solar energy at a given moment, or it is shadowed by a particle above, one can use two approaches:

1. An easy but slow way is to check directly whether any particle is situated on the line that connects the Sun and particle  $i$ . The equation describing such a line is:

$$\frac{z - z_i}{Z - z_i} = \frac{x - x_i}{X - x_i}$$

where  $(X,Z)$  - are the coordinates of the Sun.

For each particle in the box (except for particle  $i$  itself) it has to be checked whether its center is closer to this line than the radius  $r_i$ . If this distance is smaller, the particle is considered to be shadowed.

To avoid the boundary effects the simulated volume is cyclically closed. This way we simulate semi-infinite medium in the x-direction.

To accelerate the algorithm, particles with z coordinates smaller than  $z_i$  are excluded from this check from the beginning. We may do so since they can not cast shadows on particles that lie above them.

2. Another way is to use a statistical approach based on the following ideas:

After the light beam gets into the host of particles, it is allowed to travel a free path length  $l$  given by:

$$l = -\bar{l} \log R(0, 1) \quad (3.12)$$

where  $\bar{l}$  is the mean free path length between two subsequent scattering events and  $R(0,1)$  is random number in the interval  $(0,1)$ .

The mean free path length  $l$ , of light in the simulating box,  $\bar{l}$  depends on the concentration  $n$  of dust that can scatter or absorb light, and can be given in terms of the total cross section:

$$\bar{l} = \frac{1}{\sum_i (n \cdot \sigma_i)} \quad (3.13)$$

For spherical particles  $\sigma_i = 2\pi r_i^2$ .

In our case  $n$  - is the concentration of dust grains above the considered particle. It can be calculated from  $N$  - the number of particles with  $z > z_i$  :

$$n = \frac{N}{(L - z_i) \cdot B \cdot r_i} \quad (3.14)$$

where  $L$  is the thickness of ice slab,  $B$  is the width of the box (1 cm in our case).

The length of the path that light has to travel to reach the particle is

$$s = \frac{L - z_i}{\sin(h)} \quad (3.15)$$

where  $h$  is the height of the Sun above the horizon.

From the comparison of  $l$  and  $s$  it is possible to determine whether the light beam hit the dust grain on its way from the top of the slab to the particle  $i$ .

If  $s$  is bigger than  $l$ , the light is free to pass through all ice between the top of the layer and particle  $i$  without meeting any obstacle, thus particle  $i$  is not shadowed.

If  $s$  is smaller than  $l$ , light gets scattered or absorbed on the way from the top of the ice to the dust grain at the coordinate  $z$ , thus particle  $i$  is considered to be shadowed.

We used both approaches to validate the model. Since they showed very similar results, we used much faster statistical approach.

If, after the check, a particle appeared not to be shadowed, the amount of energy it receives was calculated according the equations of section 3.2.2. Particles change their relative positions and should therefore be checked again for shadowing after each time step.

Example calculations of dust particle sinking are shown in Fig. 3.9. The model starts at  $L_s=150^\circ$  with a random, uniform distribution of dust inside the box (left panel of Fig. 3.9). The latitude is set to  $75^\circ$  where the Sun first rises above the horizon between  $L_s=155^\circ$  and  $L_s=160^\circ$  (see Fig. 3.2). Dust grains are then heated and sink downwards by sublimating CO<sub>2</sub> ice below them. On the middle panel, that corresponds to  $L_s=180^\circ$ , approximately half of the ice depth has been cleaned from the dust. Within 20 days (right panel) only a few particles remain inside the ice; most of the dust reached the bottom of the slab. At this time, dust grains can start to boil the ice from below; the pressure underneath the ice can rise to the point when it cracks the ice plate.

### 3.2.5 Energy flux

In the same way that dust particles inside the slab ice shadow each other, they also shadow the surface underneath the ice. This prevents ice from boiling from the bottom and building high pressures that can break the ice plate. As dust sinks down, such shadowing becomes less effective.

We can calculate total amount of energy that is withdrawn by dust still suspended inside the ice from the total amount of energy that can be received by material below the ice. We simulated what would happen to our box, filled with CO<sub>2</sub> ice and dust, at  $75^\circ\text{S}$  (at the northern edge of the cryptic region). The box has cyclically closed boundaries. To analyze the effect of ice purity we simulated several cases: with the amount of dust inside the box 1000, 800, 600, and 400 particles. These numbers of dust grains inside

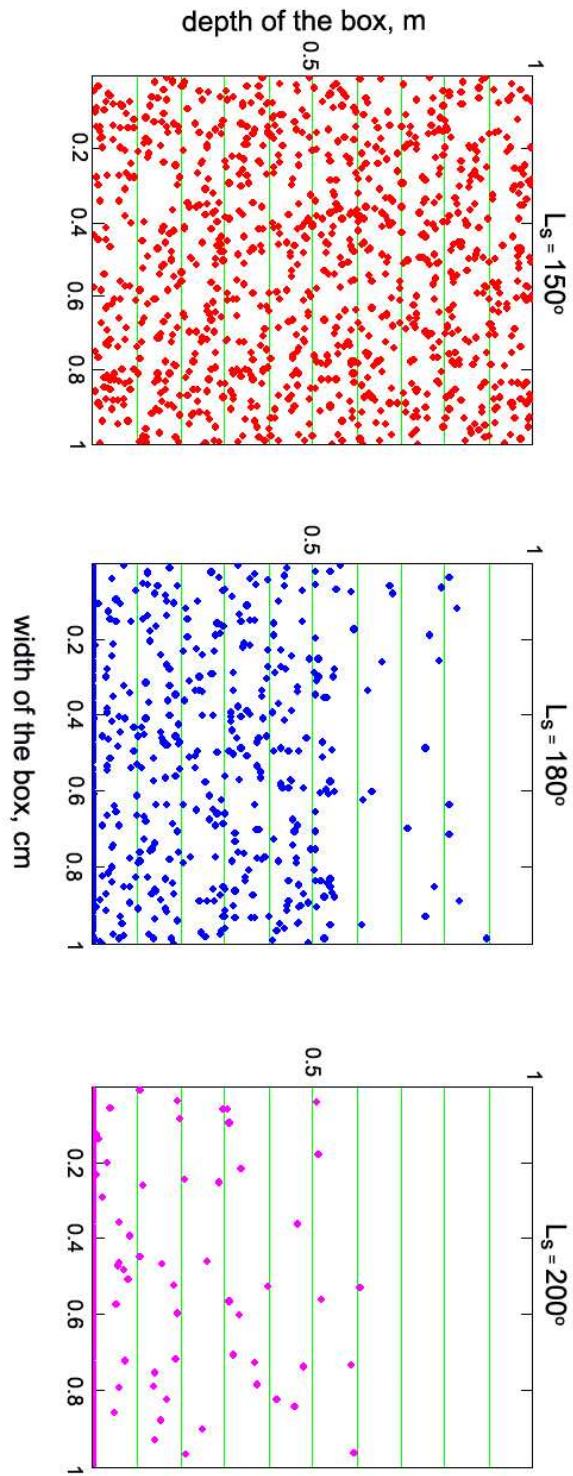


Figure 3.9: Snapshots of  $\text{CO}_2$  slab ice cleaning. The downward motion of dust grains is shown. At  $L_s=200^\circ$  slab ice is cleaned considerably.

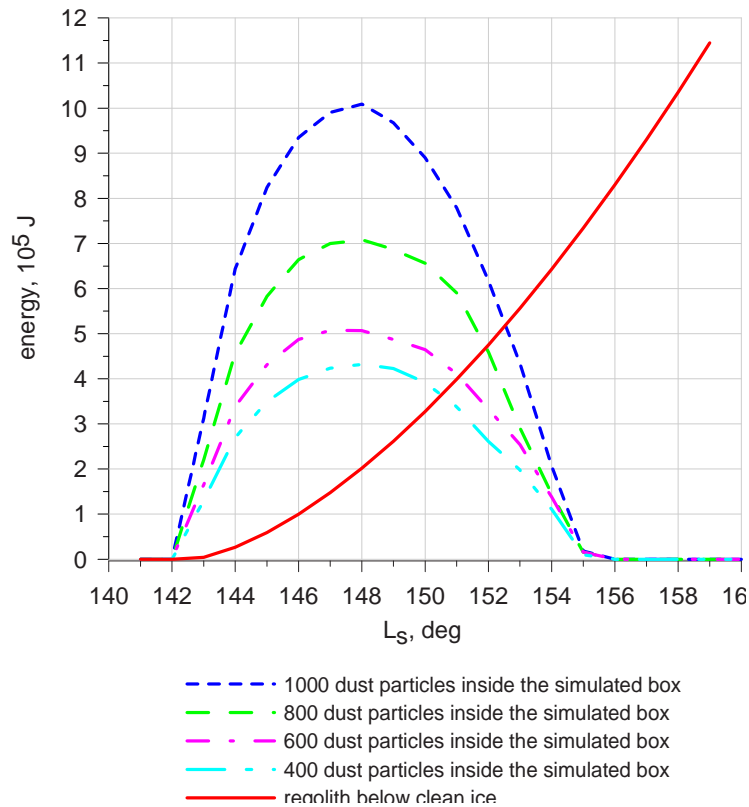


Figure 3.10: Energy removed from the total available energy flux by dust grains suspended inside the CO<sub>2</sub> ice.

the ice were chosen from the calculations described in 3.2.3 for reasonable atmospheric opacities, which can cause precipitation of these amounts of dust during the winter period. For better understanding, we can associate the number of dust grains with atmospheric opacities. The amounts of dust grains were calculated using the size distribution shown in Fig.3.8.  $\tau=0.1$  corresponds to about 1000 grains ( $N \simeq 1000$ ),  $\tau=0.06$  to  $N \simeq 800$ ,  $\tau=0.04$  to  $N \simeq 600$ , and  $\tau=0.02$  to  $N \simeq 400$ .

Fig. 3.10 shows a calculation of the total amount of energy that is removed by the suspended dust from the total available energy flux.

For example, let us consider the case with 1000 dust grain particles in the box. The total amount of energy that is removed by these is shown by the blue curve. Starting from the  $L_s=143^\circ$  the particles begin to receive Sun light and the amount of energy they capture gradually increases. At the same time, the particles sink down; those that reach the bottom of the ice slab are omitted from the calculations. This process decreases the total amount of energy that is trapped on the way down. At  $L_s=148^\circ$  the removal of dust starts to prevail over the increase of solar flux. And at  $L_s=155^\circ$  such a significant part of the dust is removed that even the increasing solar flux can not compensate anymore.

The same process happens if the number of dust particles in the box is 800, 600 or 400

(green, magenta, sky-blue curves in Fig. 3.10 respectively). The only difference shows up as maximum amount of energy that is removed.

The red curve in Fig. 3.10 is plotted for comparison. It shows the amount of energy that reaches the surface below clean ice. For this calculation we assumed that the ice plate began with a thickness of 1 m and then gets thinner with time due to ice sublimation. Thus, the absorption of light in the ice decreases with time. Therefore, the increase of energy with time (red curve, Fig. 3.10) is caused by two reasons: the increasing amount of solar hours (Fig. 3.2) and the decrease of light absorption inside the ice.

For the modeling of spider formation the important point is the intersection of the red curve with the other ones. It marks the moment when underlying material becomes warmer than the ice and may develop the pressure rise through ice sublimation. For all four curves this intersection lies between  $L_s=150^\circ$  and  $L_s=154^\circ$ . As this is still during very early spring, we conclude that shadowing of regolith by dust imbedded inside the ice may delay the formation of high pressure below the ice, but only for a few days and has no major effect on the process of spider formation.

## 3.3 Simulations of geyser-type eruptions and CO<sub>2</sub> slab ice rigidity

### 3.3.1 Calculations of stresses inside CO<sub>2</sub> ice plate

In the previous chapter we showed that CO<sub>2</sub> ice can become clean from embedded dust before the ice is fully sublimed during spring. At given moment CO<sub>2</sub> ice becomes so transparent that the surface at the bottom of the slab receives enough energy that it becomes warmer than the sublimation temperature of the ice and starts subliming ice from the bottom. Thus, CO<sub>2</sub> vapor will collect under the ice and induce rising pressure. Now we will face another question that is important for our model of spider formation: how long can the slab of ice resist the growing pressure underneath? To solve this, we have to deal with the theory of elasticity.

Mechanics of materials and theory of elasticity deal with the internal behavior of variously loaded solid bodies. The former uses assumptions based on empirical experience to approximate the behavior of the materials under the investigated conditions. The latter concerns itself largely with more mathematical analysis of the "exact" stress distribution in the loaded body. In general, however, finding solutions using the theory of elasticity is quite difficult. The main differences between these two approaches are the extent to which strains are described and the nature of simplifications that are used.

Mechanics formulae give average stresses sections. The theory of plates and shells which formulates and solves the problems from rigorous mathematical analysis, is an important application of the theory of elasticity. The study of the mechanics of materials and the theory of elasticity is based on understanding of equilibrium of bodies under the action of forces. While the statics treats the external behavior of bodies that are assumed to be ideally rigid and at rest, mechanics of materials and the theory of elasticity are concerned with the relationships between external forces and internal forces and deformations induced in the body.

Mechanics of materials and theory of elasticity methods are used to determine strength, stiffness and stability of various loaded members. The complete analysis of a load-carrying member by the so-called method of equilibrium involves three basic principles:

1. **Statics.** The equilibrium conditions of forces must be satisfied.
2. **Deformations.** Stress-strain or force deformation relations (e.g. Hook's law) must apply to the behaviour of material.
3. **Geometry.** The conditions of geometric fit or compatibility of deformations, must be satisfied.

The solutions based on this procedure must satisfy some specified boundary conditions.

For the spider formation model we will consider an ice plate under the load of gas pressure from below. We will assume the plate to be circular with simply supported edges. The pressure is uniformly distributed over the circular area in the plate's center. Fig.3.11 illustrates this case. The plate is initially flat with thicknesses that is much smaller than the other dimensions. The dimensions of our ice plate are chosen on the basis of measurements of spiders and thicknesses of ice sheets. The latter depend on time during spring season, and should therefore be calculated separately. The diameter of the plate is chosen to be mean spiders' diameter which is 300 m. We will now look at the problem of bending

of such a circular plate of constant thickness subject to symmetrical loading and boundary conditions appropriate for simply supported edges.

The derivation of governing equations for such a system in cartesian coordinates can be found in (Ansel C. Ugural 1999). The governing differential equation for deflection  $w$  of thin plates was first derived by Lagrange in 1811. It has a form:

$$\frac{\partial^4 w}{\partial x^4} + 2 \frac{\partial^4 w}{\partial x^2 \partial y^2} + \frac{\partial^4 w}{\partial y^4} = \frac{p}{D}, \quad (3.16)$$

where

$$D = \frac{Et^3}{12(1 - \nu^2)}$$

is flexural rigidity of the plate of thickness  $t$  and  $p$  is the lateral load acting on the plate, and  $\nu$  is the Poisson's ratio

$$\nu = \frac{\text{lateral strain}}{\text{axial strain}},$$

$E$  is called the modulus of elasticity or Young's modulus, it is the characteristic of material. Modulus of elasticity relates stress  $\sigma$  to strain  $\varepsilon$  in Hooke's law:

$$\sigma = E\varepsilon$$

Normal strain is defined through the displacement of unit element  $u$  along x-axis:

$$\varepsilon_x = \lim_{\Delta x \rightarrow 0} \frac{\Delta u}{\Delta x} = \frac{du}{dx}$$

Formulas for bending and twisting moments in terms of the deflection are:

$$\begin{aligned} M_x &= -D \left( \frac{\partial^2 w}{\partial x^2} + \frac{\partial^2 w}{\partial y^2} \right) \\ M_y &= -D \left( \frac{\partial^2 w}{\partial y^2} + \frac{\partial^2 w}{\partial x^2} \right) \\ M_{xy} &= -D(1 - \nu) \frac{\partial^2 w}{\partial x \partial y} \end{aligned} \quad (3.17)$$

The vertical shear forces are related to  $w$ , upon derivation of the equilibrium equations:

$$\begin{aligned} Q_x &= -D \frac{\partial}{\partial x} \left( \frac{\partial^2 w}{\partial x^2} + \frac{\partial^2 w}{\partial y^2} \right) \\ Q_y &= -D \frac{\partial}{\partial y} \left( \frac{\partial^2 w}{\partial x^2} + \frac{\partial^2 w}{\partial y^2} \right) \end{aligned} \quad (3.18)$$

To determine  $w$ , it is required to integrate equation 3.16 with the constants of integration dependent upon the appropriate conditions.

If edges of plate are considered to be simply supported, the deflection and bending moments are both zero. Hence

$$w = 0 \quad M_x = -D \left( \frac{\partial^2 w}{\partial x^2} + \nu \frac{\partial^2 w}{\partial y^2} \right) \quad (x = a) \quad (3.19)$$

The first of these equations implies that along the edge  $x = a$ ,  $\partial w / \partial y = 0$ ,  $\partial^2 w / \partial x^2 = 0$ . Therefore, conditions expressed by 3.19 may be written in the following equivalent form

$$w = 0 \quad \frac{\partial^2 w}{\partial x^2} = 0 \quad (x = a) \quad (3.20)$$

Determination of the fundamental equations of a laterally loaded circular plate is easier in polar coordinates: radial  $r$ , angular  $\theta$ :

$$\begin{aligned} x &= r \cos \theta & r^2 &= x^2 + y^2 \\ y &= r \sin \theta & \theta &= \tan^{-1} \frac{y}{x} \end{aligned} \quad (3.21)$$

The governing differential equation for plate deflection in polar coordinates is derived:

$$\nabla^4 w = \left( \frac{\partial^2}{\partial r^2} + \frac{1}{r} \frac{\partial}{\partial r} + \frac{1}{r^2} \frac{\partial^2}{\partial \theta^2} \right) \left( \frac{\partial^2 w}{\partial r^2} + \frac{1}{r} \frac{\partial w}{\partial r} + \frac{1}{r^2} \frac{\partial^2 w}{\partial \theta^2} \right) = \frac{p}{D} \quad (3.22)$$

The radial, tangential and twisting moments  $M_r$ ,  $M_\theta$ ,  $M_{r\theta}$  and the vertical shear forces  $Q_r$ ,  $Q_\theta$  expressed through the vertical deflection of the plate  $w$  in polar coordinates are:

$$\begin{aligned} M_r &= -D \left[ \frac{\partial^2 w}{\partial r^2} + \nu \left( \frac{1}{r} \frac{\partial w}{\partial r} + \frac{1}{r^2} \frac{\partial^2 w}{\partial \theta^2} \right) \right] \\ M_\theta &= -D \left[ \frac{1}{r} \frac{\partial w}{\partial r} + \frac{1}{r^2} \frac{\partial^2 w}{\partial \theta^2} + \nu \frac{\partial^2 w}{\partial r^2} \right] \\ M_{r\theta} &= -(1 - \nu) D \left( \frac{1}{r} \frac{\partial^2 w}{\partial r \partial \theta} - \frac{1}{r^2} \frac{\partial w}{\partial \theta} \right) \end{aligned} \quad (3.23)$$

$$\begin{aligned} Q_r &= -D \frac{\partial}{\partial r} (\nabla^2 w) \\ Q_\theta &= -D \frac{1}{r} \frac{\partial}{\partial \theta} (\nabla^2 w) \end{aligned} \quad (3.24)$$

Formulas for the plane stress components are written in the following form

$$\sigma_r = \frac{12M_r z}{t^3}, \quad \sigma_\theta = \frac{12M_\theta z}{t^3}, \quad \sigma_{r\theta} = \frac{12M_{r\theta} z}{t^3} \quad (3.25)$$

where  $M_r$ ,  $M_\theta$ ,  $M_{r\theta}$  are defined from equations 3.23. The maximum stresses take place on the surfaces of the plate (at  $z = \pm t/2$ ).

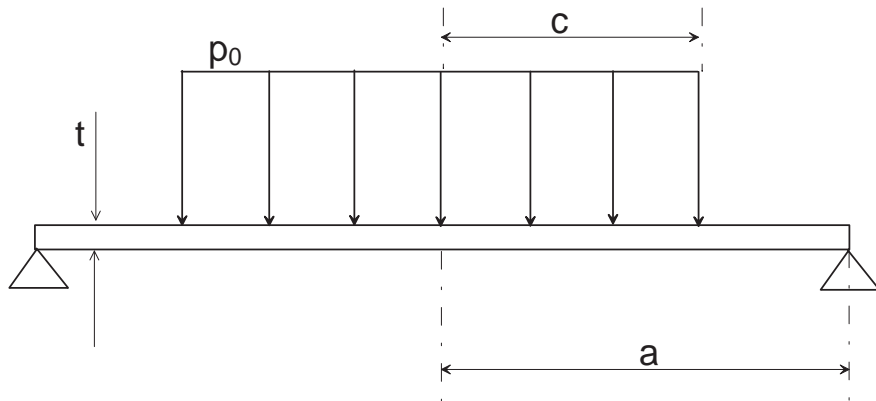


Figure 3.11: Circular plate of radius  $a$  with simply supported edges under a uniform load on circular area of radius  $c$

We will consider only load that is independent of the angle  $\theta$  or, by other words, we will restrict ourselves to axisymmetric bending of the plate. For this case, only  $M_r$ ,  $M_\theta$ , and  $Q_r$  act on the circular plate element. The moments and shear forces are:

$$\begin{aligned} M_r &= -D \left( \frac{d^2 w}{dr^2} + \frac{\nu}{r} \frac{dw}{dr} \right) \\ M_\theta &= -D \left( \frac{1}{r} \frac{dw}{dr} + \nu \frac{d^2 w}{dr^2} \right) \\ Q_r &= -D \frac{d}{dr} \left( \frac{d^2 w}{dr^2} + \frac{1}{r} \frac{dw}{dr} \right) \end{aligned} \quad (3.26)$$

The differential equation now reduces to:

$$\nabla^4 w = \left( \frac{\partial^2}{\partial r^2} + \frac{1}{r} \frac{\partial}{\partial r} \right) \left( \frac{\partial^2 w}{\partial r^2} + \frac{1}{r} \frac{\partial w}{\partial r} \right) = \frac{p}{D} \quad (3.27)$$

If the plate is under uniform loading  $p = p_0$ , the general solution of Eq.3.27 is

$$w = c_1 \ln r + c_2 r^2 \ln r + c_3 r^2 + c_4 + \frac{p_0 r^4}{64D} \quad (3.28)$$

where  $c$ 's are constants of integration.

Consider the case of a circular plate of radius  $a$  with simply supported edges under a load  $p_0$  uniformly distributed on circular area of radius  $c$  (Fig.3.11) we can integrate Eq.3.27 and find and deflection  $w$  at the center of the plate

$$w = \frac{3(1-\nu)p_0 c^2}{16Et^3} \left[ 4(3+\nu)a^2 - (7+3\nu)c^2 - 4(1+\nu)c^2 \ln \frac{a}{c} \right], \quad (3.29)$$

and maximum bending stress  $\sigma$  at the center of the plate

$$\sigma = \frac{3p_0 c^2}{8t^2} \left[ 4 - (1-\nu) \frac{c^2}{a^2} + 4(1+\nu) \ln \frac{a}{c} \right]. \quad (3.30)$$

If one knows the load to which plate is exposed then stress, calculated with the equation 3.30, can be compared to so called yield stress - the maximum stress that does not cause the failure. Yield stress, as well as modulus of elasticity, is the characteristic of each particular material. If the calculated stress is bigger than yield stress it means that the plate will not sustain the load, it will cause failure of the plate. For the model of spiders' formation it means eruptions of gas from underneath the ice plate, i.e. appearance of geyser structures.

### 3.3.2 Pressure below ice plate

To use equations 3.29 and 3.30 one needs to know the load on the plate. In our case the load is caused by pressure of  $\text{CO}_2$  subliming underneath the ice plate. For the first approximation we consider the  $\text{CO}_2$  gas to follow the ideal gas law, Then the pressure can be written as:

$$P = \frac{\rho_{gas} RT}{\mu_{\text{CO}_2}}, \quad (3.31)$$

where  $R$  is the gas constant,  $T$  - instantaneous temperature of the CO<sub>2</sub> gas,  $\mu_{CO_2}$  - molecular weight of the CO<sub>2</sub>, and  $\rho_{gas}$  is the instantaneous density of gas which can be calculated for each following time step from the conditions on preceding one:

$$\rho_{gas}(t + dt) = \frac{\rho_{gas}V(t) + \rho_{ice} \frac{\partial V}{\partial t} dt}{V(t) + \frac{\partial V}{\partial t} dt}.$$

Then the pressure is calculated as:

$$P(t + dt) = \frac{\rho_{gas}(t)RT}{\mu_{CO_2}} + \frac{\rho_{ice}RT}{V(t)} \frac{\partial V}{\partial t} dt, \quad (3.32)$$

for two dimensional case

$$\frac{\partial V}{\partial t} = \frac{\partial z}{\partial t}.$$

and

$$\frac{\partial z}{\partial t} = -\frac{E}{\rho_{ice}H_{CO_2}},$$

where  $H_{CO_2}$  - latent heat of CO<sub>2</sub> sublimation, and  $E$  is absorbed energy per unit area calculated from 3.1. Now the pressure is:

$$P(t + dt) = P(t) + \frac{RT}{dz(t)} \frac{E(t + dt)}{H_{CO_2}} dt. \quad (3.33)$$

Using this formula together with 3.30 it is possible to calculate stresses that are produced in the ice plate by growing pressure underneath. The results of such calculations are shown in Fig. 3.12. Red curve shows the dependance for the latitude of 75°S and magenta curve for the latitude of 85°S. There is a steep increase of stress at the moment when sun rises and the energy can pass through the dust in the top layer of ice. For the latitude of 75°S this happens at roughly  $L_s = 152^\circ$ . Then the pressure grows with increase of solar energy due to the rising sun. The same happens at the latitude of 85°S with the difference that the stress starts to grow later - around  $L_s = 176^\circ$ .

### 3.3.3 Discussion of material strength

A significant area of uncertainty is related to mechanical properties of CO<sub>2</sub> slab ice. To evaluate the model of spiders' formation we need to know the moment when ice plate breaks because it can not resist anymore the growing pressure. For this we need to know mechanical characteristics of material under the stress, namely: yield stress, Young's modulus and Poisson's ratio for CO<sub>2</sub> slab ice. Unfortunately, as it does not belong to usual engineering materials, the laboratory measurements of listed constants are absent. In this work we used Young's modulus and Poisson's ratio measured for water slab ice. Another difficulty is yield stress which has to be compared to the stress calculated above. From the coring experiments (Garry and Wright 2004) it is known that for coring of CO<sub>2</sub> slab ice one needs more power than for coring of H<sub>2</sub>O ice. It presumes that CO<sub>2</sub> ice is stronger than water ice, but even so it can still be more fragile for fracturing. Since we

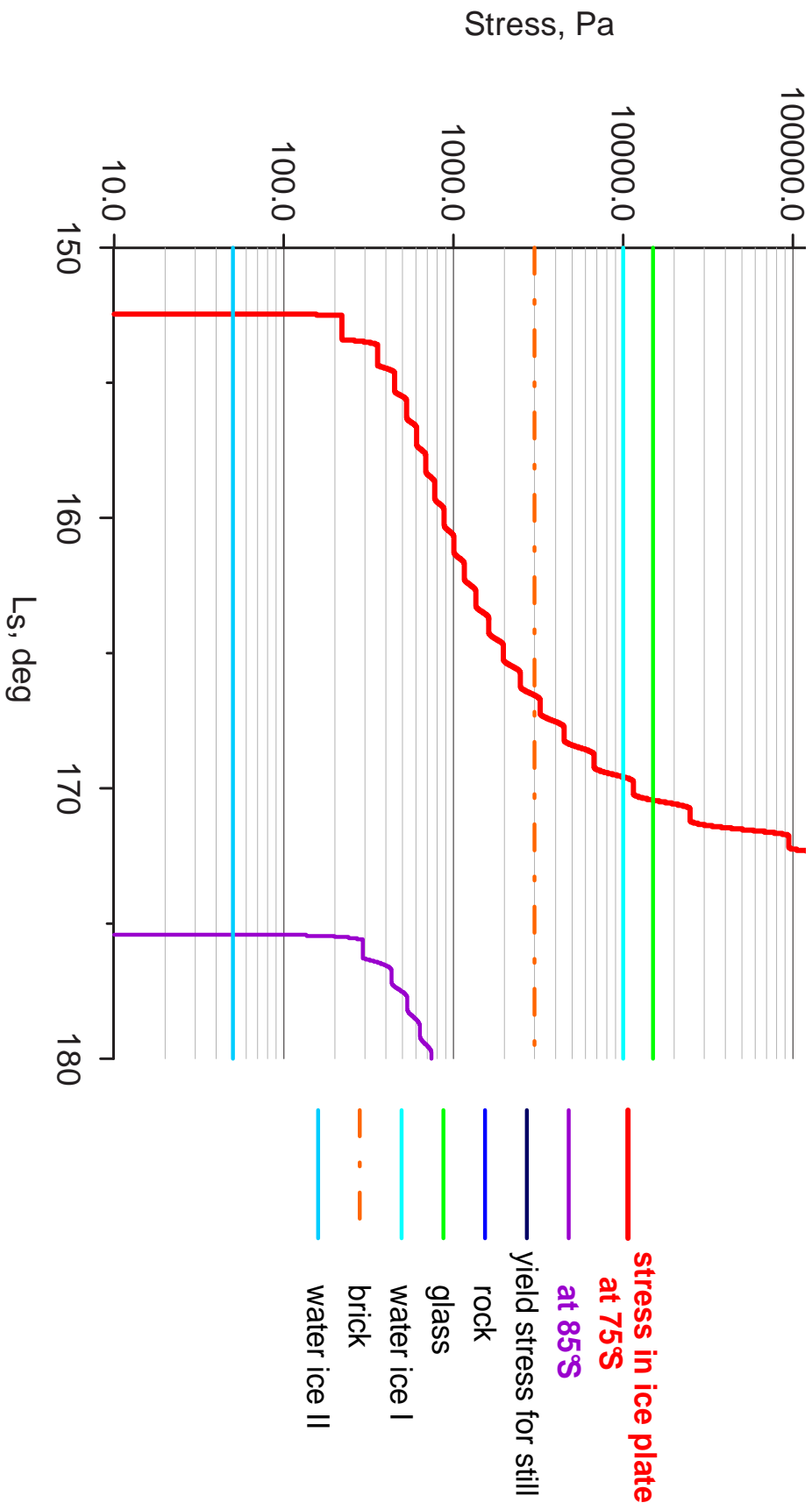


Figure 3.12: Comparison of stresses inside ice plate that are produced by growing pressure below it to the yield stresses of different materials.

have no experimental data for CO<sub>2</sub> ice, we compared stresses produced in our CO<sub>2</sub> ice plate to yield stresses of different materials Fig. (3.12). Our set includes two types of water ice: clean ice - yield stress  $\sigma_y = 10^5$  Pa; and ice with inclusions that make ice more fragile -  $\sigma_y = 50$  Pa, brick  $\sigma_y = 3 \cdot 10^3$ Pa, glass  $\sigma_y = 1.5 \cdot 10^4$ Pa, rock  $\sigma_y = 2 \cdot 10^5$ Pa and steel  $\sigma_y = 4 \cdot 10^5$ Pa.

We assume that CO<sub>2</sub> slab ice yield stress should lie inside the limits of weakest and strongest of these materials. It should be at least weaker than steel, but stronger than water ice. With this assumption we can conclude that at latitude 75°S pressure will grow enough to break the ice plate in order of minimum 1 day to maximum 20 days. The fracture of plate should happen before  $L_s = 175^\circ$ . At more southern latitudes this process can only start at this time.

### 3.4 Conclusions

We checked two stages of Kieffer's model of spider formation: cleaning of CO<sub>2</sub> slab ice from dust and breaking the slab ice plate under the pressure built below it. Concerning the cleaning of ice from dust our conclusions are:

- sinking rates of dust grain depend highly on grain shape and orientation;
- spherical grain can reach the bottom of a 1 m thick layer of ice in a relatively short time of about 20 days, if the ice is located at a latitude of 75°S;
- particles closer to pole start to sink somewhat later in the season, but due to the steeper increase in incoming solar radiation, these reach the bottom of the slab even faster than those on more northern latitudes;
- downward velocities of ice sublimation and dust sinking are comparable;
- during the beginning of spring the dust sinking rate is faster than the ice sublimation rate. Spherical dust grains can sink so fast that the CO<sub>2</sub> ice becomes completely clean of dust. If the dust particles are irregularly shaped, then only the upper part of ice will be cleaned;
- for an atmospheric optical depth of 0.1 we calculated a dust sedimentation rate in the South polar region of  $1.2518092 \times 10^{-3} \mu\text{m}/\text{m}^2/\text{yr}$ ;
- shadowing of grains by other grains doesn't have a significant impact on the time needed to clean a slab;
- shadowing of regolith below the slab by dust imbedded in the ice may delay the formation of high pressure below the ice, but only for a few days and it has no major effect on the process of spider formation;
- at a latitude of 75°S it will take between 1 and 20 days to build enough pressure below a slab to break it. The fracture of plate should happen before  $L_s = 175^\circ$ .

For the effects considered so far, the model of spiders formation proposed by Kieffer is feasible.



# 4 Seasonal evolution of the Martian cryptic region: influence of the atmospheric opacity

## 4.1 Introduction

Observations of the Martian South polar regions with the Mars Orbiter Camera (MOC) onboard Mars Global Surveyor (MGS) show diverse morphological features, such as swiss cheese, spiders, dalmatian spots, oriented fans and others (Kieffer 2003). All these structures result from interplay between solid CO<sub>2</sub>, water ice and martian dust. Condensation and sublimation of ices, which are governed by changes of insolation during the Martian seasonal cycle, produces these unusual forms that are never observed on Earth. Mainly to monitor the evolution of such intriguing features, MOC repeatedly observes the same areas. One region which contains spiders, and was observed several times by MOC, drew our attention since its albedo changed dramatically from one year to the next.

These two images, E09-00028 and R08-01730 (Fig. 4.1), were taken in years 2001 and 2003 respectively with MOC's NA camera. The region covered is around 82.5°S, 41°E. The area is outside of the permanent South polar cap, but during winter time it is covered by seasonal CO<sub>2</sub> and H<sub>2</sub>O ices. Images lie inside the cryptic region and partially cover the area showing spider patterns. Both images show the same morphological features, however differ significantly in surface albedo, the image from 2001 has a lower albedo than the one from 2003.

The observed inter-annual variability may be related to the global dust storm that happened in 2001 and finished around  $L_s=230^\circ$ , i.e. just before image E09-00028 was taken. The 2001 dust storm engulfed Mars completely for about 50 sols around the beginning of southern spring. Southern spring began with a "bang" in late June 2001 ( $L_s=180^\circ$ ) with a series of large dust storms that in some regions were still occurring each day, well into September ( $L_s=220^\circ$ ).

Spring in the polar region is a time of fast sublimation of seasonal surfaces ices. Atmospheric opacity plays a significant role in this process. When a dust storm occurs, the increase of atmospheric optical depth has 3 major effects:

1. Solar flux onto the surface is decreased;
2. Heating of the atmosphere is increased;
3. Surface albedo is altered by the settling dust - in polar regions this lowers the albedo below that of pure ice.

Here we model the seasonal ice sublimation/condensation cycle to show that the evo-

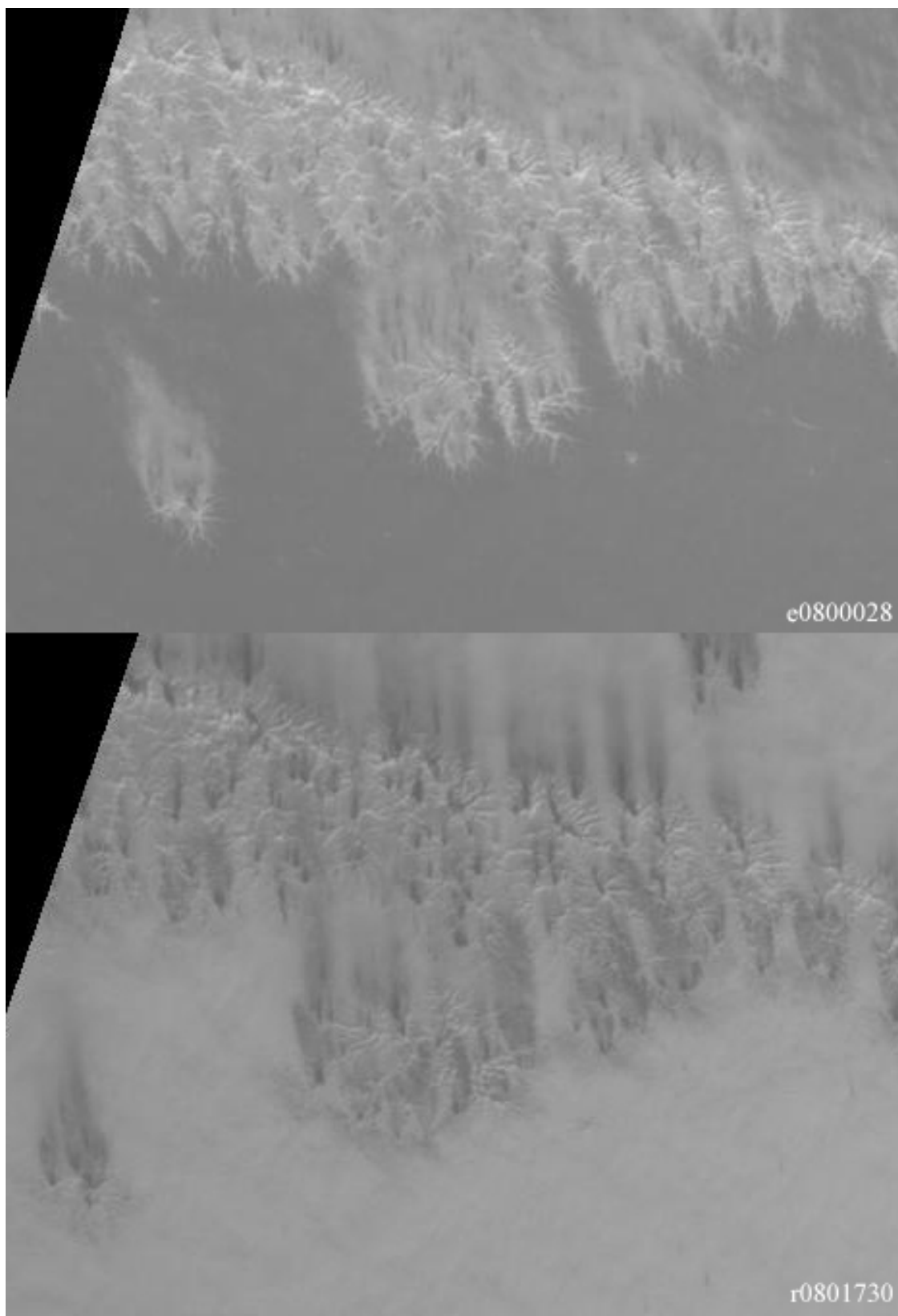


Figure 4.1: The subsections of MOC NA images e0800028 and r0801730 of the same area showing year to year change of the surface albedo.

lution of this particular area of the cryptic region was affected by the dust storm during year 2001. The storm lowered surface temperatures, and thus caused later than usual seasonal sublimation of both CO<sub>2</sub> and water ices. It also decreased surface albedo.

## 4.2 Observations

### Images of the area

Image E09-00028 targeted the area around 82.5°S, 41°E at  $L_s=244.05^\circ$  in 2001. Image R08-01730 is another observation of the same area at  $L_s=244.31^\circ$  in 2003 - one Martian year later. More details of observation parameters for both images are listed in the Table 4.1. Both of these MOC narrow angle images are shown in Fig. 4.6, together with the plot of the surface albedo and TES measured temperatures.

One can see that areas in the beginning of the images and at the end significantly differ in surface albedo while rough surface in the middle of the images stays the same. Fig. 4.1 shows a closer view of the left sections of both images. Spiders features can be clearly seen in both images. Their shapes appear very similar while the features that look like fan-shaped deposits have changed appearance (but indeed, not orientation). The main conclusion is again that surface albedos differ significantly between the two images.

### Early south spring images with and without dust storm

By early July 2001, the martian atmosphere was so hazy that opportunities for high resolution imaging of the planet were very limited. Fig. 4.2 illustrates the difference of the atmospheric conditions in 2001 and 2003. Both images, E08-00262 and R07-01697 were taken at  $L_s=227^\circ$ . Earlier imaging of South pole regions is difficult because of low angle of insolation. The left panel of Fig. 4.2 is the wide angle camera image E08-00262 taken on September 4, 2001. It shows only few surface features, mainly the brightest regions that are visible on the South polar cap, and it makes clear that the atmosphere is very opaque with a large amount of dust suspended in it. Although the atmosphere over the

	E09-0028	R08-01730
Longitude of the image center	319.19°W	319.17°W
Latitude of the image center	82.53°S	82.55°S
Solar longitude ( $L_s$ )	244.05°	244.31°
Scaled pixel width	4.35 <i>m</i>	4.35 <i>m</i>
Local true solar time	15.78 decimal hours	15.86 decimal hours
Emission angle	18.00°	17.99°
Incident angle	63.56°	63.66°
Phase angle	49.87°	52.28°
North azimuth	112.95°	112.00°
Sun azimuth	53.21°	51.01°
Spacecraft altitude	375.45 <i>km</i>	372.94 <i>km</i>

Table 4.1: Observational parameters for MOC images E09-00028 and R08-01730.



Figure 4.2: MOC WA camera images E08-00262 (left) and R07-01697 (right), both taken at  $L_s = 227^\circ$  the first during 2001, the second in 2003.

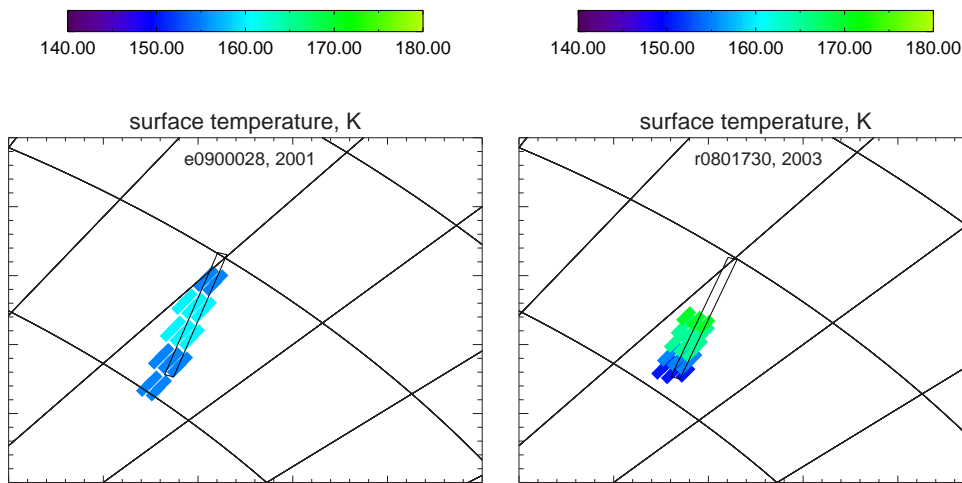


Figure 4.3: Surface temperatures measured by TES for time and location of images e09-00028 and r08-01730.

South Pole is usually very clean, even polar area features are hardly visible in this image. Thus the 2001 dust storm penetrated to the south polar region. In comparison, image R07-01697 taken on July 24, 2003, shows a cleaner atmosphere. Below we will discuss modeling results for particular area shown in Fig. 4.1 for years with different atmospheric opacities. However, first we should check whether we really can interpret the observed effect as the result of a global dust storm.

There are at least two other possible explanations of the observed inter-annual change in the surface albedo. First, the difference could be explained if the observations were made with different insolation and observing geometries. This would be especially important since the Martian surface is hardly Lambertian. Differences in incident or emission angles between the two images should change the amount of light reflected towards the camera, but Table 1 shows the observation was repeated under the same conditions with high accuracy. Differences in incident, emission, phase and other observational angles are below  $3^\circ$ . Therefore, we will neglect effects of insolation and observational geometry in the following discussion. Another explanation could be that the weather differed significantly between these two years, so that in one year there was more ice present than in the other. The consequence would be a different surface albedo. A low albedo indicates absence of ice and such surface should have higher temperature. Surface with higher albedo should have ice cover and low temperature.

### TES temperatures

The Thermal Emission Spectrometer (TES) offers the possibility to check the last assumption above. An estimate of the observed surface temperature is obtained from TES infrared spectra in the band  $1285\text{-}1315\text{ cm}^{-1}$ . This window was used by the TES team for the estimate of surface temperatures (Smith 2004). TES derived surface temperature for the same orbits when MOC took images E09-00028 and R08-01730 are shown in Fig. 4.3 together with MOC NA images footprints. As one can see the surface temperature during the 2001 are between 155K and 165K; i.e. at least 7K above sublimation temperature of

CO<sub>2</sub> ice. This in turn implies that surface is not covered with CO<sub>2</sub> ice or at most only locally in shadowed areas. Temperatures in 2003 are more scattered: from 150K to 175K. But the main area of the 2003 MOC image has generally 5-10K higher temperatures than in 2001. This is hard to explain considering the high surface albedo in 2003 and the lower one in 2001. Moreover, it proves our assumption about albedo differences only as a result of the presence or absence of CO<sub>2</sub> ice is incorrect. In addition, we can see that the middle of imaged area is warmer than its edges in both years.

### **Wind direction and fans**

Both images in Fig. 4.1 show fan structures superimposed on the spiders. They are all oriented in the same direction but their fine structures differ between two years. This may imply that spiders are active features and that the fans were reproduced each year. From the statistical study of spider images taken by MOC we concluded that fan structures near spiders appear only during beginning of the southern spring, i.e., before  $L_s=280^\circ$ . Fig. 2.13 shows the seasonal distribution of spiders with and without fans. We used 326 images of spiders to compile these data. Fans associated with spiders were never found after  $L_s=280^\circ$  which coincides with the time when CO<sub>2</sub> ice has completely sublimed away. During both years the fans were oriented in the same direction. Probably the winds that determine this, blew in the same direction during the spring of both years. We compared the direction of the fans with winds simulated in the Martian Climate Database for the southern spring (Fig. 2.14). One can see that direction of the preferential wind of the area in spring coincides with the orientation of the fans.

### **Surface roughness from MOLA**

The resolution of MOLA data does not allow to resolve such fine structure as seen in MOC images. Several tracks exist for the considered area but all of them fall not exactly in the area of images E09-00028 and R08-01730. Three of such tracks are shown in the Fig. 4.5. MOC image r08-01731 lies to the side of all of them. All three MOLA tracks indicate quite steep North-facing slope between  $-83^\circ$  and  $-82.3^\circ$ . Latitudinal extend of MOC images is indicated with red bar and covers the slope.

We used MOLA data for similar spider pattern regions to infer the approximate roughness of the surface. Fig. 4.4 shows an example of such a region. The fine structure is not resolved well, but the scattering of MOLA measurements imply altitude variations of about 20 m within the measured footprints.

### **Overview of observational data for the area**

- MOC images e09-00028 and r08-01730 show a significant difference in surface albedo (Fig.4.6, middle panel).
- Middle part of both images shows no albedo difference and looks pretty much the same as rough areas of other images with spiders, for example, Fig. 4.4.
- General inclination of the surface is close to  $3^\circ$ . TES temperatures show a slight difference between the images: e09-00028 is generally colder than r08-01730, but the difference is more pronounced in the middle of the images, where the surface seems rough and show no albedo difference.

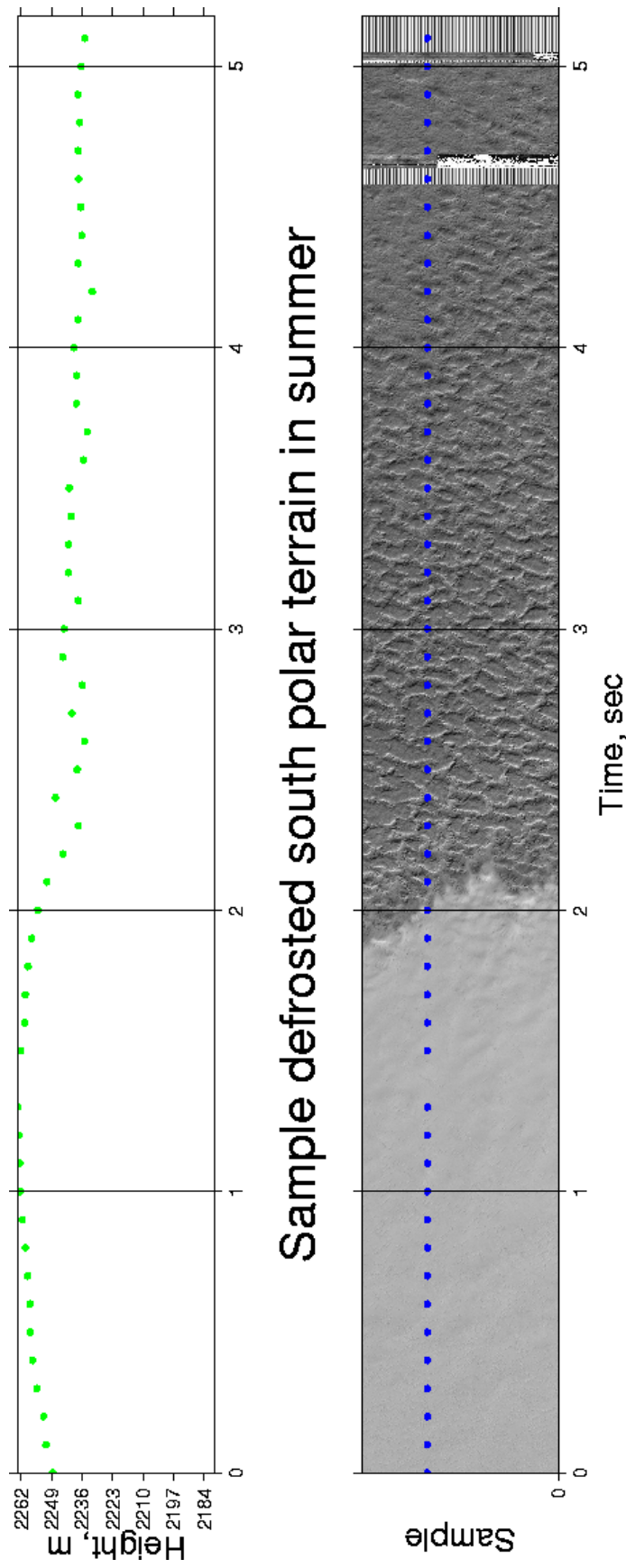


Figure 4.4: MOLA data for the spider pattern area. Left side of MOC image show rough area with pits and depressions. Variations in altitudes is about 20 m.

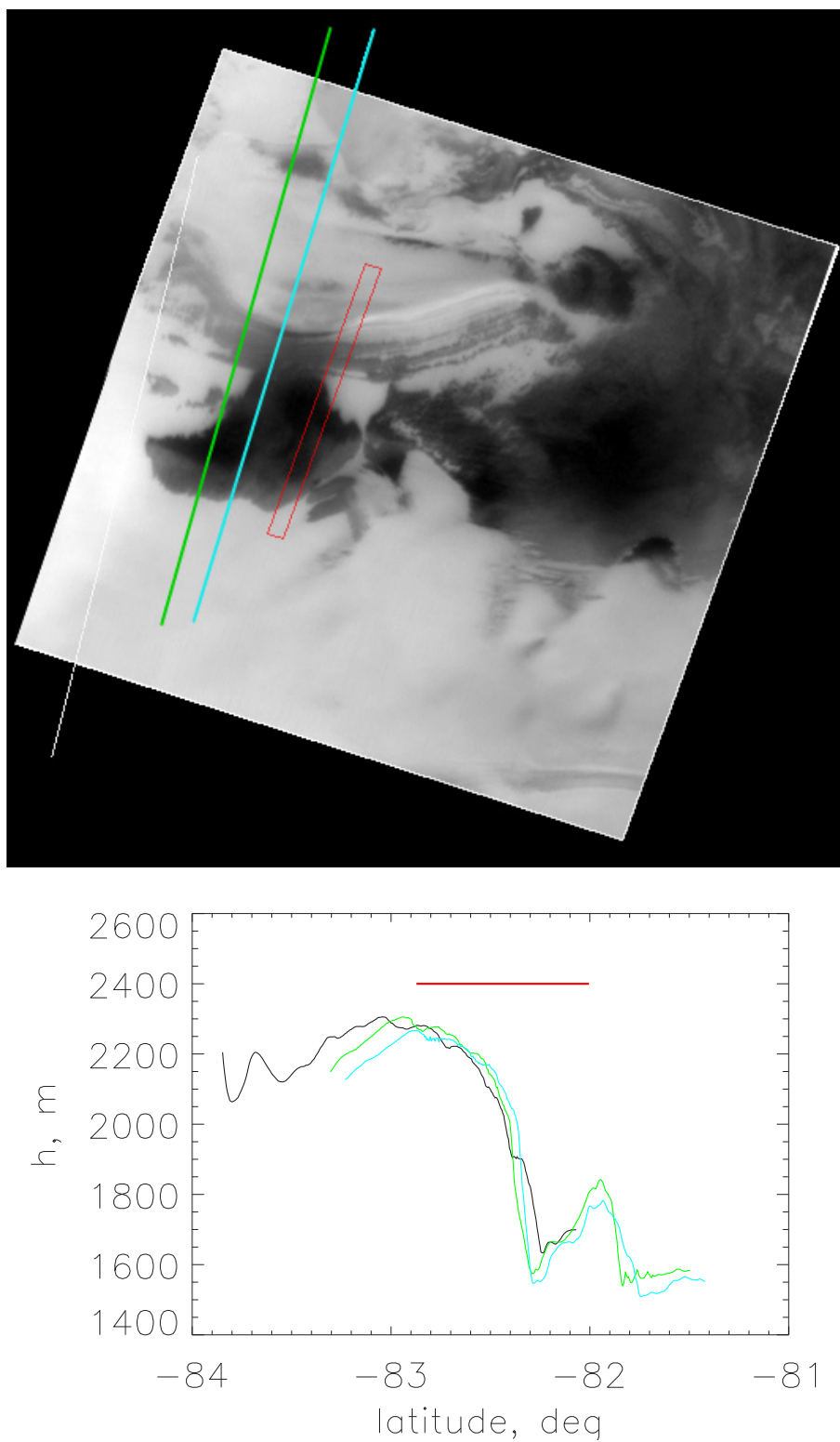


Figure 4.5: Topography of area of interest. Upper panel shows MOC WA image, i.e. contest image for NA image r08-01731. The red rectangle is the footprint of MOC NA image r08-01731; blue, green, and white lines - footprints of MOLA measurements, they are shown in lower panel plot. Red line indicates latitudinal extend of MOC footprint.

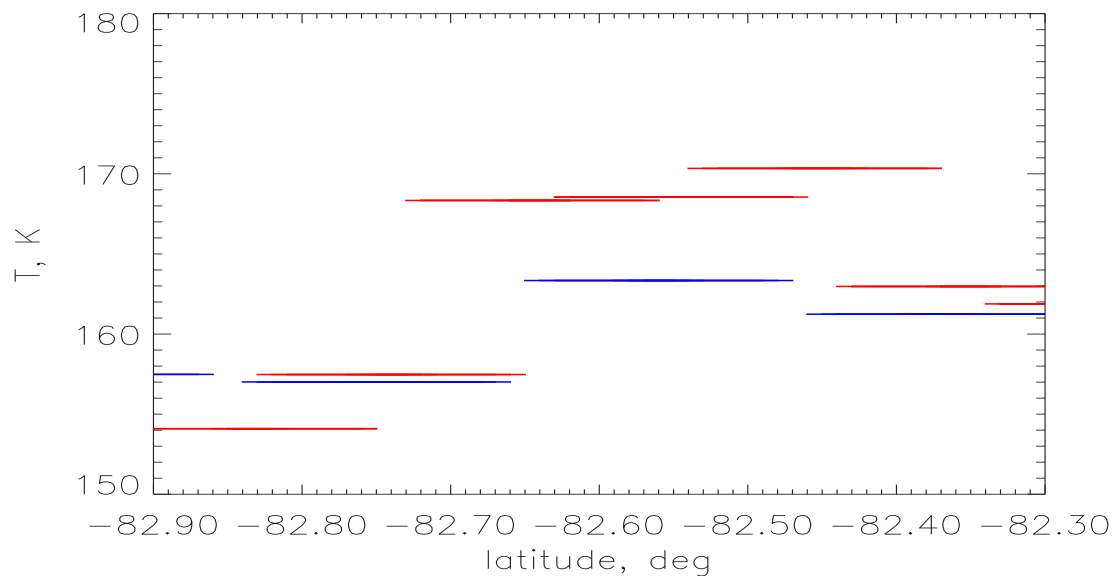
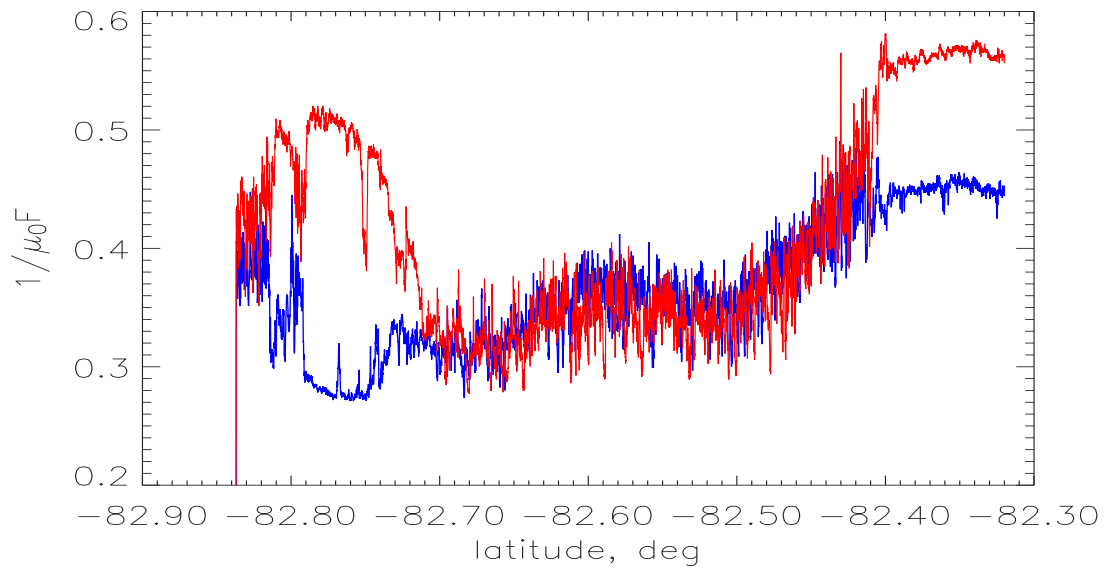
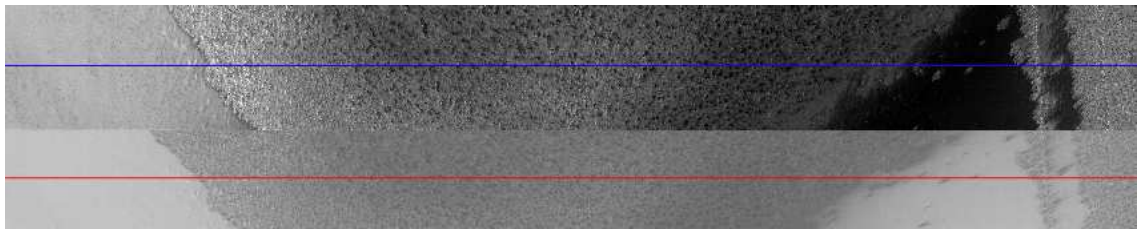


Figure 4.6: The upper panel shows sections of MOC images e09-00028 and r08-01730. The middle panel shows the  $I/\mu_0 F$  plots through these images. Blue curve corresponds to the line in the middle of upper image, red one - to the same place in the image below. The lower panel is the TES temperatures plotted in the same frame.

We will try to explain these observational data with modeling in the following section.

## 4.3 Model description and results

### 4.3.1 Model description

The model used for the present work has been described by Kossacki and Markiewicz (2002), Kossacki et al. (2003), and Kossacki and Markiewicz (2004). Full description of the model is beyond the scope of the present work. Interested reader is referred to the papers cited above. The model includes self-consistent treatment of the sublimation and condensation of CO<sub>2</sub> and H<sub>2</sub>O ices. In the current version we consider a smooth, horizontal surface without any troughs and added warming of the surface by the IR emission from the atmosphere.

### 4.3.2 Model results

The main aim of this work is to understand the thermal behaviour and visual appearance of the area shown in the two images in Fig. 4.1. The model was used to calculate surface temperatures and thicknesses of CO<sub>2</sub> and H<sub>2</sub>O ice layers for the corresponding conditions of these two years. The coordinates of the modelled area correspond to the MOC NA image center: 82.5°S and 41°E.

The seasonal sublimation of ices from the Martian surface is affected by various parameters. Among them are atmospheric opacity and surface/ice albedos. These could be changed considerably during the dust storm in 2001. This is especially important for the polar regions since, firstly, ice albedo changes dramatically by adding even a small amount of dust (Hansen 1999), and secondly, the most important parameters for sublimation insolation processes are highly affected by the atmosphere.

Below we will consider the influence of these two parameters on the evolution of polar area as well as make some investigations with the surface roughness of the area.

The most important parameter that changed between 2001 and 2003 is the atmospheric opacity. For the calculations we used two scenarios of opacity change: a clear atmosphere scenario - the opacity was set to 0.05, and dust storm scenario - the opacity varies from 0.05 to 0.2. These values are in agreement with TES observations discussed by Smith (2004).

First we run the model with parameters set closest to the observed conditions during the considered years. Fig. 4.7 shows the temperature of a smooth horizontal surface versus time. The solid line is for 2001 with varying opacity and an ice albedo 0.3, the dotted one for 2003 with a clear atmosphere of opacity 0.05 and clean ice albedo 0.5. Surprisingly, One can see that the calculated temperature curves are hardly distinguishable.

Two important effects almost cancel. The solar flux is reduced during a dust storm but at the same time the dust that precipitates onto the surface reduces the albedo and thus allows a bigger fraction of the solar radiation to be absorbed. In both cases the surface temperature stays at about 146°K for almost half of the Martian year, both during 2001 and during 2003. This temperature corresponds to the condensation temperature of CO<sub>2</sub> ice. During spring, when the sun rises above the horizon there is a rapid increase of

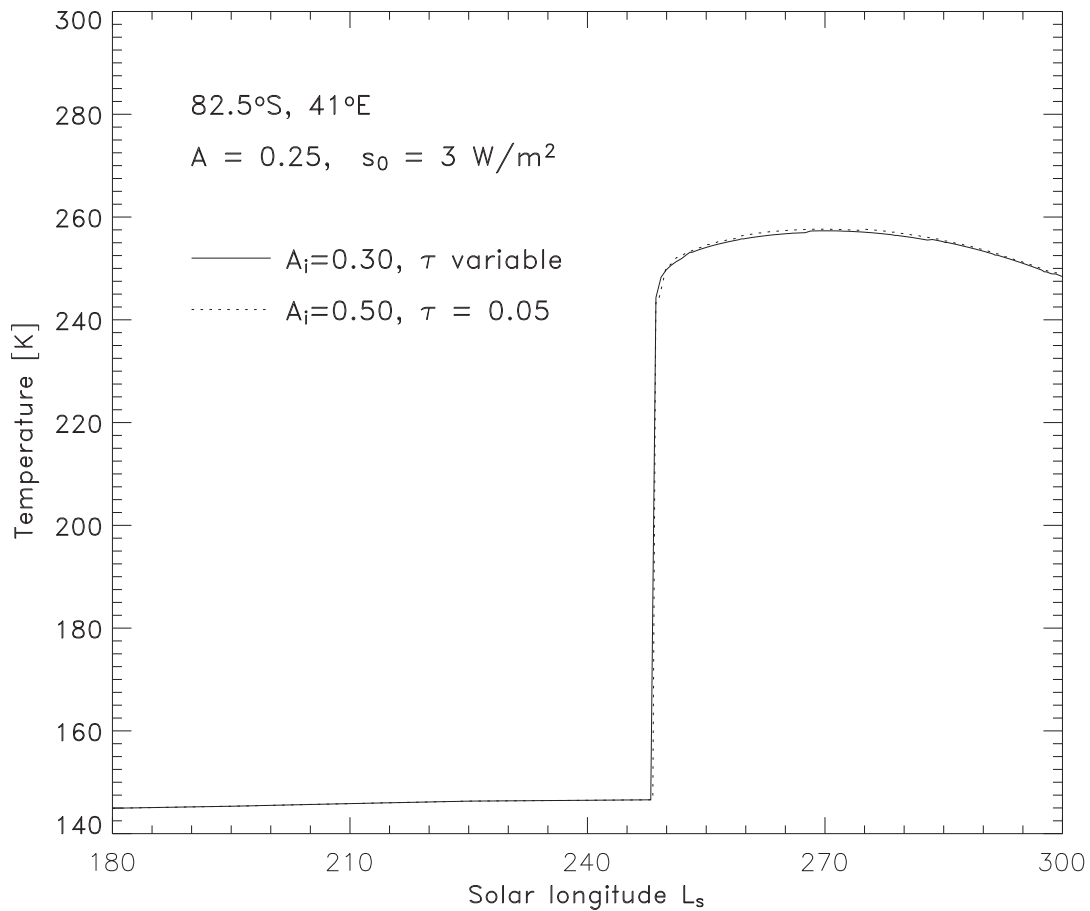


Figure 4.7: Seasonal changes of the surface temperature. Position is  $82.5^{\circ}\text{S}$  and  $41^{\circ}\text{E}$ , albedo of the ice-free surface is 0.25. The solid line is modeled temperature for the year with dust storm (2001) - atmospheric opacity changes from 0.05 to 0.2, surface ice albedo is 0.3. The dashed line corresponds to the year with clear atmosphere: opacity is 0.05, ice albedo is 0.5.

temperature around  $L_s=250^{\circ}$ . Later, after all the ice is sublimed, the temperature stabilizes around  $280^{\circ}\text{K}$ . Figure 4.8 compliments Fig. 4.7 and shows the modelled thickness of  $\text{CO}_2$  and  $\text{H}_2\text{O}$  ices for the same conditions. The maximum amount of condensed  $\text{CO}_2$  only slightly differs (around  $L_s=200^{\circ}$ ) between two years.

To separate the effect of albedo and atmospheric opacity we first fixed the ice albedo at a value 0.3 and changed the value of opacity. The result for two different scenarios for opacity behaviour is shown on Fig. 4.9 together with TES data for the same area. The dotted curve is for an opacity of 0.05 and the solid line is for the dust storm scenario. The observed TES temperatures are higher than modelled values around  $L_s=210^{\circ}$  since the contribution of the atmosphere is not completely removed from temperatures measured by TES. Unfortunately, we have no TES data for  $L_s > 250^{\circ}$  for the year 2003. For the dusty year, the agreement between the variable opacity model and the TES observations is rather good, except from the period  $L_s=250^{\circ} - 270^{\circ}$ , where the increase of TES temperatures is not as steep as in our model.

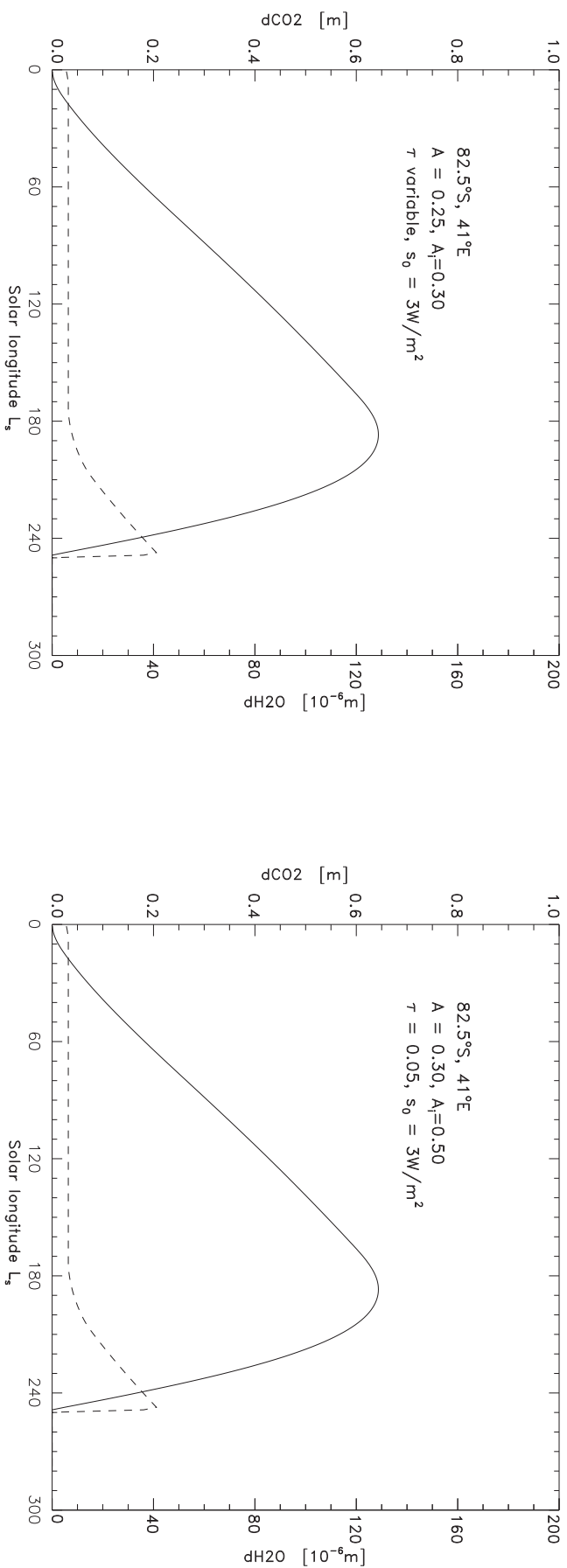


Figure 4.8: Seasonal changes of ices thickness on the surface at the position 82.5°S and 41°E. The solid line shows thickness of the CO<sub>2</sub> ice and dashed one of the H<sub>2</sub>O ice. Left panel is for the year with dust storm (2001) with atmospheric opacity changing from 0.05 to 0.2 and surface ice albedo is 0.3. Right panel corresponds to the year 2003 with clear atmosphere. Opacity is 0.05 and ice albedo is 0.5.

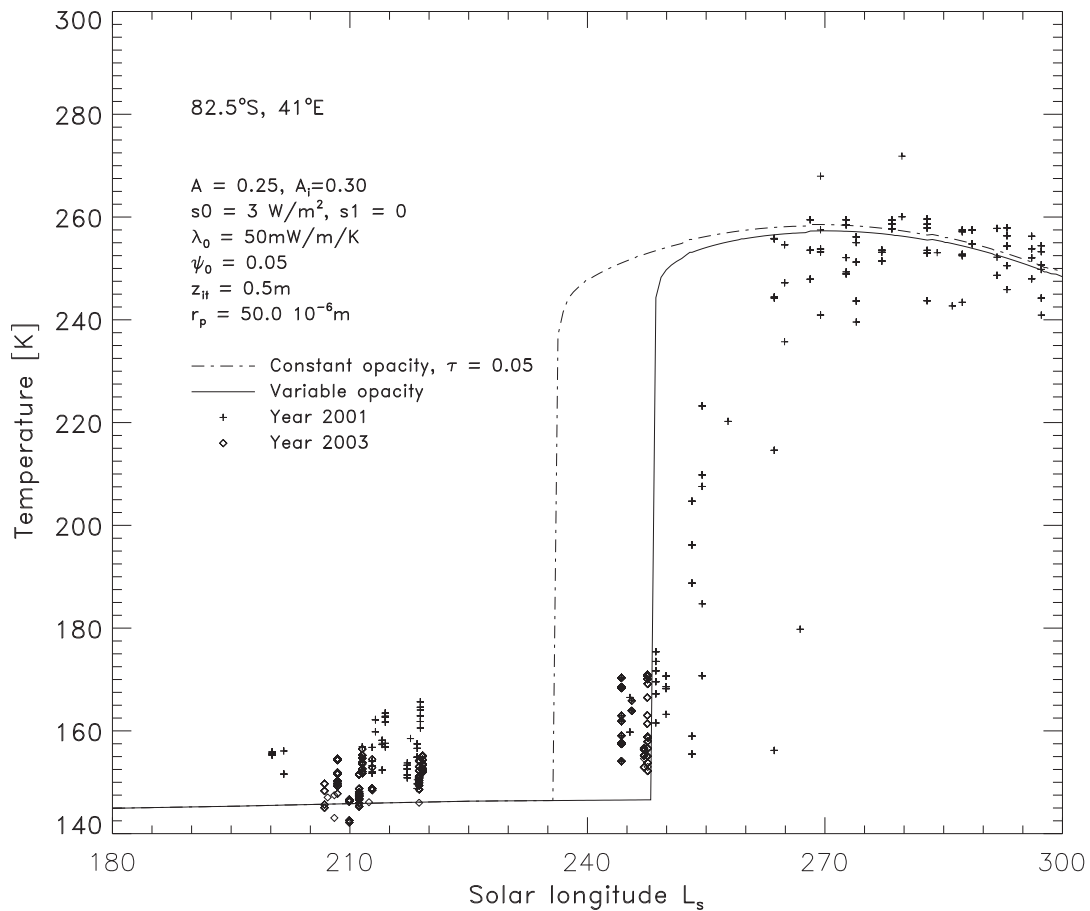


Figure 4.9: Influence of the atmospheric opacity on the surface temperature.

Further input parameter in our model that we varied is the albedo of the ice covered surface. Fig. 4.10 shows that changing the value of the ice albedo shifts the beginning of ice sublimation, i.e. brighter ice starts sublimating later since it first needs the solar flux to become strong enough.

Roughness of the surface may also have a very important impact on when the sublimation of seasonal ice starts. High resolution images of the surface reveal the presence of very rough regions (see section 4.2). We do not have the altimetry data for exactly the considered location, but expect the presence of several terraces and scarps. Any scarps that are inclined toward the equator defrost significantly earlier than horizontal surfaces, and later on the slopes oriented in the opposite direction. This, should result in some smoothing of the average temperature rise that is associated with the defrosting of the surface.

In Fig. 4.11 we present temperature profiles calculated assuming that most surface is horizontal, but some fraction has an inclination of  $1.5^\circ$  (dashed-dotted curve) or  $3^\circ$  (dashed curve). Curves show that the roughness of the surface influences the temperature in two ways:

- first, rough surface has an additional plateau near  $L_s = 245^\circ$ . It reflects the fact that areas that faced to the North get more solar energy. Ice on them sublimates first and only then

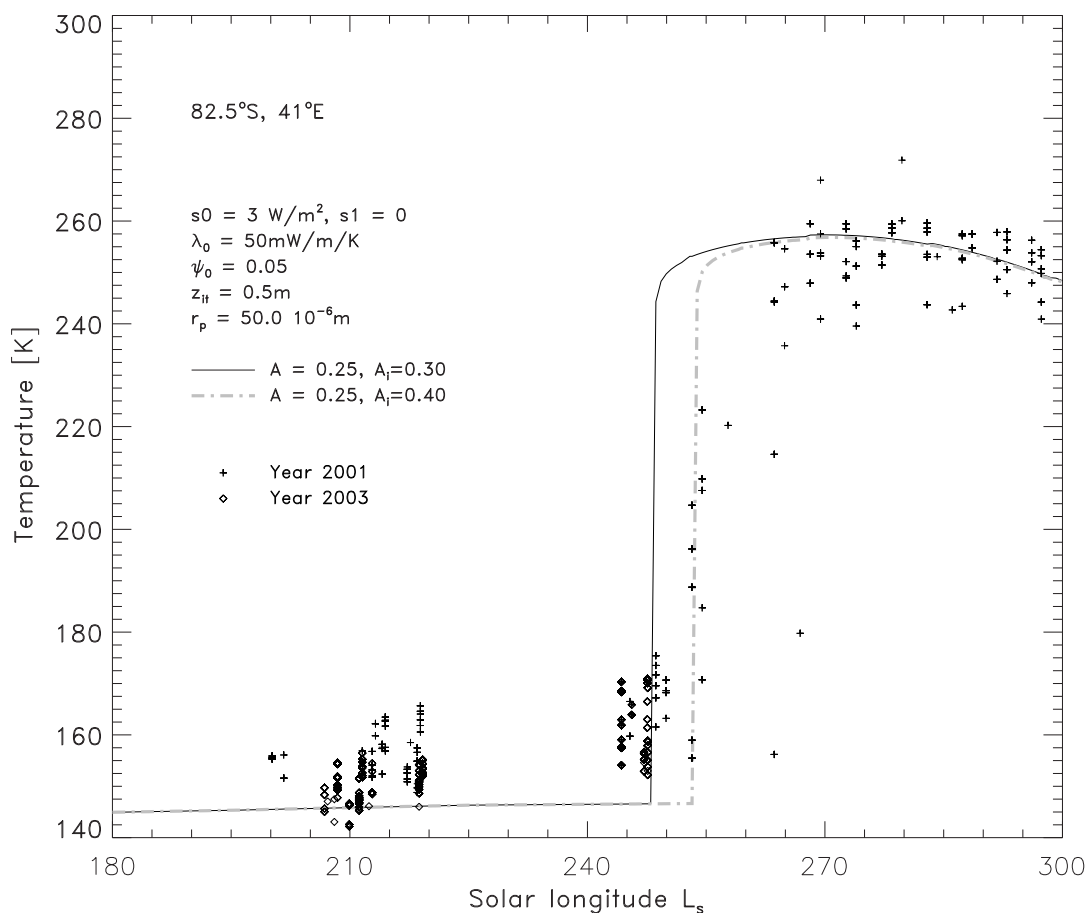


Figure 4.10: Influence of the ice albedo on the surface temperature.

the sublimation starts on horizontal areas. The rougher the surface is the higher the plateau. This is because a rougher surface has more sun-facing walls and easily gets heated. This is also connected to the second effect:

- second, the temperature after  $L_s = 250^\circ$  is higher for a rougher surface because the rough surface has a bigger area that faces the Sun, and hence, gets heated more.

Data from TES are also plotted on Fig. 4.11 and show a gradual increase of temperature, not so steep as in our calculation with a flat surface. This is in favor of the idea that the considered surface exhibits all degrees of roughness. Moreover, there is an apparent plateau in temperature rise from  $L_s = 245^\circ$  to  $L_s = 255^\circ$ . It can be explained with the mean inclination of the surface.

MOLA altimetry data shows that the considered region has a slightly inclined surface by, on average, about three degrees. From MOLA data (discussed in chapter 4.2) we could see that the whole area of the image lies in the north-facing slope with approximately  $3^\circ$  inclination. The temperature profile calculated for such a case is shown in Fig. 4.12. It shows a rather good fit to the TES temperature data with an ice albedo of 0.4 and an albedo of the defrosted surface of 0.3.

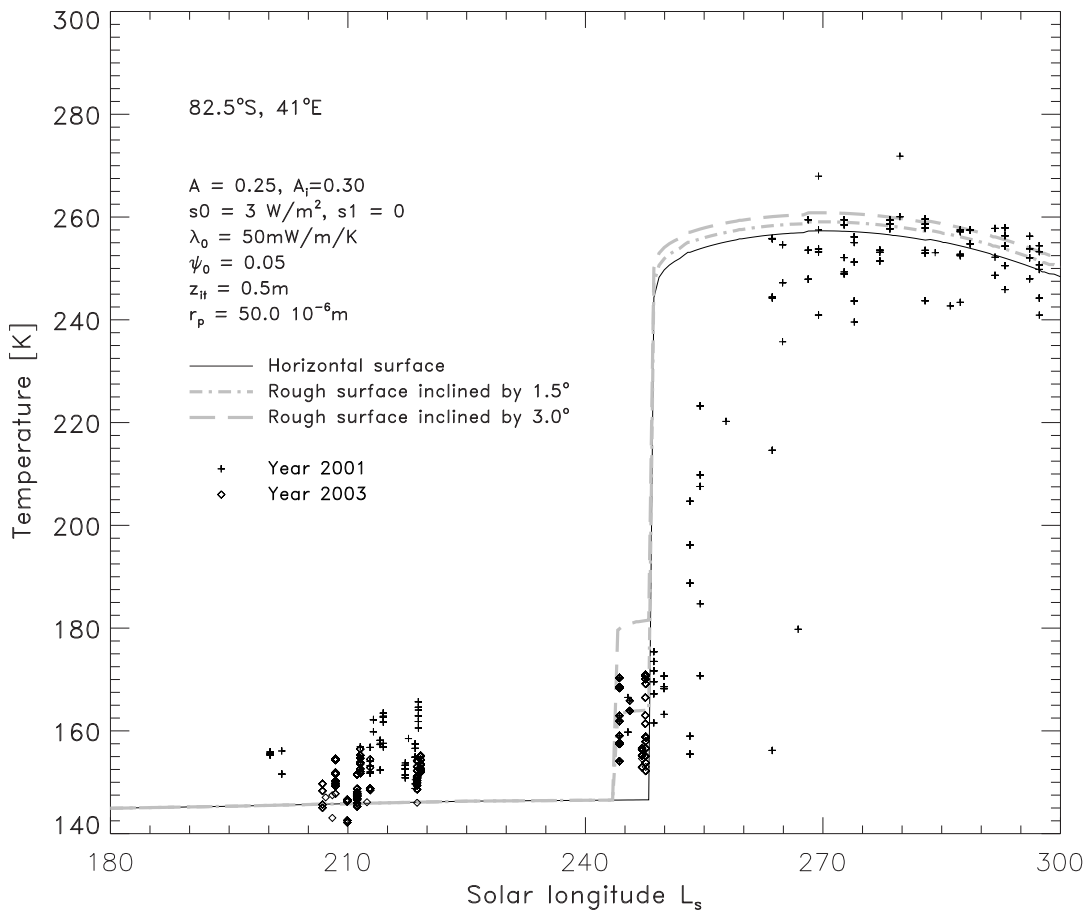


Figure 4.11: Influence of the topography on the surface temperature.

## 4.4 Conclusions

We examined the behaviour of the surface temperature and  $\text{CO}_2$  and  $\text{H}_2\text{O}$  ice covers in the location  $82.5^\circ\text{S}$ ,  $41^\circ\text{E}$  during 2001 with global dust storm, as well as during clear year 2003. Horizontal surface during both years have roughly the same temperatures. The amount of ice, as well as time of its sublimation are also the same for this two years on horizontal surface.

The edges of images e09-00028 and r08-01730 show the biggest difference in albedo of all area. At the same time they exhibit only slight difference in temperatures. This is consistent with our model results for horizontal surface under two different conditions of years 2001 and 2003. According to our modeling both images show ice free surface, or at least the surface where ice can still exist only in small portion of shadowed zones. The albedo difference comes from the dust that was precipitated from the atmosphere during the great dust storm in 2001. This dust darkened the surface in image e09-00028.

On the contrary, middle parts of both images have the same albedo, but different temperatures. During 2003 surface was slightly warmer in this area than during 2001. This may be the sign for surface being rather rough: sun-faced walls get more solar energy, ice on them sublimates earlier and faster, temperature of ice free surface rises higher. The

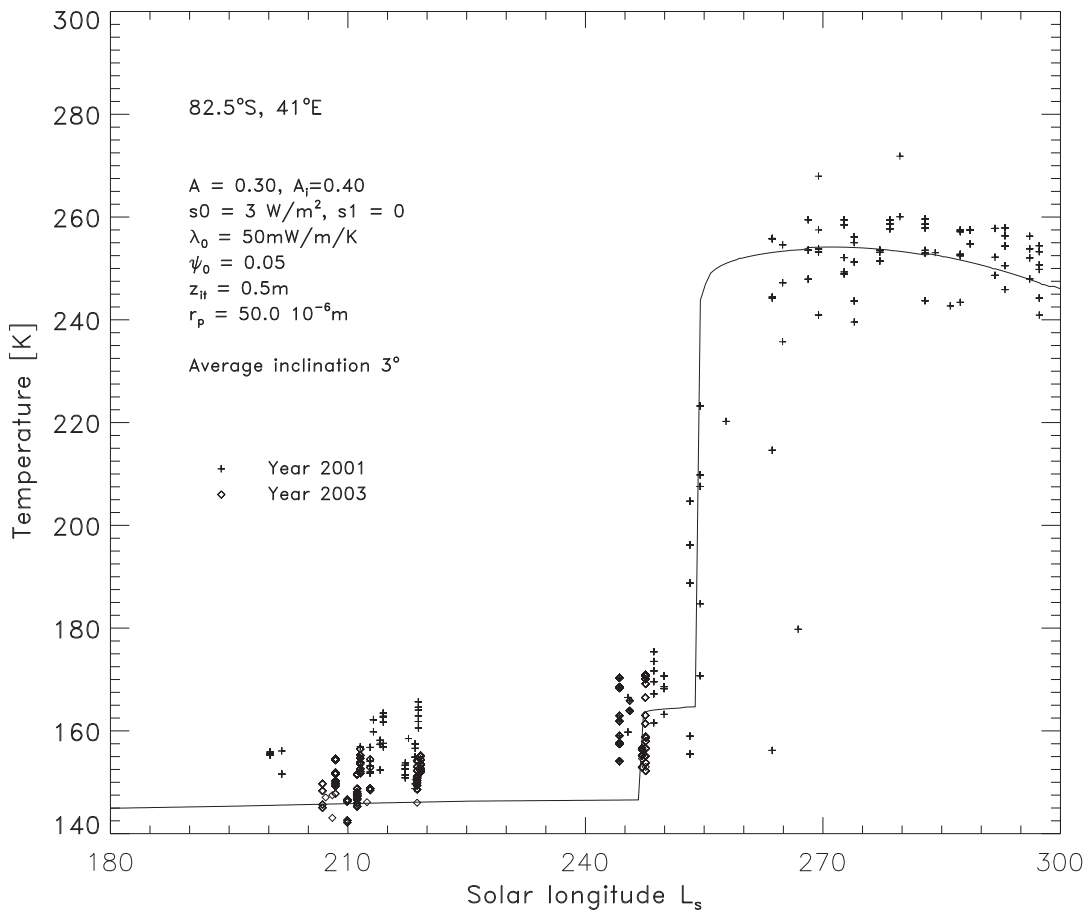


Figure 4.12: Influence of the inclination of the surface temperature.

amount of solar radiation in 2003 was bigger than in 2001 due to shadowing of the surface by dust in 2001. This allowed rough surface to get warmer in 2001, even possessing the same albedo.

The main conclusion of our modeling is that global dust storm influences the local conditions inside polar region in very different ways, depending on local properties of the surface.

# 5 Lee wave clouds in the Martian atmosphere: observations by HRSC

Lee wave clouds are a well-known phenomenon in the Earth's atmosphere. Usually they show up as large and dense clouds that hover over the tops of the mountains. They can prevail for long periods of time, and, even if there are very strong winds, they usually are almost stationary. Lee wave clouds are formed by vertical deflection of winds on a topographic obstacle; the air is forced to oscillate in the lee of the obstacle. In the crest of the wave air rises up to the cooler region where condensation occurs due to adiabatic cooling. In this way often a regular train of elongated clouds forms. This train of clouds is aligned orthogonal to the prevailing wind if the obstacle is a mountain range or an isolated mountain.

## 5.1 Observations of Martian lee-waves before HRSC

Martian clouds have been the subject of scientific interest for a long time. The understanding of their appearance, distribution and behavior is closely related to the understanding of the Martian water, dust and CO<sub>2</sub> cycles. The existence of clouds in the Martian atmosphere was beyond doubt since the time of telescopic observations. In the first paper devoted to the Martian climatology by Hess (1950) wind directions were obtained from tracking clouds on the terminator and limb of Mars during the oppositions of 1894, 1896, and 1924. Small clouds, such as streak clouds, wave clouds, dust plumes as well as properties of these clouds, were discovered from spacecraft observations. However even earlier several types of clouds were known: polar hoods, tropical clouds and, of course, dust storms.

Since lee wave clouds in the Martian atmosphere are smaller than a few kilometers, and thus too small to be visible with ground based observatories, they were observed for the first time by Mariner 9 in 1971. French et al. (1981) made a catalogue of Martian clouds from mainly Mariner 9 and a few Viking Orbiter images. They marked the following cloud categories:

- fog
- dust plumes
- streak clouds
- cloud streets
- wave clouds
- lee waves.

Added later were: thin haze, moderate haze and thick haze categories (Kahn 1984).

Subsequently lee waves were regularly detected by Viking Orbiter and Mars Global Surveyor (Wood et al. (2003)). MGS is in an almost polar orbit with a period of about two hours. Its MOC wide-angle camera produces global swaths at 7.5 km/pixel. This systematic spatial and temporal coverage offers ample opportunity to monitor clouds on Mars. Also with the 2 MOC WA color filters (red 575-625 nm; blue 400-450 nm) it is often possible to discriminate between dust and condensate clouds since the latter ones are usually much bluer. All this allowed to plot spatial and temporal distribution not only of general clouds but of their different types (Wang and Ingersoll 2002). Thus the MOC WA imagery is a big help for studying the evolution and distribution of clouds as well as their phenomenology.

Lee waves are frequently observed in both polar regions during fall and winter, and are often superimposed on haze and streak clouds. In the Northern hemisphere their number sharply increases around  $L_s \approx 170^\circ$  and quickly decreases after  $L_s \approx 20^\circ$  of the next year (Wang and Ingersoll 2002). This decrease of lee waves was also observed from Viking images (Kahn 1984). Most probably it is caused by the decrease of atmospheric water around that time. Viking occasionally observed lee waves in the Northern polar regions during the local summer. These were never seen in MOC WA images, possibly since the MOC WA images have lower spatial resolution than the Viking images: 7.5 km/pixel versus 1.5 km/pixel (Snyder 1977).

Despite a general lack of ice condensate clouds in the Southern hemisphere, many lee wave clouds were observed in the Southern polar region. The spatial extent of southern lee waves are bigger than in the North mostly because seasonal polar cap in the South is larger than in the North.

One disadvantage of MGS MOC is that the rather low spatial resolution of the wide-angle camera prohibits the detection of lee wave clouds with wavelengths less than 15 km while the narrow-angle camera has a too narrow field of view to see a whole lee wave cloud in one image. In addition it would be helpful to view the mountain on which lee wave has been formed in one image. The High Resolution Stereo Camera (HRSC) onboard of the Mars Express mission fills this gap in lee wave clouds observation.

## 5.2 Wind velocity measurement on Mars

Direct estimates of wind speeds are extremely rare for Mars. At the moment, wind speeds have been measured in three ways: direct measurements by landers, from cloud observations and from coupling of atmospheric modeling with temperature measurements.

### 5.2.1 Direct measurements of wind velocities on Mars

Two Viking landing sites and Mars Pathfinder gave direct measurements on wind speed. All three landed in equatorial/mid-latitudes areas, with the highest latitude of  $47.97^\circ\text{N}$  for the Viking 2 lander. During the ascent of Viking landers wind profiles were obtained as well (Seiff and Kirk 1977). Partial failure of the wind instrumentation on the Viking Lander 1 demanded additional reduction of data from this site (Murphy et al. 1990). The Viking landers were equipped with instruments to measure temperature and wind speeds at a height of about 1.6 meters above the surface and they also measured atmospheric

pressure (Hess et al. (1976), Hess et al. (1976)). Wind speeds were measured by two small orthogonal hot film rods (the wind sensors) approximately in the horizontal plane. The cooling rate of such rods is a measure of the wind speed. Power required to maintain the overheat was measured and converted to wind component normal to each sensor. Measured wind speeds were rather small (0.8 - 4 m/s) depending on time period (during dust storm or before and afterwards).

The wind sensors on Mars Pathfinder were similar to those of the Viking Landers. Near-surface winds on Mars were measured by a hot-wire anemometer sensor atop the meteorology mast on the Pathfinder lander, 1 m above the spacecraft solar panels. The sensor, designed and developed for Pathfinder, had 6 hot wire elements arrayed around the periphery of a 2.5 cm diameter cylinder. This arrangement permitted definition of both wind directions and their magnitudes. Winds during the early part of the mission, until sol 25, showed a systematic diurnal variation, increasing from 0 to 10 m/s during the daytime hours, peaking at 13:00, then subsiding toward sunset. Daytime winds were also very gusty, with gust magnitudes of a few m/s on a time scale of a few seconds. The winds almost disappeared at sunset, but returned after 23:00, when a night flow began which peaked at 4 m/s near 2:30 AM. From this peak until dawn, the winds were subsiding to near zero at dawn. There also appears to have been a seasonal change in the wind patterns, with more vigorous winds appearing in the morning hours near the end of the mission, early autumn (Seiff et al. 1999).

### 5.2.2 Winds derived from the cloud motion.

Wind velocities can be measured by tracing stable clouds in the atmosphere. Ground-based telescopes do not have sufficient spatial resolution for such studies. They are not able adequately resolve atmospheric features and therefore are not suitable for this type of investigations. Spacecrafts in orbit around Mars are also not very useful because they do not provide sufficient temporal resolution to make a detailed investigation. That is why the Hubble telescope is used (Mischna et. al. 1998). A set of Hubble images was used to trace cloud structures and their motion. The measured wind speeds ranged from  $15.5 \pm 8.4$  to  $44 \pm 17$  m/s.

### 5.2.3 Winds derived from modeling or analysis of temperature fields.

Wind speed estimates are also obtained using modeling of atmospheric processes with either measured or computed temperatures. Existing Mars General Circulation Models (GCM) simulates the dynamics of Mars' atmosphere including prevailing wind patterns. Two most known GCMs are those of Nasa Ames Research center and Laboratoire de Meteorologie Dynamique, Paris - LMD GCM (Forget et al. 1999). Results of simulation from LMD GCM were compiled to Martian Climate Database and available online at <http://www-mars.lmd.jussieu.fr/>

GCMs have complete coverage of the Martian globe and atmosphere and can calculate winds for any season. However for such coverage they have to sacrifice spatial and temporal resolution, which becomes not efficient to predict small scale local wind patterns. Of course, results from GCM are simulations and not observational data and they need to be confirmed with more direct measurements.

### **5.3 Mars Express (MEX) and the High Resolving Stereo Camera (HRSC), an overview**

Mars Express was launched on June 2, 2003 from the Baikonur Cosmodrome in Kazakhstan onboard a Russian Soyuz/Fregat launcher. After its six-month journey the orbiter successfully entered Martian orbit on 25 December 2003. First it manoeuvred into a highly elliptical capture orbit from which it moved into its operational near polar orbit later in January 2004. Mars Express plans to observe Mars from its orbit for at least one Martian year or 687 Earth days. This is the nominal mission lifetime, but extended mission is also planned. During this time, the point of the orbit closest to Mars (pericentre) will move around to give the scientific instruments coverage of the entire Martian surface at all kinds of viewing angles and spatial resolution.

The High Resolution Stereo Camera (HRSC) is a multi-sensor push-broom instrument comprising multiple charge coupled device (CCD) line sensors mounted in parallel for simultaneous high-resolution stereo, multi-color and multi-phase imaging of the Martian surface. An additional Super Resolution Channel provides frame images imbedded in the basic HRSC swath at five times greater resolution.

The HRSC has been originally built for the Russian space mission Mars '96. Two fully tested and calibrated flight models were produced. The launch of this spacecraft in November 1996 was unsuccessful. After that HRSC has been successfully proposed for the European Mars Express Mission in 2003. The flight spare has undergone a modification process to make it fully compliant with the Mars Express interface requirements.

The main HRSC's task is the mapping of the Martian surface. The resolution is 10 meters / pixel at an altitude of 250 km (point of closest approach to Mars).

Other objectives are:

- Climate and the role of water throughout the Martian history;
- Evolution of volcanism on Mars;
- Shaping of the Martian surface throughout time and involved geologic processes;
- Potential resources on Mars;
- Characteristics of past, present and future landing sites;
- Interactions between atmosphere and surface;
- Mapping 100% of the surface with a resolution smaller than 30 meter / pixel;
- Mapping 50% of the surface with a resolution smaller than 15 meter /pixel;
- Observation of Phobos and Deimos.

The camera is operated mainly around the pericentre of the MEX orbit, having about 40 minutes of good exposure conditions there. The other part of the orbit is used to send the data to the Earth.

The imaging electronics of the HRSC are based on the principle of a linescanner camera. The HRSC has 9 CCD line sensors. One CCD-line of the HRSC consists of 5184 light-sensitive cells (pixels). The CCD's are situated perpendicular to the flight direction and are read-out at variable frequency, which is adjusted to the ground velocity of the spacecraft. During imaging operations this creates 9 independent image strips, one from each channel.

The multi sensor concept of the HRSC combines stereo, multi-spectral and multi-phase imaging.

Stereo imaging is performed using nadir-directed, forward looking (+18.9°), and aft-looking (-18.9°) line sensors with a spectral range of  $675 \pm 90$  nm. In general, the nadir-looking channel delivers the highest resolution images, while the two outer stereo channel images are transmitted at lower resolution after the pixel summation. They are used for the extraction of 3D-data, which result finally in a digital terrain model.

Four of the channels are sensitive in the spectral range of blue ( $440 \pm 45$  nm), green ( $530 \pm 45$  nm), red ( $750 \pm 20$  nm) and near infrared ( $970 \pm 45$  nm). These color images cover the same areas as the panchromatic triple stereo images and are matched geometrically to the nadir channel panchromatic swath. The multi-spectral images are artificially decreased in spatial resolution by on-board pixel summation for lower data rates and better signal-to-noise characteristics, giving rise to data entities referred to as macro pixels.

Furthermore there are two photometric-channels with a spectral range of  $675 \pm 90$  nm, delivering data for the physical analysis of the Martian surface. These two additional panchromatic line sensors having inclined forward and backward viewing directions perform multi-phase imaging. These sensors complement the information contained in the triple stereo channels and allow the determination of photometric surface characteristics. The data from these channels are normally transmitted at lower resolution by pixel summation.

The SRC is an additional channel of the HRSC working with an area-sensor - matrix of  $1024 \times 1032$  elements. The result of each read-out is a picture of  $1024 \times 1032$  pixels, in an altitude of 250 km this corresponds to a square on the Martian surface with the edges of 2.35 km. The pixel-size in this case is 2.3 meters.

## 5.4 The formation of lee wave clouds - mathematical formulation

In this section we describe the mathematical formulation of lee waves formation in stable atmosphere. We also discussed a specific solution with specified atmospheric and boundary conditions. Full details beyond what is given below can be found in Lyra (1940).

We will limit ourselves to a two-dimensional (x is horizontal axis and z is vertical) atmospheric flow over an infinite and uniform obstacle in one direction, set to y-direction. Air mass moves horizontally with a constant velocity  $(\bar{u}, 0)$ . We will consider the case when  $\bar{u}$  is constant with altitude. After meeting the obstacle the velocity is perturbed  $(\bar{u} + u, w)$ . Due to air mass movement density and pressure in each point become also perturbed and can be set as  $\bar{\varrho} + \varrho, \bar{p} + p$ , while

$$\bar{\varrho} = \bar{\varrho}_0 e^{-z/h}$$

and

$$\bar{p} = \bar{p}_0 e^{-z/h}$$

with

$$h = \frac{\bar{p}}{g\bar{\varrho}}$$

being the scale height of the uniform atmosphere. The equations of conservation of moments in linearized form of Euler equations are,

$$\bar{\rho} \cdot \bar{u} \frac{\partial u}{\partial x} = - \frac{\partial p}{\partial x} \quad (5.1)$$

$$\bar{\rho} \cdot \bar{u} \frac{\partial w}{\partial x} = - \frac{\partial p}{\partial z} - g \varrho \quad (5.2)$$

We will further simplify the problem with the use of the Boussinesq approximation. This arises from the observation that the role of density variation in buoyancy, that is, where it is multiplied by gravity, is much more important than as a factor of the acceleration terms. Then the equation of conservation of mass given in a form of the linear continuity equation is,

$$\bar{u} \frac{\partial \varrho}{\partial x} + w \frac{\partial \bar{\rho}}{\partial z} + \bar{\rho} \left( \frac{\partial u}{\partial x} + \frac{\partial w}{\partial z} \right) = 0 \quad (5.3)$$

The fourth equation is that of the conservation of energy. It is the equation of state,

$$\frac{d(\bar{p} + p)}{dt} = \bar{c}^2 \frac{d(\bar{\rho} + \varrho)}{dt}$$

which through the equality

$$\frac{d}{dt} = (\bar{u} + u) \frac{\partial}{\partial x} + w \frac{\partial}{\partial z}$$

and after the consequent linearization takes the form:

$$\bar{u} \frac{\partial p}{\partial x} + w \frac{\partial \bar{p}}{\partial z} - \bar{c}^2 \left( \bar{u} \frac{\partial \varrho}{\partial x} + w \frac{\partial \bar{\rho}}{\partial z} \right) = 0 \quad (5.4)$$

here  $\bar{c}^2 = \gamma \bar{p} = \gamma g h$  is the square of sound speed in the atmosphere. The polytrope equality gives the constant  $\gamma = c_p/c_v$ .

Equations 5.1, 5.2, 5.3, 5.4 are the determining equations for variables  $u$ ,  $w$ ,  $\varrho$  and  $p$ . We will eliminate  $u$ ,  $\varrho$  and  $p$  from this equations to obtain only one equation for vertical speed perturbation  $w$ .

First of all  $\frac{\partial p}{\partial x}$  should be excluded from 5.1 and 5.4,  $\bar{u} \left( \frac{\partial \varrho}{\partial x} + w \frac{\partial \bar{\rho}}{\partial z} \right)$  replaced by the  $-\bar{\rho} \left( \frac{\partial u}{\partial x} + \frac{\partial w}{\partial z} \right)$  from 5.3 and with the account for the hydrostatic equation  $\frac{d\bar{p}}{dx} = -\bar{\rho} g$  it will result in:

$$\bar{u}^2 \frac{\partial u}{\partial x} = \bar{c}^2 \left( \frac{\partial u}{\partial x} + \frac{\partial w}{\partial z} \right) - g w \quad (5.5)$$

After the differentiation of 5.2 with respect to  $x$ , 5.4 with respect to  $z$  and elimination of  $\frac{\partial^2 p}{\partial x \partial z}$  one obtains,

$$\bar{u}^2 \frac{\partial^2 w}{\partial x^2} = \bar{c}^2 \frac{\partial}{\partial z} \left( \frac{\partial u}{\partial x} + \frac{\partial w}{\partial z} \right) - g \frac{\partial w}{\partial z} + \left( \frac{\bar{c}^2}{\bar{\rho}} \frac{\partial \bar{\rho}}{\partial z} + g \right) \left( \frac{\partial u}{\partial x} + \frac{\partial w}{\partial z} \right) \quad (5.6)$$

Finally through the elimination of  $\frac{\partial u}{\partial x} + \frac{\partial w}{\partial z}$  from 5.5 and 5.6 the desired equation can be found:

$$\left(1 - \frac{\bar{u}^2}{c^2}\right) \frac{\partial^2 w}{\partial x^2} + \frac{\partial^2 w}{\partial z^2} - \frac{\gamma g}{c^2} \frac{\partial w}{\partial z} + \frac{(\gamma - 1)g^2}{\bar{u}^2 c^2} w = 0 \quad (5.7)$$

With the substitution of  $w = w_1 e^{z/2h}$  and with the change of the coordinate system  $x = x_1 \sqrt{1 - \frac{\bar{u}^2}{c^2}}$  it can be rewritten in the form:

$$\Delta w_1 + \frac{4\pi^2}{\lambda^2} w_1 = 0 \quad (5.8)$$

where,

$$\lambda = \frac{2\pi\bar{u}\bar{c}}{g\sqrt{\gamma - 1 - \gamma^2 \frac{\bar{u}^2}{4c^2}}}$$

It is known that in planetary atmospheres  $\frac{\bar{u}^2}{c^2} < 10^{-3}$ , so we can consider  $x = x_1$  and  $\lambda = \frac{2\pi\bar{u}\bar{c}}{g\sqrt{\gamma - 1}}$ .

Now we only need to specify the boundary conditions. We will assume the obstacle to be rectangular. Its profile with height  $H$  and width  $B$  is defined by,

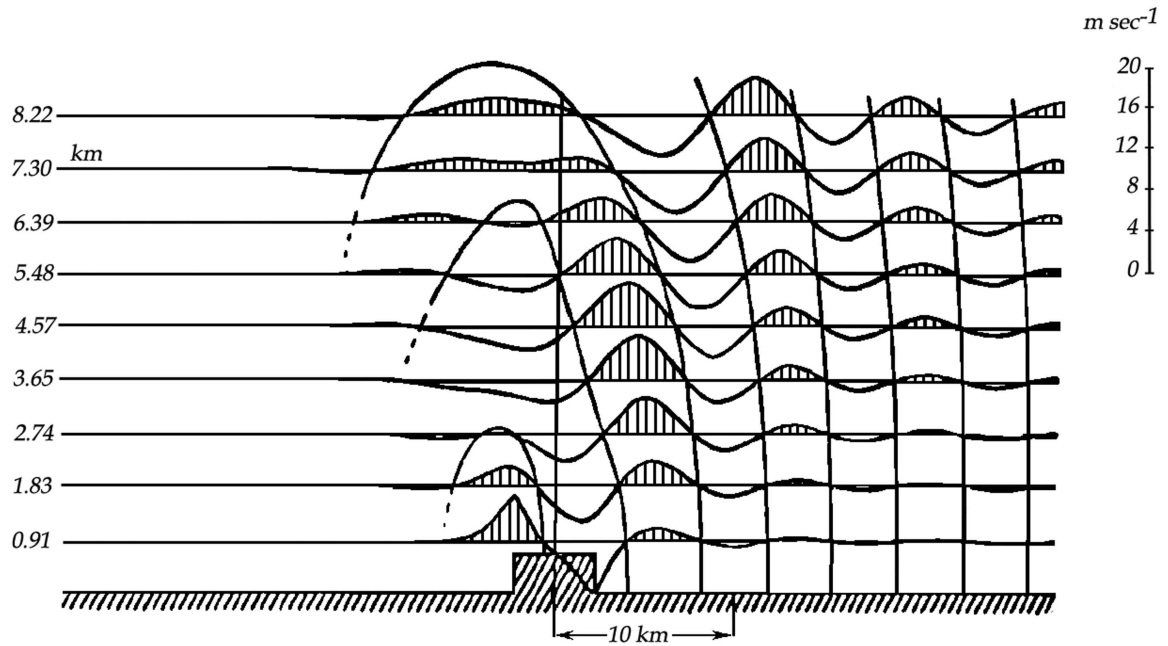


Figure 5.1: Vertical velocity field in the Earth atmosphere for the flow over the rectangular obstacle. Initial wind speed is constant. (Lyra 1940)

$$\zeta_0(x) = \begin{cases} 0 & \text{when } x < -\frac{B}{2} \\ H & \text{when } |x| \leq \frac{B}{2} \\ 0 & \text{when } x > \frac{B}{2} \end{cases} \quad (5.9)$$

The boundary conditions for the equation 5.8 are then,

$$\begin{aligned} w_1(x, z) &= \bar{u} \zeta_0'(x) \quad \text{for } z = 0 \\ \lim w_1(x, z) &= 0 \quad \text{for } \sqrt{x^2 + z^2} \rightarrow \infty \end{aligned} \quad (5.10)$$

Assuming  $\bar{u}$  to be constant Lyra obtained the solution for such a system with the help of Green's function (Lyra 1940). This solution is:

$$w = -\frac{\pi \bar{u} H B}{\lambda} z e^{z/2h} \cdot \frac{1}{B} \left[ \begin{aligned} & \frac{N_1 \left( \frac{2\pi}{\lambda} \sqrt{\left(x + \frac{B}{2}\right)^2 + z^2} \right)}{\sqrt{\left(x + \frac{B}{2}\right)^2 + z^2}} + \frac{\left(x + \frac{B}{2}\right) J_2 \left( \frac{2\pi}{\lambda} \sqrt{\left(x + \frac{B}{2}\right)^2 + z^2} \right)}{\left(x + \frac{B}{2}\right)^2 + z^2} \\ & - \frac{N_1 \left( \frac{2\pi}{\lambda} \sqrt{\left(x - \frac{B}{2}\right)^2 + z^2} \right)}{\sqrt{\left(x - \frac{B}{2}\right)^2 + z^2}} - \frac{\left(x - \frac{B}{2}\right) J_2 \left( \frac{2\pi}{\lambda} \sqrt{\left(x - \frac{B}{2}\right)^2 + z^2} \right)}{\left(x - \frac{B}{2}\right)^2 + z^2} \end{aligned} \right] \quad (5.11)$$

As one can expect the solution of the wave equation is expressed through Bessel functions. Here  $J_2$  is the second order Bessel function of the first kind and  $N_1$  is the first order Bessel function of the second kind (or Neumann function). Lyra's original plot is presented in Fig. 5.1. It shows the vertical velocity field in the Earth atmosphere for the flow over the rectangular obstacle.  $w$  is shown as a function of distance from the obstacle center and height of atmospheric layer. The horizontal velocity is set to be constant with height and  $u = 15m/sec$ .

For the comparison we have calculated the vertical velocity fields for the same wind speed and obstacle dimensions in terrestrial and martian atmospheres. Used parameters are summarized in the Table 5.1. Fig. 5.2 shows the comparison of vertical velocity fields for the Earth and for Mars. As the martian atmosphere is much thinner and less dense the lee waves are more stable there and propagate further from the obstacle. This can be one of the reasons together with high near-surface static stability that lee waves are so often observed on Mars. Also as can be seen with the same wind velocity the wavelength of the produced lee wave is bigger in martian conditions. At the same time, due to Earth dense atmosphere the lee wave perturbations are bigger in terrestrial atmosphere - air mass is deflected vertically more than in the martian atmosphere.

There is a simple connection between the wavelength of produced lee wave and the velocity of horizontal wind. As was already noted before it can be written as:

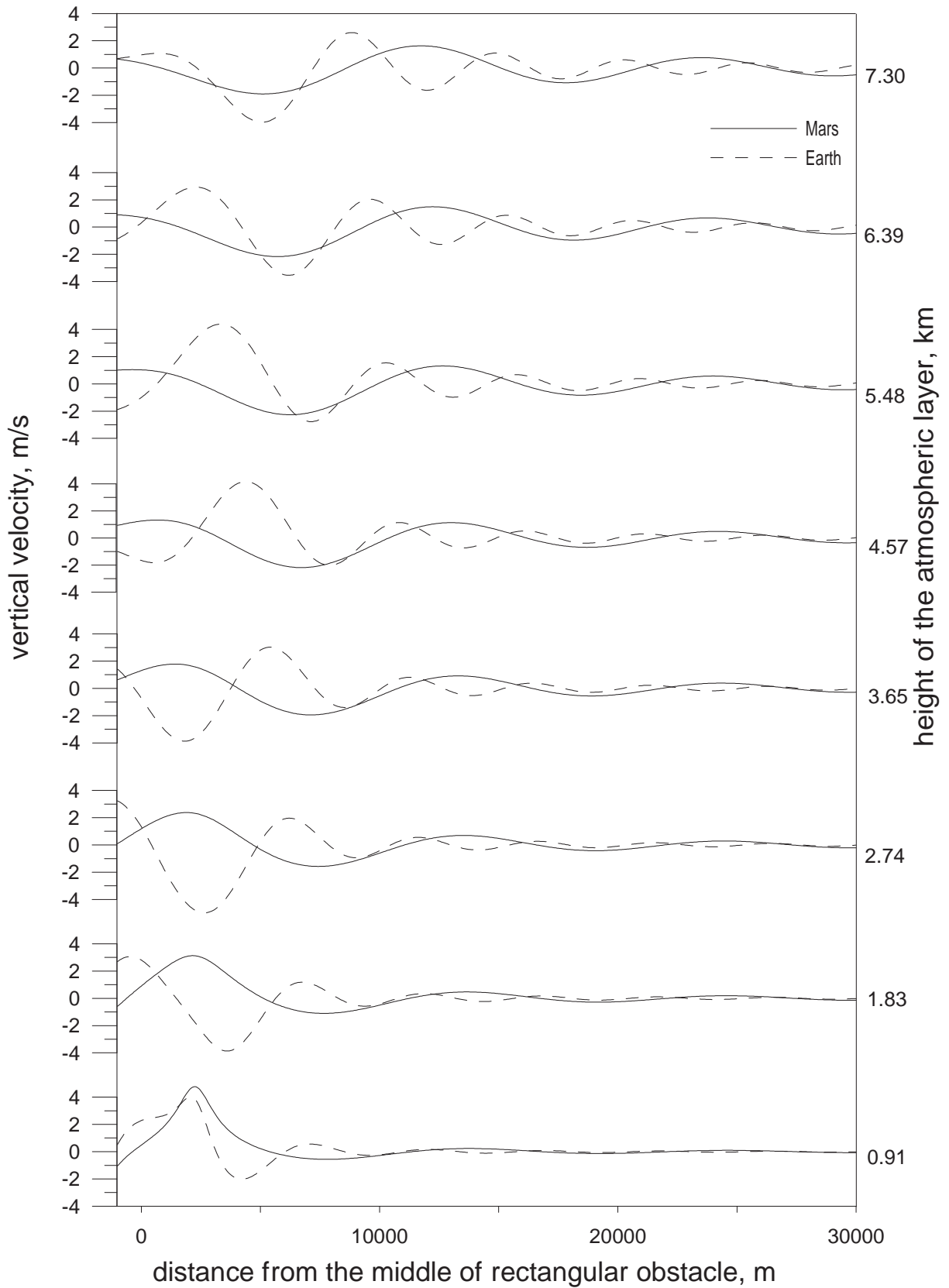


Figure 5.2: Comparison of vertical velocity fields for the Earth and Mars.

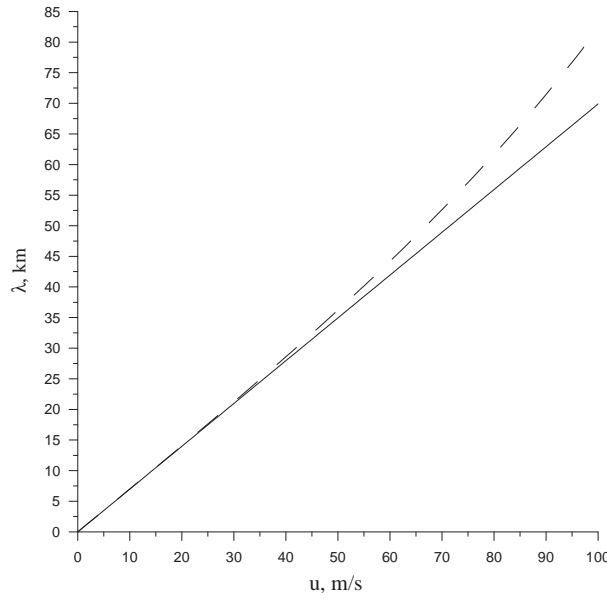


Figure 5.3: Wavelength of produced lee wave depending of horizontal wind speed.

	Earth	Mars
height of uniform atmosphere, $h$	300 km	80 km
planetary equilibrium temperature, $T$	256K	210K
sound speed, $c$	331.5 m/s	226.58 m/s
height of the obstacle, $H$	700 m	700 m
width of the obstacle, $B$	4.5 km	4.5 km
$g$	9.8 m/s <sup>2</sup>	3.69 m/s <sup>2</sup>

Table 5.1: Parameters used to calculate vertical velocity field for Mars and Earth.

$$\lambda = \frac{2\pi\bar{u}\bar{c}}{g\sqrt{\gamma - 1 - \gamma^2\frac{\bar{u}^2}{4\bar{c}^2}}} \quad (5.12)$$

or, if we consider low wind speeds, such that  $\frac{\bar{u}^2}{c^2} \approx 10^{-3}$  then we can neglect this term and write  $\lambda$  simply as:

$$\lambda = \frac{2\pi\bar{u}\bar{c}}{g\sqrt{\gamma - 1}} \quad (5.13)$$

Both curves calculated for Martian conditions are compared in the Fig.5.3. Solid line corresponds to formula 5.12 and dashed - to the formula 5.13. As one can see till the wind speeds reach 50 m/s (or corresponding wavelengths  $\approx 1.6 \cdot 10^4$ ) two formulas give almost indistinguishable results. Or in other words, using simplified formula 5.13 for the wavelength as big as  $6 \cdot 10^6$  the difference between two formulas is 8 m/s when the derived value of the wind speed is 80 m/s. This is quite a big number for Martian atmosphere according to previous wind speed estimates and model results ((Mischna et.

al. 1998), (Murphy et al. 1990), (Forget et al. 1999)).

## 5.5 Measuring wind velocities from HRSC images

The High Resolution Stereo Camera (HRSC) onboard Mars Express has atmospheric observations as one of the priorities of its scientific program. From the beginning of the mission it has detected quite a number of clouds in the Martian atmosphere. Several of them are lee wave clouds in the middle latitudes and in the polar regions. Until the present time 4 images with distinct lee wave clouds are found:

- Orbit 68: image taken on 31 January 2004, the position of the image is  $43^{\circ}\text{N}$ ,  $256^{\circ}\text{E}$ . Source mountain is outside the image frame;
- Orbit 719: image taken on 31 January 2004, North pole. Set of lee waves formed over the rims of several craters;
- Orbit 751: image taken on 31 January 2004, North pole, the position of the image is  $43^{\circ}\text{N}$ ,  $256^{\circ}\text{E}$ . Two lee wave clouds formed on the rim of crater and most probably at the edge of ice deposits.
- Orbit 1096: image taken on 31 January 2004, North pole. Source is covered by haze.

Three last images show polar lee wave clouds. They appear superimposed on the haze and streak clouds and considerably cover the underlying surface.

The wavelength, height and propagation characteristics of lee waves are mostly determined by the velocity of driving wind and the obstacle dimensions. Other critical parameters include atmospheric temperature and moisture in the flow. We used images of lee wave clouds to infer the velocity of the driving wind.

### Image taken during the orbit 68

HRSC image taken during the orbit number 68 (upper panel of Fig. 5.4) shows a lee cloud already smeared by the motion of the atmosphere. The position of the image is  $43^{\circ}\text{N}$ ,  $256^{\circ}\text{E}$ . Unfortunately, the mountain over which this lee wave was formed is outside of the image frame. The lee wave structure is distinct enough however, to measure its wavelength. On the example of this image we will describe the procedure we used to measure lee wave wavelength.

Red line on the upper panel of Figure 5.4 marks the points picked for the I/F plot shown in the lower panel. This cut is made perpendicular to the regular train of clouds that mark crests of lee wave cloud. Black curve represents raw data. One can see that periodical lee wave structure shows itself most prominent in the middle part as three pronounced crests. These raw data points were filtered with the low-pass filter (shown in right panel of Fig. 5.4) to remove high-frequency part of the signal and make the wave structure more distinguishable. The result is plotted with red curve.

The wavelength value for this lee wave cloud is 17.59 km. Using formula 5.13 we can estimate the speed of the wind producing this lee wave cloud as 25.2 m/sec.

### Image taken during the orbit 719

During the orbit 719 HRSC took the overview image of the North polar cap of Mars. Figure 5.5 shows a small subsection of this image where lee wave clouds can be seen. These clouds are formed over the set of craters. Figure 5.6 left panel shows I/F data for the line marked red in the Figure 5.5. On the right - the result of filtering is presented. For this case the filter was chosen in a way to remove not only high-frequency part of "signal" but also very low-frequency part. The trend from low values at the left wing of the plot to high values at the right part is also removed. The idea of filtering was to mark out the wave structure we observe in the image. The left and right parts of the plot shouldn't be considered because they are corrupted by the finite width of the filter.

The wavelength of the lee wave was calculated over middle eight crests and appeared to be 17.1 km. Corresponding speed of the source wind is 24.5 m/sec.

Two more examples of lee waver observed by HRSC are shown in figures 5.7 na 5.8.

## 5.6 Conclusions

HRSC detected Martian lee wave clouds in mid latitudes, near volcanoes and in polar regions.

We used images of lee wave clouds to infer wind speed.

Data from orbits 68 and 719 (North Pole) have been analyzed. The wavelength of lee waves in these data are 17.59 and 17.1 km

The inferred speeds are 25.2 and 24.5 m/sec respectively.

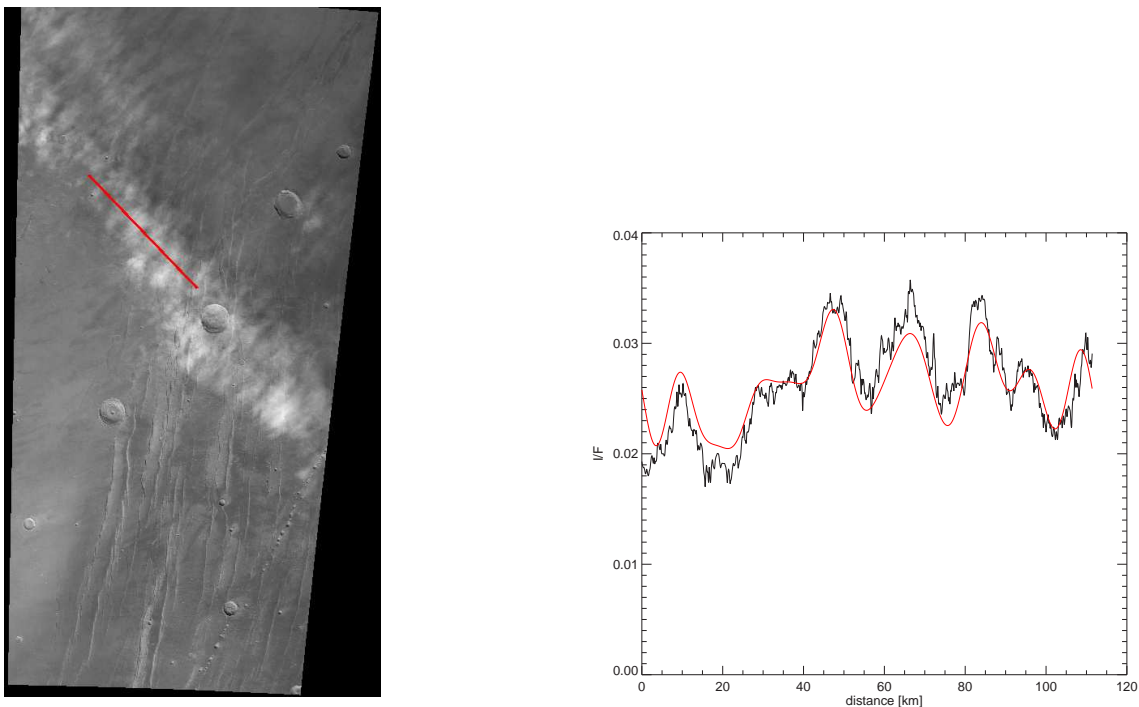


Figure 5.4: Image h0068 (left panel) with the marked cut for I/F plot shown on the right panel with black curve. Red curve is the data after applying low-pass filtering.

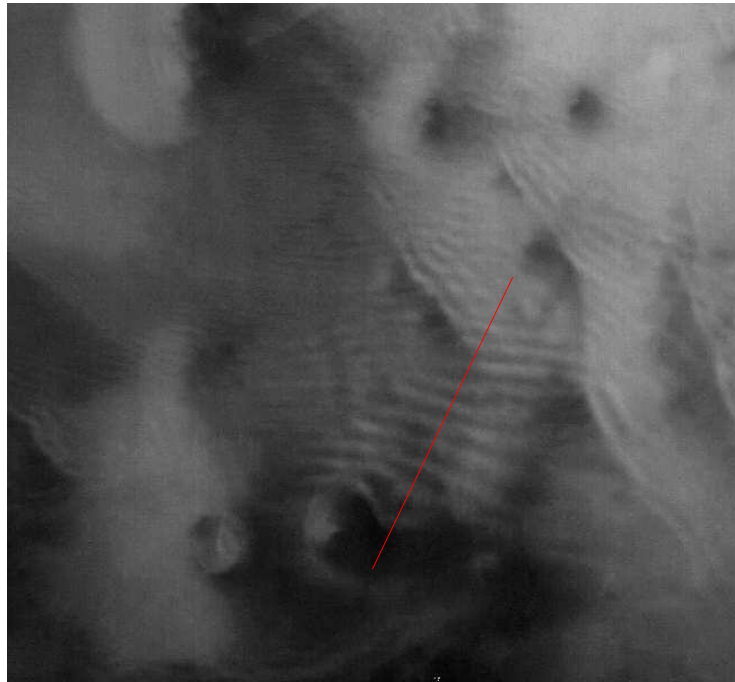


Figure 5.5: Subsection of HRSC image taken during the orbit 719. Several lee waves clouds are visible. The red line marks the position of the cut for plots shown in Fig. 5.6.

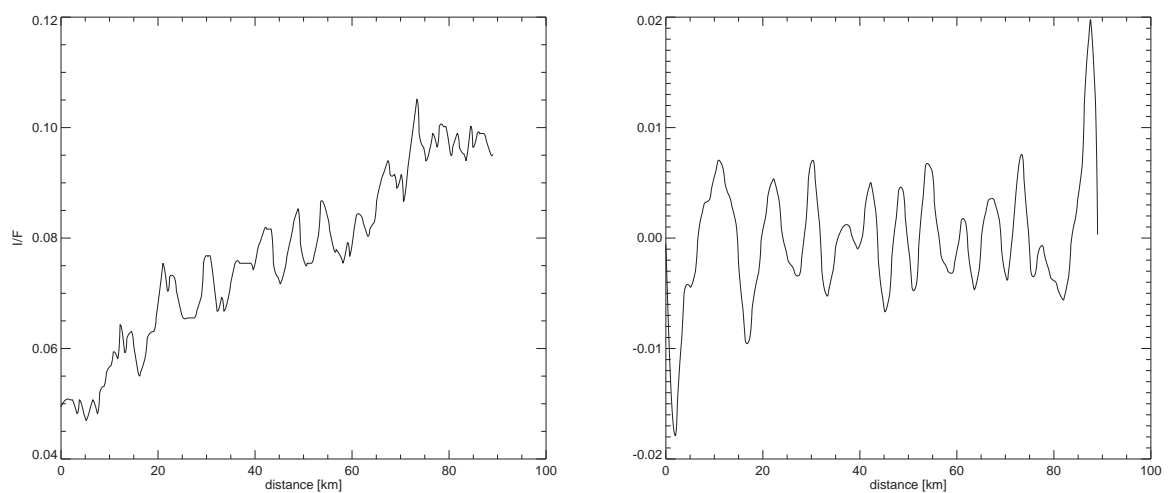


Figure 5.6: I/F plot and the result of its filtering for the image h0719.



Figure 5.7: Subsection of HRSC false color image taken during the orbit 751. It shows the lee wave cloud formed on the ice covered crater.

These values are in good agreement with the measurements of Martian wind speeds from Hubble Space Telescope images (Mischna et. al. 1998), estimates from dust devils motion (C. Stauzer, personal communication) and GCM models.

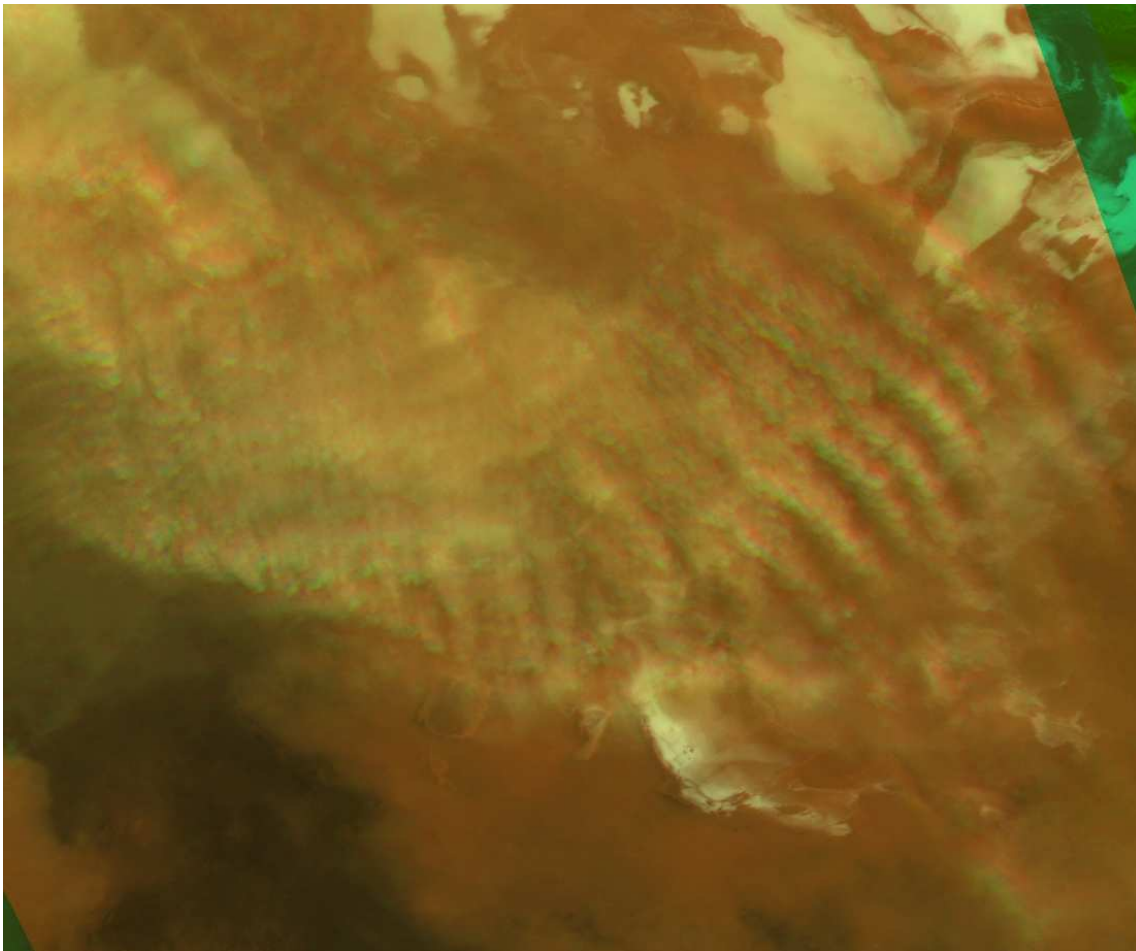


Figure 5.8: Subsection of HRSC true color image taken during the orbit 1096. Lee wave cloud is clearly visible over the North polar region.



# A Mars Global Surveyor MOC images which contain spiders patterns.

The image IDs are as they appear in Planetary Data System archive. Coordinates (west longitude and south latitude) are given in degrees for each image center.

N	image ID	longitude, °	latitude, °	$L_s$ , °
1	e07-00316	142.88	77.65	209.12
2	e07-00829	254.63	85.72	213.76
3	e07-01468	34.63	82.34	218.3
4	e07-01580	287.99	85.36	219.50
5	e07-02046	267.49	86.05	223.31
6	e07-02047	290.72	83.12	223.31
7	e07-02064	232.35	85.50	223.41
8	e08-00043	260.99	84.80	225.20
9	e08-00187	204.93	86.51	226.42
10	e08-00197	258.86	84.59	226.47
11	e08-01158	266.62	86.10	238.15
12	e08-01325	181.02	86.95	239.39
13	e08-01333	268.69	86.95	239.49
14	e08-01447	183.95	87.00	240.68
15	e08-01451	289.84	80.86	240.73
16	e08-01508	181.97	86.82	241.35
17	e08-01734	306.49	82.57	243.37
18	e09-00028	319.19	82.53	244.05
19	e09-00103	305.93	86.12	244.72
20	e09-00407	269.72	87.02	247.31
21	e09-00409	330.56	79.85	247.32
22	e09-00642	260.76	86.79	249.23
23	e09-00807	218.58	86.98	250.53
24	e09-00891	181.04	86.99	251.10
25	E09-00897	264.05	85.62	251.16
26	e09-00981	248.92	87.07	251.88

*Continued on the next page...*

A Mars Global Surveyor MOC images which contain spiders patterns.

---

N	image ID	longitude, °	latitude, °	$L_s$ , °
27	e09-01155	266.01	87.03	253.18
28	e09-01221	260.79	85.19	253.75
29	e09-01316	318.22	82.31	254.48
30	e09-01634	323.06	82.29	257.74
31	e09-02202	290.34	80.84	260.28
32	e09-02324	269.51	82.41	260.90
33	e10-00703	45.50	82.62	266.59
34	e10-01106	44.02	83.09	268.29
35	e10-02699	264.86	86.11	274.04
36	e10-04220	264.83	85.72	279.65
37	e10-04240	315.06	82.40	279.70
38	e10-04753	258.40	84.06	281.53
39	e11-01107	267.11	86.20	286.03
40	e11-01508	265.81	86.05	287.28
41	e11-02247	264.15	85.60	289.79
42	e11-02686	319.54	82.97	291.73
43	e12-00035	314.59	82.43	301.24
44	e12-00329	264.59	85.78	302.80
45	e12-00589	255.33	85.90	304.16
46	e12-00619	317.36	81.80	304.30
47	e12-00700	238.64	85.86	304.74
48	e12-00836	289.95	83.32	305.46
49	e12-00953	294.14	85.94	306.04
50	e12-01762	293.47	81.93	310.07
51	e12-02568	209.96	86.00	314.28
52	e12-02570	319.78	82.98	314.29
53	e12-03003	282.81	83.01	316.59
54	e12-03058	318.43	81.30	316.87
55	m03-07160	141.07	78.47	183.45
56	m07-00604	187.37	73.69	199.67
57	m07-01173	283.03	82.73	201.08
58	m07-02251	245.89	87.00	204.80
59	m07-02525	241.07	87.00	206.04
60	m07-03438	150.64	87.03	208.41
61	m07-04841	286.99	81.99	212.89
62	m07-05316	280.71	82.58	214.14
63	m08-00442	181.93	87.02	217.25
64	m08-01855	179.99	86.99	220.44
65	m08-02004	178.21	87.04	221.05
66	m08-02352	161.97	87.03	222.31
67	m08-02778	237.70	87.03	223.74
<i>Continued on the next page...</i>				

A Mars Global Surveyor MOC images which contain spiders patterns.

N	image ID	longitude, °	latitude, °	$L_s$ , °
68	m08-02941	164.01	87.01	224.20
69	m08-03260	182.49	87.01	224.91
70	m08-03267	262.85	80.74	224.91
71	m08-03818	172.37	81.18	226.03
72	m08-03864	209.14	75.28	226.08
73	m08-04688	284.38	82.02	227.77
74	m08-04874	292.45	81.81	228.18
75	m08-05207	248.23	87.07	228.89
76	m08-06175	291.44	83.10	231.41
77	m08-06477	10.06	79.85	232.18
78	m08-06582	157.39	76.57	232.44
79	m08-07008	230.72	87.10	233.36
80	m08-07362	181.77	87.01	233.93
81	m08-07706	190.54	82.71	234.70
82	m08-07997	275.47	83.74	235.27
83	m08-08054	192.70	77.90	235.37
84	m09-00126	181.09	86.94	235.88
85	m09-00157	265.87	86.14	235.94
86	m09-00454	285.09	78.26	236.56
87	m09-00528	265.49	87.13	236.66
88	m09-00570	273.96	86.96	236.71
89	m09-00757	184.84	87.01	237.17
90	m09-01070	182.86	86.84	237.84
91	m09-01350	189.90	86.75	238.52
92	m09-01352	262.65	85.80	238.52
93	m09-01372	194.51	76.52	238.62
94	m09-01520	291.59	83.65	239.19
95	m09-01567	268.57	87.00	239.29
96	m09-01714	86.06	82.24	239.70
97	m09-01716	151.62	87.10	239.70
98	m09-01744	240.18	84.67	239.76
99	m09-01967	134.54	86.55	240.38
100	m09-02042	296.07	80.96	240.48
101	m09-02066	172.87	75.63	240.53
102	m09-02096	266.73	87.04	240.58
103	m09-02567	126.97	86.43	241.67
104	m09-02598	245.80	84.94	241.72
105	m09-02662	318.28	81.93	241.83
106	m09-02835	224.26	77.01	242.29
107	m09-03082	263.61	85.62	243.07
108	m09-03312	189.66	78.49	243.53

*Continued on the next page...*

A Mars Global Surveyor MOC images which contain spiders patterns.

---

N	image ID	longitude, °	latitude, °	$L_s$ , °
109	m09-03463	294.42	82.76	243.74
110	m09-03484	177.45	76.83	243.79
111	m09-03807	280.88	80.38	244.62
112	m09-04068	267.46	87.01	245.09
113	m09-04379	261.29	86.77	245.71
114	m09-05362	143.34	87.06	248.82
115	m09-05567	154.31	87.03	249.49
116	m09-05981	286.43	79.68	251.15
117	m09-06313	319.08	82.89	252.50
118	m09-06356	21.24	84.16	252.60
119	m09-06428	264.73	87.00	252.97
120	m09-06652	181.67	86.99	254.11
121	m09-05066	283.54	79.97	247.88
122	m10-00071	269.82	86.95	254.94
123	m10-00442	284.79	80.72	256.75
124	m10-01138	45.59	82.65	260.48
125	m10-01846	289.66	81.65	263.27
126	m10-02442	226.68	77.44	267.04
127	m10-02495	305.18	81.67	267.19
128	m10-03023	308.85	81.59	270.43
129	m10-03415	288.14	81.43	272.33
130	m10-03666	260.71	85.67	273.61
131	m10-03668	283.91	81.34	273.61
132	m11-00396	266.34	85.85	275.56
133	m11-01070	337.48	79.58	278.46
134	m11-01739	264.54	87.12	281.40
135	m11-02315	174.98	87.05	283.78
136	m11-02665	194.74	76.92	285.60
137	m11-02723	287.84	80.11	285.75
138	m11-03042	230.26	77.26	286.90
139	m11-03062	189.11	87.02	286.95
140	m11-03107	246.80	87.09	287.05
141	m11-03217	174.78	87.03	287.55
142	m11-03283	261.17	87.08	287.70
143	m11-03346	192.75	77.90	288.10
144	m11-03348	194.63	76.63	288.11
145	m11-03360	226.41	77.02	288.16
146	m11-03525	209.26	77.70	288.76
147	m11-03583	194.70	76.64	289.36
148	m11-03774	288.28	79.22	290.15
149	m11-03956	326.44	81.48	291.10

*Continued on the next page...*

A Mars Global Surveyor MOC images which contain spiders patterns.

N	image ID	longitude, °	latitude, °	$L_s$ , °
150	m11-03968	169.96	79.19	291.20
151	m11-04019	253.71	85.84	291.40
152	m11-04046	261.95	86.83	291.45
153	m11-04128	194.68	76.59	291.85
154	m11-04140	194.49	76.72	291.90
155	m11-04156	189.92	86.74	291.95
156	m12-00159	302.95	82.12	294.18
157	m12-00425	321.16	82.42	295.22
158	m12-00456	298.91	82.25	295.41
159	m12-00543	260.81	85.13	295.76
160	m12-00680	128.00	86.48	296.30
161	m12-02005	288.10	84.19	304.60
162	m12-02550	280.63	85.05	308.20
163	m12-02657	181.86	87.02	309.16
164	m12-02778	190.94	78.29	309.64
165	m12-02797	286.00	84.16	309.83
166	m12-02868	280.25	82.24	310.40
167	m13-01816	165.78	74.84	324.86
168	m13-01827	193.20	76.23	324.90
169	m14-01110	184.79	86.69	336.25
170	m14-01682	191.49	72.87	340.58
171	m14-01838	186.60	73.58	341.66
172	m15-00027	190.36	72.99	344.38
173	m16-00550	187.56	73.94	5.24
174	m11-00280	274.77	86.97	275.04
175	m11-02188	246.94	87.13	283.28
176	m11-02878	174.24	87.06	286.3
177	m12-00888	180.79	87.02	297.58
178	e09-00039	340.5	84.23	244.1
179	e10-02085	86.09	82.01	271.84
180	r04-00150	142.55	78.04	162.38
181	r04-01518	333.46	81.24	171.59
182	r04-02327	326.59	82.25	176.7
183	r05-00379	199.3	86.75	179.45
184	r05-00417	242.68	87.01	179.54
185	r05-00418	283.6	85.43	179.54
186	r05-00612	245.98	85.76	180.65
187	r05-00678	208.05	74.17	181.11
188	r05-00695	203.72	85.61	181.16
189	r05-00714	241.47	84.54	181.2
190	r05-00791	239.81	85.98	181.8

*Continued on the next page...*

A Mars Global Surveyor MOC images which contain spiders patterns.

---

N	image ID	longitude, °	latitude, °	$L_s$ , °
191	r05-00813	273.95	87.12	181.94
192	r05-01089	305.3	84.43	184.22
193	r05-01145	187.03	86.05	184.64
194	r05-01156	211.21	86.24	184.69
195	r05-01640	183.41	86.77	188.21
196	r05-01878	240.15	85.89	190.05
197	r05-02149	148.37	79.74	192.24
198	r05-02161	175.35	80.73	192.29
199	r05-02179	186.13	86.7	192.38
200	r05-02372	246.9	85.31	199.82
201	r06-00190	262.71	85.78	196.7
202	r06-00553	202.91	87.46	199.76
203	r06-00570	209.86	86.92	199.8
204	r06-00959	99.55	81.48	205.83
205	r06-00983	266.11	83.72	205.88
206	r06-01000	227.88	87.37	205.93
207	r06-01143	336.49	79.12	206.86
208	r06-01197	132.42	87.38	207.01
209	r06-01284	254.01	85.78	207.75
210	r06-01343	64.42	81.41	208.25
211	r06-01707	171.41	80.66	210.68
212	r06-01729	200.23	80.52	210.73
213	r06-01842	206.76	69.83	211.98
214	r06-01860	254.82	85.73	212.13
215	r07-00266	231.53	80.41	215.19
216	r07-00386	125.43	87.53	216.99
217	r07-00648	298.19	87.52	218.61
218	r07-00778	157.13	87.04	219.67
219	r07-00967	193.44	86.56	220.89
220	r07-00973	233.13	85.69	220.94
221	r07-01092	149.88	87.43	222.16
222	r07-01096	253.32	79.16	221.21
223	r07-01151	186.43	85.61	222.77
224	r07-01160	264.05	80.13	222.87
225	r07-01188	197.07	79.98	223.02
226	r07-01189	243.54	87.27	223.02
227	r07-01202	249.21	86.03	223.07
228	r07-01266	254.61	85.88	223.53
229	r07-01390	31.09	78.11	224.65
230	r07-01487	155.89	75.72	225.51
231	r07-01740	163.98	78.49	227.82
<i>Continued on the next page...</i>				

A Mars Global Surveyor MOC images which contain spiders patterns.

N	image ID	longitude, °	latitude, °	$L_s$ , °
232	r07-02037	265.76	86.16	230.63
234	r07-02226	209.72	85.78	231.82
235	r07-02245	250.77	84.12	231.87
236	r08-00241	96.07	81.18	233.77
237	r08-00349	151.95	87.19	234.39
238	r08-00368	184.92	87.13	234.44
239	r08-00402	63.33	81.57	234.75
240	r08-00460	273.57	87.23	235.26
241	r08-00598	305.27	81.38	236.09
242	r08-00677	266.61	87.03	236.5
243	r08-00912	213.38	73.95	239.19
244	r08-01153	266.11	86.59	241.67
245	r08-01164	312.89	85.34	241.72
246	r08-01192	265.03	85.8	241.83
247	r08-01195	33.66	77.75	241.83
248	r08-01248	171.06	87.16	242.19
249	r08-01261	197.59	87.14	242.24
250	r08-01280	224.36	87.18	242.29
251	r08-01296	187.2	85.39	242.34
252	r08-01314	189.04	74.91	242.39
253	r08-01317	271.27	87.32	242.4
254	r08-01336	252.55	86.13	242.45
255	r08-01391	66.59	81.26	242.81
256	r08-01443	189.55	86.49	242.94
257	r08-01445	282.04	85.03	242.97
258	r08-01466	242.08	87.24	243.02
259	r08-01610	306.47	82.64	243.64
260	r08-01628	309	86.35	243.69
261	r08-01665	63.6	81.65	243.85
262	r08-01730	319.17	82.55	244.31
263	r08-01746	204.87	80.99	244.36
264	r08-01805	38.15	75.53	244.72
265	r08-01853	156.08	85.81	244.88
266	r08-01884	303.45	86.42	244.99
267	r08-01907	234.26	85.19	245.04
268	r08-02072	216.81	85.09	246.13
269	r08-02105	308.22	86.31	246.33
270	r08-02301	256.19	86.36	248.2
271	r08-02518	64.12	81.52	249.96
272	r09-00282	290.44	83.58	254.27
273	r09-00564	284.71	80.76	255.98

*Continued on the next page...*

A Mars Global Surveyor MOC images which contain spiders patterns.

---

N	image ID	longitude, °	latitude, °	$L_s$ , °
274	r09-00605	292.72	83.53	256.24
275	r09-00763	305.79	79.35	257.59
276	r09-01017	258.67	87	259.3
277	r09-01019	318.27	80.51	259.3
278	r09-01167	264.1	86.39	259.92
279	r09-01196	325.7	82.4	259.97
280	r09-01303	302.91	81.79	260.18
281	r09-01328	327.7	80.21	260.23
282	r09-01557	320.42	82.73	261.27
283	r09-01662	77.88	81.64	261.47
284	r09-01820	214.33	75.21	261.99
285	r09-01821	242.52	85.33	261.99
286	r09-01916	64.14	81.5	262.35
287	r09-02028	73.42	81.78	262.77
288	r09-02085	254.51	85.35	263.13
289	r09-02143	333.06	81.23	263.23
290	r09-02196	266.89	85.28	263.33
291	r09-02305	251.6	86.37	263.8
292	r09-02326	246.12	87.08	263.85
293	r09-02374	255.85	85.78	263.95
294	r09-02403	46.66	78.99	264.01
295	r09-02433	70.54	81.3	264.06
296	r09-02520	290.03	83.95	264.47
297	r09-02567	241.24	85.91	264.57
298	r09-02740	260.52	86.89	265.14
299	r09-02921	313.18	86.6	265.86
300	r09-02948	264.58	85.81	265.91
301	r09-03024	41.8	74.53	266.22
302	r09-03025	46.69	78.97	266.22
303	r09-03136	324.88	84.38	266.48
304	r09-03251	253.11	86.48	267.05
305	r09-03268	247.25	87.08	267.1
306	r09-03433	240.31	86.29	267.67
307	r09-03461	299.78	82.65	267.72
309	r09-03604	269.28	87.09	268.44
310	r09-03607	348.89	79.32	268.44
311	r09-03639	23.16	74.31	268.49
312	r09-03724	106.99	83.21	268.9
313	r09-03725	191.5	86.82	268.9
314	r09-03885	56.18	81.7	269.47
315	r09-03907	86.05	82	269.52
<i>Continued on the next page...</i>				

A Mars Global Surveyor MOC images which contain spiders patterns.

---

N	image ID	longitude, °	latitude, °	$L_s$ , °
316	r09-03960	216.52	87	269.62
317	r09-03979	241.23	87.07	269.67
318	r09-04001	245.41	86.82	269.73
319	r09-04023	260.24	86.32	269.78
320	r09-04077	65.8	81.52	269.88
321	r09-04104	95.48	80.99	269.93
322	r09-04180	223.16	87.03	270.29
323	r09-04287	47.39	79.51	270.75
324	r09-04341	280.9	80.42	270.91
325	r09-04363	158.16	76.55	270.96
326	r09-04365	246.98	87.01	270.96



# Bibliography

- Aharonson, Oded, Zuber, Maria T., Smith, David E.; Neumann, Gregory A., Feldman, William C., Prettyman, Thomas H., 2004, Depth, distribution, and density of CO<sub>2</sub> deposition on Mars *Journal of Geophysical Research*, Volume 109, Issue E5, E05004
- Allison, M. 1997, Accurate analytic representations of solar time and seasons on Mars with applications to the Pathfinder/Surveyor missions, *Geophys. Res. Lett.* 24, 1967-1970
- Ansel C. Ugural, 1999, *Stresses in plates and shells*, 2nd ed., Boston: McGraw-Hill, 502p.
- Arden L. Albee, Raymond E. Arvidson, Frank Palluconi, and Thomas Thorpe, 2001, Overview of the Mars Global Surveyor mission, *Journal of Geophysical Research*, Vol. 106, p. 23,29123,316
- Bell, J. F., Wolff, M. J., Noll, K., Lubenow, A., Noe-Dobrea, E.; Hubbard, M. Y., Morris, R. V., Videen, G., Shkuratov, Y., 2003, Hubble Space Telescope Imaging and Spectroscopy of Mars During the Extremely Close Approach of 2003, American Geophysical Union, Fall Meeting 2003, abstract #RP12C-01
- Bibring, J.-P., Langevin, Y., Poulet, F., Gendrin, A., Gondet, B., Berthe, M., Soufflot, A., Drossart, P., Combes, M., Bellucci, G., Moroz, V.i, Mangold, N., Schmitt, B., and the OMEGA team, 2004, Perennial water ice identified in the south polar cap of Mars, *Nature*, Vol. 428, p.627-630
- Brown, R.H. and Matson, D.L., 1987, Thermal effects of insolation propagation into the regoliths of airless bodies. *Icarus* 72, p. 84-94.
- Byrne, S.; Ingersoll, A. P., 2002, A Sublimation Model for the Formation of the Martian Polar Swiss-cheese Features, *Bulletin of the American Astronomical Society*, Vol. 34, p.837
- Cantor, B.A., Wolff, M.J., James, P.B., Higgs, E., 1998, Regression of martian north polar cap: 1990-1997 Hubble Space Telescope observations, *Icarus*, V. 136, p. 175-191.
- Cantor, Bruce A., James, Philip B., Caplinger, Michael, Wolff, Michael J., 2001, Martian dust storms: 1999 Mars Orbiter Camera observations, *Journal of Geophysical Research*, Volume 106, pp. 23653-23688
- Christensen P.R. and Zurek, R.W., 1984, Martian north polar hazes and surface ice: Results from the Viking survey/completion mission, *Journal of Geophysical Research*, Vol. 89, p. 4587-4596

- Christensen Philip R., Anderson, Donald L., Chase, Stillman C., Clark, Roger N., Kieffer, Hugh H., Malin, Michael C. Pearl, John C. Carpenter, James; Bandiera, Nuno; Brown, F. G., 1992, Thermal emission spectrometer experiment - Mars Observer mission, *Journal of Geophysical Research*, Vol. 97, p. 7719-7734
- Colaprete, A. and Toon, O.B., 2002, Carbon dioxide snow storms during the polar night on Mars, *Journal of Geophysical Research*, Vol. 107
- Fishbaugh, K.E. and Head III, J.W., 2001, Comparison of the North and South Polar Caps of Mars: New Observations from MOLA Data and Discussion of Some Outstanding Questions, *Icarus*, Vol. 154, p. 145-161
- Focas, J.H., 1961, Etude photometrique et polarimetrique des phenomenes saisonniers de la planete Mars, *Ann. Astrophys.* 24, p. 309-325
- Focas, J.H., 1962, Seasonal evolution of the fine structure of the dark areas on Mars, *J. Planet. Space Sci.* 9: 371-381
- Forget, F., Hansen, Gary B., Pollack, James B., 1995, Low brightness temperatures of Martian polar caps: CO<sub>2</sub> clouds or low surface emissivity?, *Journal of Geophysical Research*, Volume 100, Issue E10, p. 21219-21234
- Forget, F., Hourdin, F., and Talagrand, O., 1998, CO<sub>2</sub> snowfall on Mars: Simulation with a general circulation model. *Icarus*, 131, p.302-316
- Forget, F., Frederic Hourdin, Richard Fournier, Christophe Hourdin and Oliver Talagrand, Matthew Collins, Stephen R.Lewis and Peter L. Read, Jean-Paul Huot, 1999, Improved general circulation models of the Martian atmosphere from the surface to above 80 km, *Journal of Geophysical Research*, Vol. 104, p.24,155-24,175
- French, Richard G., Gierasch, Peter J., Popp, Bruce D. and Roger J. Yerdon, 1981, Global patterns in cloud forms on Mars, *Icarus*, Vol. 45, p. 468-493
- Garry, J.R.C., Wright, I.P, 2004, Coring experiment with cryogenic water and carbon dioxide ices - toward planetary surface operations, *Planetary and Space Science*, Vol. 52, p. 823-831
- Hansen, J.E. and Travis, L.D., 1974, Light scattering in planetary atmospheres. *Space Science reviews*, 16, p. 527-610
- Hansen, Gary B., 1999, Control of the radiative behavior of the Martian polar caps by surface CO<sub>2</sub> ice: Evidence from Mars Global Surveyor measurements, *Journal of Geophysical Research*, vol. 104, p. 16,471-16,486
- Hess, S.L. 1950, Some aspects of the meteorology of Mars, *Journal of Meteorology*, 7:1-13
- Hess, S.L., Henry, R.M., Leovy, C.B., Ryan, J.A., Tillman, J.E., Chamberlain, T.E., Cole, H.L., Dutton, R.G., Greene, G.C., Simon, W.C., and Mitchell, J.L., 1976, Preliminary meteorological results on Mars from the Viking 1 Lander. *Science* 193, p. 788-791

- Hess, S.L., Henry, R.M., Leovy, C.B., Ryan, J.A., Tillman, J.E., 1977, Meteorological results from the surface of Mars: Viking 1 and 2, *Journal of Geophysical Research*, vol. 82, p. 4559-4574
- Inada, Ai, 2002, Simulation of Martian Surface Fog and Calibration of Mars Imaging Camera for its Future Observations, thesis manuscript
- James, P.B., Briggs, G., Barnes, J. and Spruck, A., 1979 Seasonal recession of Mars' south polar cap as seen by Viking, *Journal of Geophysical Research*, vol. 84, p. 2889-2922
- James, P.B., 1979, Recession of Martian north polar cap: 1977-1978 Viking observations, *Journal of Geophysical Research*, vol. 84, p. 8332-8334
- James, P.B., 1982, Recession of Martian north polar cap: 1979-1980 Viking observations, *Icarus*, Vol.52, p. 565-569
- James, Philip B., Bruce A. Cantor, Scott Davis, 2001, Mars Orbiter Camera observations of the Martian south polar cap in 1999-2000, *Journal of Geophysical Research*, Vol.106, p. 23,635 - 23,652
- Johnson J.R., Grundy, W. M., Lemmon, M., Herkenhoff, K., 2001, Visible/Near-Infrared Spectroscopy of Dust Deposition on Mars, American Geophysical Union, Fall Meeting 2001, abstract P52B-0579
- Johnson, Jeffrey R., Grundy, William M., Lemmon, Mark T., 2003, Dust deposition at the Mars Pathfinder landing site: observations and modeling of visible/near-infrared spectra, *Icarus* 163, p. 330-346
- Kahn, R., 1984, The spatial and seasonal distribution of Martian clouds and some meteorological implications, *Journal of Geophysical Research*, Vol. 89, p. 6671-6688
- Kieffer, H.H., 1968, Near infrared spectral reflectance of simulated Martian frosts. PhD thesis, Calif.Inst.Tech
- Kieffer, H.H., 1970, Spectral reflectance of CO - HO frosts, *Journal of Geophysical Research*, Vol. 75, p. 501
- Kieffer, H.H., 1990, H<sub>2</sub>O grain size and the amount of dust in Mars' residual north polar CAP, *Journal of Geophysical Research*, Vol. 95, p. 1481-1493
- Kieffer, H.H., Jakosky, B.M., Snyder, C.W., Matthews, M.S. with 114 collaborating authors, 1992, *Mars*, The University of Arizona Press, Tucson, 1498 p.
- Kieffer, Hugh H., Titus, Timothy N. Mullins, Kevin F. Christensen, Philip R., M., 2000, Mars south polar spring and summer behavior observed by TES: Seasonal cap evolution controlled by frost grain size, *Journal of Geophysical Research*, Volume 105, p. 9653-9700
- Kieffer, Hugh H., 2003, Behavior of solid CO<sub>2</sub> on Mars: a real zoo, *Journal of Geophysical Research*, 6<sup>th</sup> International conference on Mars

- Kossacki, Konrad J., Markiewicz, W.J., 2002, Martian seasonal CO<sub>2</sub> ice in polygonal troughs in Southern Polar region: role of the distribution of subsurface H<sub>2</sub>O ice, *Icarus*, Vol.160, p. 73-85
- Kossacki, Konrad J., Markiewicz, W.J. and Smith, Michael D., 2003, Surface temperature of Martian regolith with polygonal features: influence of the subsurface water ice, *Planetary and Space Science*, Volume 51, Issue 9-10, p. 569-580
- Kossacki, Konrad J., Markiewicz, W.J. 2004, Seasonal melting of surface water ice condensing in martian gullies, *Icarus*, Volume 171, Issue 2, p. 272-283
- Kurucz, R.L., Furelid, I., and Brault, J. (1984) Solar flux atlas from 296 to 1300 NM. National Solar Observatory Atlas, Sunspot, New Mexico: National Solar Observatory.
- Landis, G.A., and Jenkins,P.P., 2000, Measurement of the settling rate of atmospheric dust on Mars by the MAE instrument on Mars Pathfinder, *Journal of Geophysical Research*, Vol. 105, p. 1855-1858
- Langvin, Y. , Poulet, F., Bibring, J.-P., Schmitt, B., Doute, S., Gondet, B., 2005, Summer evolution of the North Polar Cap of Mars as observed by OMEGA/Mars Express, *Science*, Vol. 307, p. 1581-1584
- Leighton, R. R., Murray, B. C., 1966, Behavior of carbon dioxide and other volatiles on Mars, *Science*, vol. 153, p. 136-144
- Litvak, M.L., Mitrofanov, I. G., Kozyrev, A. S., Sanin, A. B., Tret'yakov, V. I., Boynton, W. V., Shinohara, C., Hamara, D., Saunders, S., Drake, D.M., 2004, Seasonal Carbon Dioxide Depositions on the Martian Surface as Revealed from Neutron Measurements by the HEND Instrument Onboard the 2001 Mars Odyssey Spacecraft, *Solar System Research*, v. 38, Issue 3, p. 167-177
- Lyra, Von G., 1940, Über den Einfluß von Bodenerhebungen auf die Strömung einer stabil geschichteten Atmosphäre, *Beiträge zur Physik der freien Atmosphäre*, Bd. 26, s.197-206
- Malin, M.C., Danielson,G.E., Ingersoll, A.P., Masursky, H., Veverka, J., Ravine, M.A., Soulanalle, T.A., 1992, Mars Observer Camera, *Journal of Geophysical Research*, Vol. 97, p. 7699-7718
- Malin, Michael C., Caplinger, Michael A., Davis, Scott D., 2001, Observational Evidence for an Active Surface Reservoir of Solid Carbon Dioxide on Mars, *Science*, Volume 294, Issue 5549, p. 2146-2148
- Markiewicz, W.J., Sabolotny, R.M., Keller, H.U., Thomas, N., Titiv, D., and Smith, P.H. 1999, Optical properties of the martian aerosols derived from Imager for Mars Pathfinder midday sky brightness data, *Journal of Geophysical Research*, Vol. 104, p. 9009-9018
- Maattanen, A., H. Vehkamäki, A. Lauri, S. Merikallio, J. Kauhanen, H. Savijärvi, and M. Kulmala (2005), Nucleation studies in the Martian atmosphere, *J. Geophys. Res.*, 110, E02002, doi:10.1029/2004JE002308.

- Mischna, Michael A., Bell, James F., James, Philip B., Crisp, David, 1998, Synoptic measurements of Martian winds using the Hubble Space Telescope, *Geophysical Research Letters*, Volume 25, Issue 5, p. 611-614
- Moroz, V.I., Petrova, E.V., and Ksanfomality, L.V., 1993, Spectrophotometry of mars in the KRFM experiment of the Phobos mission: Some properties of the particles of atmospheric aerosols and the surface. *Planetary and space science* 41, p.569-585
- Murphy, James R., Leovy, Conway B, and Tillman, James E, 1990, Observations of Martian Surface Winds at the Viking Landing 1 Site, *Journal of Geophysical Research*, Vol.95, p. 14,555-14,576
- Paige, D.A., Herkenhoff, K.E., and Murray, B.C., 1990, Mariner 9 observations of the south polar cap of Mars: evidence for residual CO<sub>2</sub> frost, *Journal of Geophysical Research*, Vol. 95, p.1319-1335
- Piqueux, Sylvain, Byrne, S., Richardson, M.I., 2003, Sublimation of Mars's southern seasonal CO<sub>2</sub> cap and the formation of spiders, *Journal of Geophysical Research*, volume 108, p. 5084
- Pollack, J. B., Colburn, D. S., Flasar, F. M., Kahn, R., Carlston, C. E., Pidek, D. G., Properties and effects of dust particles suspended in the Martian atmosphere, *Journal of Geophysical Research*, Vol. 84, p. 2929-2945
- Schorghofer, N, Aharonson, O., Gerstell, M. F., 2003, Slope-Streak Formation and Dust Deposition Rates on Mars, 34th Annual Lunar and Planetary Science Conference, March 17-21, League City, Texas, abstract no. 2012
- Seiff, A. and Kirk, D.B., 1977, Structure of the atmosphere of Mars in Summer at mid-latitudes, *Journal of Geophysical Research*, Vol. 82, p.4364-4378.
- Seiff, A., Schofield, J. T., Murphy, J. R., Mihalov, J. D., 1999, Winds on Mars at the Pathfinder Landing Site, American Astronomical Society, DPS meeting 31, abstract no.68.02
- Smith, Michael D., 2004, Interannual variability in TES atmospheric observations of Mars during 1999-2003, *Icarus*, Vol.167, p.148-165
- Shkuratov, Yu., Kreslavsky, M., Kaydash, V., Viden, G., Bell III, J., Wolff, M., Hubbard, M., Noll, K., Lubenow, A., 2005, Hubble Space Telescope imaging polarimetry of Mars during the 2003 opposition, *Icarus*, V. 176, p.1-11
- Smith, David E., Zuber, Maria T., Frey, Herbert V., Garvin, James B., Head, James W., Muhleman, Duane O., Pettengill, Gordon H., Phillips, Roger J., Solomon, Sean C., Zwally, H. Jay, Banerdt, W. Bruce, Duxbury, Thomas C., Golombek, Matthew P., Lemoine, Frank G., Neumann, Gregory A., Rowlands, David D., Aharonson, Oded, Ford, Peter G., Ivanov, Anton B., Johnson, Catherine L., McGovern, Patrick J., Abshire, James B., Afzal, Robert S., Sun, Xiaoli, 2001, Mars Orbiter Laser Altimeter: Experiment summary after the first year of global mapping of Mars, *Journal of Geophysical Research*, Volume 106, Issue E10, p. 23689-23722

- Smith, D.E., Zuber, M.T., Neumann, G.A., 2001, Seasonal variation of snow depth on Mars, *Science*, Vol. 294, p. 2141-2146
- Snyder, C.W. 1977, The mission of the Viking Orbiters, *Journal of Geophysical Research*, Vol. 82, p. 3971-3983
- Thomas, P. C., Malin, M. C., Edgett, K. S., Carr, M. H., Hartmann, W. K., Ingersoll, A. P., James, P. B., Soderblom, L. A., Veverka, J., Sullivan, R., North-south geological differences between the residual polar caps on Mars, *Nature*, Vol. 404, p. 161-164
- Titus, T.T., Kieffer, H.H., Mullins, K.F., Christensen, P.R., 2001, TES premapping data: Slab ice and snow flurries in the Martian north polar night, *Journal of Geophysical Research*, Vol. 106, p.23181-23196
- Tomasko, M.G., Doose, L.R., Lemmon, M., Smith, P.H., and Wegryn, E., 1999, Properties of dust in the Martian atmosphere from the Imager on Mars Pathfinder, *Journal of Geophysical Research*, Vol. 104, p. 8987-9008
- Toon, O.B., Pollack, J.B., and Sagan, C., 1977, Physical properties of the particles composing the Martian dust storm of 1971-1972, *Icarus* 30, p. 663 - 669
- Wang, Huiqun and Ingersoll, Andrew P., 2002, Martian clouds observed by Mars Global Surveyor Mars Orbiter Camera, *Journal of Geophysical Research*, Vol. 107, 5079
- Wolff, M.J., Bell III, J.F., James, P.B., Clancy, R.T., Lee, S.W., 1999, Hubble Space Telescope observations of the martian afelion cloud belt prior to the Mars Pathfinder mission: seasonal and interannual variations, *Journal of Geophysical Research*, Vol. 104(E4), p. 9027-9041
- Wood, S. E., Catling, D. C., Rafkin, S. C. R., Ginder, E. A., Peacock, C. G., 2003, MGS Observations and Modeling of Martian Lee Wave Clouds, Sixth International Conference on Mars, July 20-25 2003, Pasadena, California, abstract no. 3283
- Zuber, M.T., Smith, D.E., Solomon, S.C., Muhleman, D.O., Head, J.W., Garvin, J.B., Abshire, J.B., Bufton, J.L., 1992, The Mars Observer Laser Altimeter Investigation, *Journal of Geophysical Research*, Vol. 97, p. 7781-7797

# Acknowledgements

I thank my supervisors in the Max-Planck-Institut für Sonnensystemforschung Dr. habil. Horst Uwe Keller and Dr. habil. Ulrich Christansen for offering me the possibility to work on this thesis and study at the MPS.

I would like to thank my supervisor Wojciech Markiewicz for the great opportunity to get into Martian science and to gain experience of doing it myself. Wojciech, thank you for showing me an unlimited world of possibilities and guiding me there with all your tact.

With pleasure I also thank Ai Inada. Ai, I appreciate all the time you spent working with me, all the explanations you gave me, all your long stays in the office for routine work with me. And specially, thank you for doing it with a smile! You taught me most of the things I used for my work. I am deeply grateful to you for being my guide, my advisor, and most important, my friend.

Many thanks to Nick Hoekzema for all the patience he had for reading and correcting this work, for all advises and great comments.

I thank Dr. habil. Konrad Kossacki for the interesting and instructive collaboration that led to the appearance of chapter 4.

I thank Anton Ivanov for providing me with MOLA data that were used in this work and for all the explanations and help in working with these data.

I also would like to thank the HRSC Co-Investigator team for the great opportunity to be at the frontier of Martian investigations, to see how science really works and to learn a lot being inside this team. Personal thanks to John Murrey, Bernard Foing, and Boris Ivanov.

A lot of thanks to the secretary of our group, Sabine Stelzer. Sabine, your help without a single refuse made my stay at the MPS (and generally in Germany) very easy and comfortable. Thank you!

I want to thank all my friends, all students and colleagues in MPS for all kinds of help during these 3 years. Thank you all!

With great gratitude I thank my parents, Vera Mychak and Valeriy Portyankin, for their believe in me even in times when I lose it myself. I know they are all the time by my side and that helped me to finish this work and to keep the strength to go further.

Мама, папа, вы у меня самые лучшие! Спасибо вам огромное за веру в меня и за вашу поддержку!



# Lebenslauf

Name: Ganna Portyankina

Geburtsdatum: 29. November 1977

Geburtsort: Karachevka, Ukraine

Eltern: Valeriy Portyankin  
Vera Mychak

Staatsbürgerschaft: Ukrainisch

Schulbildung: 9/1985–6/1993 Grundschule N2, Karachevka  
9/1993–6/1995 Grundschule N1, Pokotilovka

Studium: 9/1995–7/2000 Physikstudium an der physikalischen  
Fakultät der Nationalen Universität Kharkiv, Ukraine  
Abteilung für Physik und Astronomie

9/1998–1/1999 Bachelorarbeit: "Classical means of description  
of minor planets' gravitational fields  
and their application to the asteroids"

9/1999–7/2000 Diplomarbeit: "Approximation of asteroid  
gravitational fields by the field of  
a gravitational doublet"

8/2000–1/2002 Wissenschaftlicher Mitarbeiter des Instituts  
für Astronomie der Nationalen Universität Kharkiv

2/2002–2/2005 Doktorarbeit an dem Max-Planck-Institut für  
Sonnensystemforschung, Katlenburg-Lindau,  
und der Universitäts-Sternwarte, Göttingen